Universitetet i Stavanger

FACTULTY OF SCIENCE AND TECHNOLOGY

MASTER'S THESIS

Study programme / specialisation: Marine and Offshore Technology	Spring, 2024 Open / ~~Confidential~~
Author: Andrè Gjerde	
Supervisor at UiS: Prof. Muk Chen Ong Co-supervisor: Xueliang Wen External supervisor(s):	
Thesis title: Dynamic analysis of gravity-type fish cages using XPBD algorithm	
Credits (ECTS): 30	
Keywords: Aquaculture; gravity-type fish cage; lifting operations; extended position-based dynamics; extreme conditions; regular and irregular wave.	Pages: 145 + appendix: 0 Stavanger, 15/06/ 2024

I, **Andrè Gjerde**, declare that this thesis titled, “Dynamic analysis of gravity-type fish cages using XPBD algorithm” and the work presented in it are my own. I confirm that:

- This work was done wholly or mainly while in candidature for a master’s degree at the University of Stavanger.
- Where I have consulted the published work of others, this is always clearly attributed.
- Where I have quoted from the work of others, the source is always given. With the exception of such quotations, this thesis is entirely my own work.
- I have acknowledged all main sources of help.

Acknowledgements

I extend my sincere gratitude to my supervisor, Muk Chen Ong, and my co-supervisor, Xueliang Wen, for their unwavering support, invaluable guidance, and their profound feedback throughout my thesis journey. Their expertise and encouragement have been crucial in shaping this research and guiding me through its various stages. I am deeply grateful for their mentorship and dedication.

I extend my gratitude to the University of Stavanger for providing me with the opportunity to pursue my academic aspirations and undertake this thesis. The university's resources and academic environment have greatly facilitated my research and academic growth.

Abstract

The dynamic behaviors of fish cages are numerically studied to explore the safety issue of the aquaculture system. The hydrodynamic forces acting on the net panels are simplified into Morison forces acting on the net ropes. The structural responses of the fish cages and the mooring system are calculated using an extended position-based dynamics (XPBD) algorithm, where correction forces are added to improve the accuracy of the original XPBD. Two typical cases are involved in the present study: lifting operations of a fish cage during the de-lice or harvest operations and ultimate state analysis of multiple fish cages with a mooring system. In the case of lifting operations, the environmental loads are neglected due to the operational condition. The structural model of modified XPBD is validated against experimental results obtained from a flexible horizontal net. A time-step sensitivity study is conducted for the lifting operation of the fish cage. The results of the lifting operations reveal a rapid increase in lifting force due to the weight of the sinkers positioned at the bottom of the side net. Furthermore, it is observed that the maximum tension in the net occurs at the net ropes connected to the center point of the bottom net. The damaged fish cages with broken net ropes at the bottom net exhibit no significant changes in lifting force and net tension. However, structural reinforcements are recommended for the bottom net to ensure safe lifting operations. In the case of the ultimate state analysis of multiple fish cages with a mooring system, the environmental loads due to waves and currents are included to conduct the ultimate state analysis. The present modified XPBD is coupled with the Morison model, and the method is validated against the experimental results of a vertical net panel and a cage net. Grid and time-step sensitivity studies are conducted for the single fish cage with a mooring system. Results show that the maximum pitch angle of the floating collar and sinker tube,

the horizontal displacement, and the vertical displacement are reached when the flow angle is 0 degrees. However, the maximum horizontal force is observed when the flow angle is 30 degrees and the maximum roll angle is observed when the flow angle is 45 degrees. The effect of regular and irregular waves on a single fish cage with a mooring system shows minimal changes in the maximum calculated values. However, when subjected to regular waves, the fish cage exhibits an increased pitch angle. Summarised from the two cases, the safety of the fish cage system can be enhanced by numerically exploring the operational activities and the ultimate state.

Contents

List of Figures

List of Tables

Chapter 1

Introduction

1.1 Background and Motivation

The anticipated increase in the human population, expected to grow from 8 billion to 9.7 billion by 2050, places exceptional demands on food and seafood production [9]. This escalating demand poses substantial challenges to food and seafood industries, necessitating improvements in production efficiency and sustainability [12, 13]. To address this challenge, exploration into innovative technologies and practices in aquaculture is imperative.

Studies suggest that seafood production exhibits superior sustainability levels compared to meat production [10]. However, a significant challenge lies in producing food to meet this demand without causing adverse impacts on the environment. To address this challenge, efforts within the seafood production industry have experienced rapid growth on a global scale. Aquaculture production and total fisheries reached 49.2% in 2020, compared to 13.4% in 1990. This growth has been prioritized over conventional land-based agriculture, as suggested by reports from SjømatNorge and the Food and Agriculture Organization of the United Nations (FAO) [21, 10]. As reported by FAO in 2022, fisheries and aquaculture production achieved a new record of 214 million tonnes in 2020, with aquaculture contributing 122.6 million tonnes to this total. Of this total, approximately 54.4 million tonnes were cultivated in inland waters, while 68.1 million tonnes originated from marine and coastal aquaculture (see Figure 1.1) [10]. During the

same period, aquatic animal production exceeded the 1990s average by over 60%, surpassing global population growth. Furthermore, fish contributed to approximately 17% of global protein consumption in 2020.

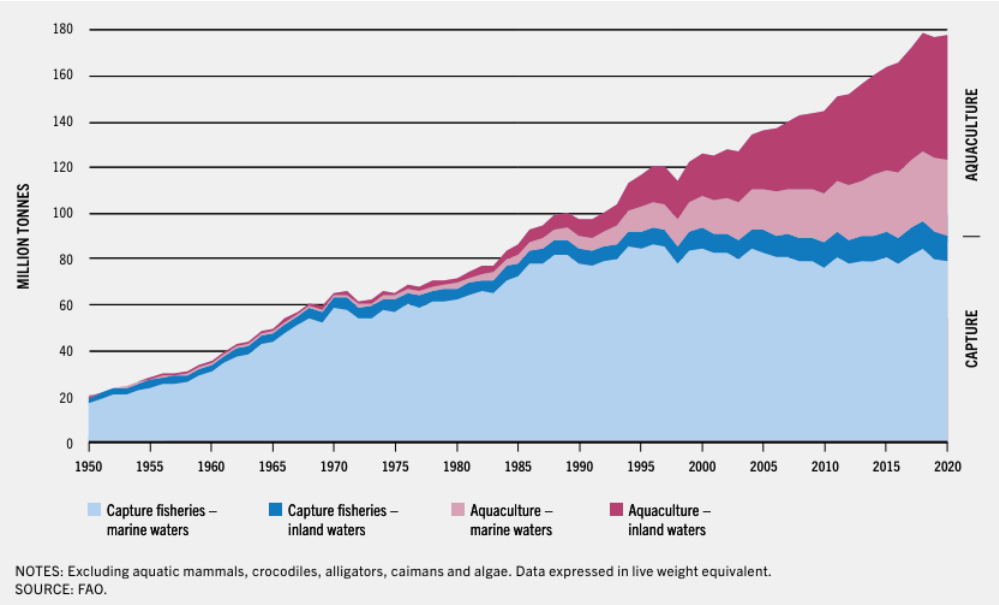

Figure 1.1: World capture fisheries and aquaculture production (FAO 2022) [10].

The development of the Norwegian aquaculture industry began in the 1970s with the first capture of Atlantic salmon in floating sea cages. Since then, aquaculture has evolved significantly and grown into a substantial sector in coastal regions. In Norway, Atlantic salmon comprises the majority of total ocean-farmed fish, amounting to 1.2 million tonnes, while other species such as cod, halibut, and char are also cultivated.

Although Norway has the perfect conditions for farming salmon and other species of fish in its cold, clear waters and along with strict criteria for the farms, it still encounters numerous challenges. Among these challenges are sea lice infestations and environmental impacts on the ecosystem. Sea lice are parasitic crustaceans that harm fish by feeding on their blood, leading to reduced growth, increased mortality, and weakened immune systems. These parasites can also threaten wild salmon populations and disrupt marine ecosystems. Effective man-

agement and prevention are crucial to mitigate the impact of sea lice infestations and protect both farmed and wild fish.

1.2 Overview of Aquaculture Cage Practice

Numerous fish farming methods exist, each presenting distinct advantages and challenges. Commonly employed techniques include fish cages [20][22], pond aquaculture [20][14], recirculating aquaculture system (RAS) [20], integrated multi-trophic aquaculture (IMTA) [2], and land-based aquaculture [4]. Among these, the fish cages stand out as versatile and widely utilized farming systems. Typically deployed in marine or freshwater environments, they consist of floating enclosures where fish are raised in controlled conditions. These cages provide efficient space utilization, enabling high population densities while minimizing environmental impacts. Two critical components of a fish farm are the cage system and the feeding system. Ongoing research in this field focuses on improving fish cage design and management practices to optimize production efficiency and environmental sustainability.

1.2.1 Traditional Fish Cage Systems

The traditional fish cage systems have been in practice for several decades and have proven to be versatile and widely used in different countries such as Norway, China, Scotland, and Ireland [5]. These cage systems can be classified into three different variants: floating cages, submersible cages, and submerged cages, as shown in Figure 1.2 [1].

Floating cages: These are buoyant structures that remain on the water surface. They are typically anchored in place and float with the water's surface movements. Floating cages are commonly used in open water environments and are visible above the water surface [19].

Submersible cages: Also known as semi-submersible cages, these structures partially submerge beneath the water surface while still maintaining some buoyancy. They are designed to withstand wave action and may be adjusted to various

depths. Submersible cages offer increased stability compared to floating cages and are often used in areas with rough sea conditions [19].

Submerged cages: These cages are fully submerged below the water surface and are usually anchored to the seabed. Submerged cages provide protection from surface waves and weather conditions. They are often used in deeper waters and can be less visible compared to floating and submersible cages [19].

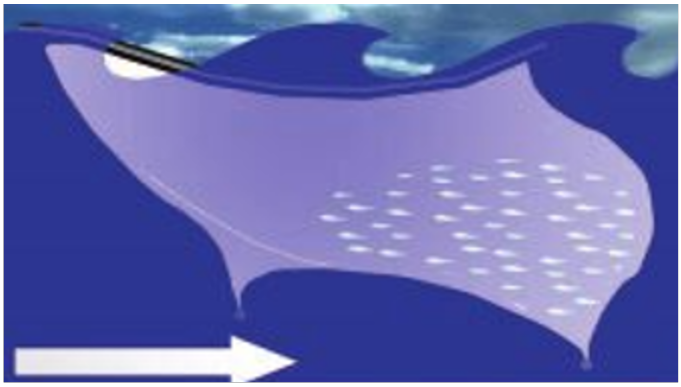

(a) Floating cage

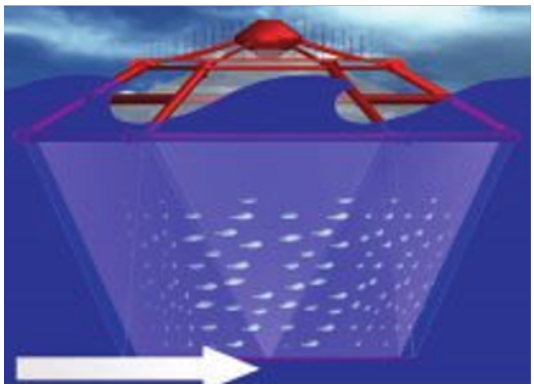

(b) Submersible cage

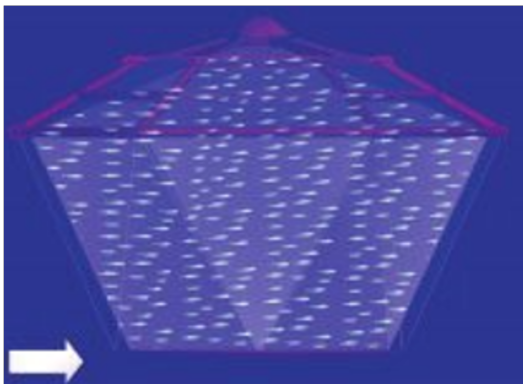

(c) Submerged cage

Figure 1.2: Illustration of different cage systems used for ocean-farmed fish, by Bugrov(2006) [6].

1.2.2 Gravity-type fish cage

A gravity-type fish cage is a structure used in Norwegian aquaculture for farming fish in open water bodies such as oceans, seas, or fjords. The design of a gravity-

type fish cage typically involves a framework made of buoyant materials such as plastic or metal, which supports a mesh netting enclosure submerged in the water. The cage is usually cylindrical or square in shape, with netting or mesh walls that allow water to flow freely through the structure while containing the fish inside. Additionally, a mooring system is often attached to the fish cage to keep it anchored in place against currents and waves. A schematic of a cylindrical shaped gravity-type fish cage is shown in Figure 1.3 [24].

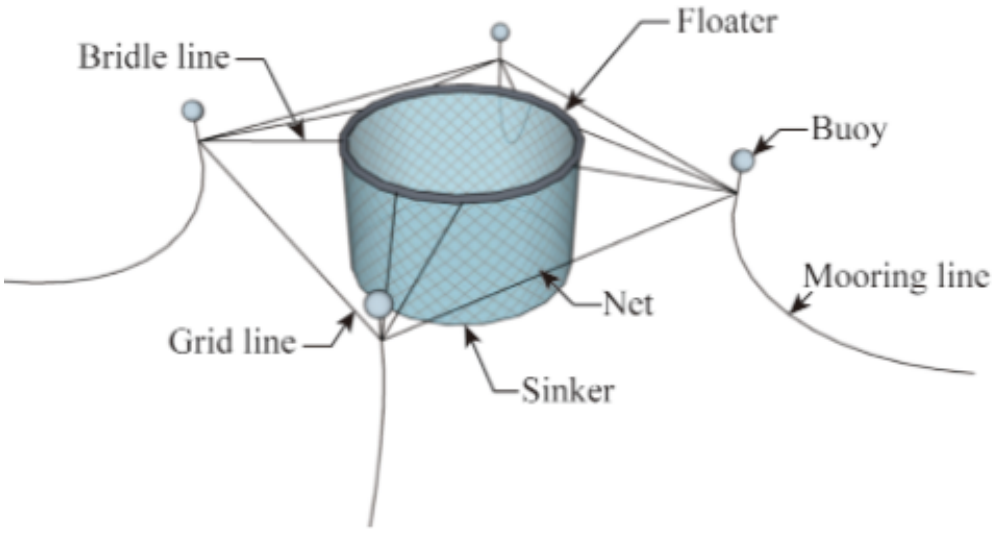

Figure 1.3: Schematic diagram of a cylindrical shaped gravity-type fish cage used for ocean-farmed fish, by Xiao-dong et al.(2021).

The following list outlines key components found in a typical fish cage mooring system:

- *Bridle line*: A bridle line is a rope or cable used to distribute loads evenly across multiple attachment points. In aquaculture, it's often used to connect a fish cage to its mooring system.

- *Grid line*: A grid line is a line or cable forming part of the structural support system within a fish cage. It helps to maintain the shape and integrity of the cage.

- *Floater collar*: A floater collar is a buoyant component typically located at the top of a fish cage. It provides buoyancy and stability to the cage structure, keeping it afloat on the water surface.
- *Sinker tube*: A sinker tube is a weighted component usually positioned at the bottom of a fish cage. It helps to stabilize the cage and maintain its position underwater.
- *Buoy*: In aquaculture, buoys are often used as part of mooring systems to provide flotation and anchor points.
- *Mooring line*: A mooring line is a rope or cable used to secure a floating structure, such as a fish cage, to an anchor or mooring point. It helps to keep the structure in place and resist movement caused by currents or waves.

The key feature of a gravity-type fish cage is its ability to sink to a desired depth in the water column through the use of weights or ballasts attached to the bottom of the cage. This sinking action is achieved by the force of gravity, hence the name.

Once the cage reaches the desired depth, it remains suspended in the water column, allowing fish to be contained within the netted enclosure while still having access to natural water currents and nutrients. This setup mimics the natural environment of fish while providing a controlled space for farming.

Furthermore, the gravity-type fish cages are often used in offshore aquaculture operations where there is sufficient water depth and current flow to support fish farming activities. They are designed to withstand the forces of waves, currents, and weather conditions while providing a stable environment for fish growth and production. These cages can vary in size and capacity depending on the specific requirements of the aquaculture operation and the species being farmed.

1.2.3 Alternative Concepts in Fish Cage Design

In recent years, there has been a significant shift in the fish farming industry from near shore to offshore locations, driven by the quest for innovative solutions capable of thriving in offshore environments. This shift has focused on innovative

fish cage designs specifically engineered to withstand the challenges of offshore applications while also featuring larger capacity, improved water exchange, extended lifespan, and reduced labor requirements.

One example of this innovation is Ocean Farm 1 [3], developed by SalMar ASA, which is an offshore fish farm located off the coast of Norway. The farm consists of a circular cage system surrounded by a robust barrier designed to withstand open sea conditions. It utilizes mooring lines for stability and is anchored to the seabed to ensure security. Using advanced technology, it remotely monitors water quality, feed distribution, and fish health. Ocean Farm 1 utilizes natural ocean currents for water exchange, reducing the risk of disease and pollution, and aims to produce 150,000 tonnes of salmon per year by 2030.

Figure 1.4: Ocean Farm 1 (source: SalMar [18]).

HavFarm 1 [15], developed by Nordlaks, is an innovative offshore aquaculture project located 5 kilometers southwest of Hadseløya off the coast of Norway. The fish farm is a vessel-shaped structure that measures 385 meters in length, and 59.5 meters in width, and has a salmon capacity of 10,000 tons. The ocean farm features a single-point mooring system that allows the structure to move within a circle with a radius of 450 meters from the center point of the site.

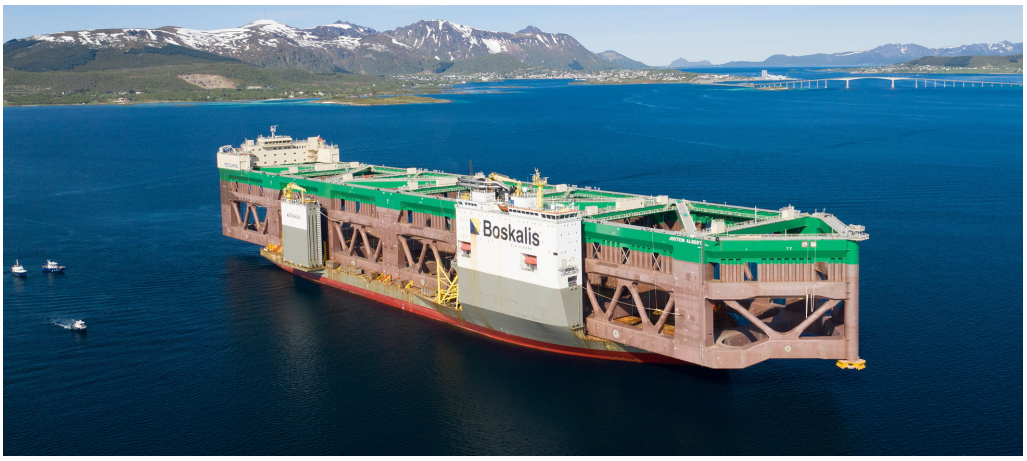

Figure 1.5: HavFarm 1 (source: Nordlaks [15]).

Deep Blue 1 [16] is an offshore aquaculture concept developed by RefaMed [17], introducing an innovative fish cage design specifically tailored for deep waters. The key feature of the fish cage is the tension-leg structure, which replaces traditional mooring lines with an anchoring system to the ocean floor, ensuring stability in rough offshore conditions.

Figure 1.6: Deep Blue 1 (source: CSSC-global, published on X [8]).

1.2.4 Environmental and Economic Benefits

Cage methods harness the environment to create a more sustainable and efficient aquaculture system, prioritizing ecological balance and economic viability [11]. This farming method operates efficiently by harnessing natural forces and minimizes adverse effects on the surrounding ecosystem, presenting an environmentally sustainable alternative [23]. In contrast, conventional methods often require significant energy inputs to be operational, such as energy for water circulation, filtration, aeration systems, and heating/cooling systems.

In addition to the environmental benefits of the fish cage, the adoption of this fish farming method holds promising economic advantages. The potential to reduce operational costs while simultaneously increasing the yield, contributing to its economical sustainability. Furthermore, optimization of the gravity-type fish cages also has the potential for positive global impact on sustainable aquaculture practices [5]. For instance, by incorporating advanced monitoring and control systems into these cages, such as sensors for water quality and automated feeding systems, operators can significantly reduce human interference and minimize environmental impact. Additionally, innovations in cage design, such as improved materials or streamlined shapes, can improve water circulation and oxygenation, promoting healthier fish populations and reducing the need for chemical treatments. Implementing these environmentally conscious and efficient methods worldwide can lead to reduced resource usage, minimized waste production, and overall improvement in the sustainability of aquaculture operations on a global scale.

1.2.5 Future Directions and Challenges

Fish cage farming has contributed towards meeting the growing demand for seafood while effectively addressing concerns associated with over-fishing and degradation of the ocean environment. However, further progress is still needed to achieve the required food production levels and to further reduce the environmental impact. As the fish farming industry moves toward a more sustainable approach, the use of fish cages emerges as a promising solution.

Another significant challenge regarding fish farming is the management of sea lice infestations. Sea lice, such as Lepeophtheirus salmonis and Caligus rogercresseyi [7], are parasitic crustaceans that can cause significant harm to farmed fish populations, leading to economic losses and environmental concerns. Further development of effective strategies for sea lice control while minimizing environmental impacts remains a critical area of research and innovation in fish cage aquaculture.

Further study will allow for exploration of the full potential of fish cage aquaculture, aiming to optimize its design, performance, and scalability, while addressing challenges such as sea lice infestations and environmental concerns.

1.3 Research objective

The main objective of this thesis is to investigate and analyze the dynamic behaviors, structural integrity, stability, load distributions, and performance of gravity-type fish cages under various operational activities and environmental conditions.

First, a numerical study on the lifting operation of a gravity-type fish cage will be conducted. The structural model of modified XPBD is validated against experimental results obtained from a flexible horizontal net. A time-step sensitivity study is conducted for the lifting operation of the fish cage. The dynamic behaviors of both regular and damaged fish cages during lifting operations are numerically studied and compared.

Then, a dynamic analysis of multiple gravity-type fish cages with mooring systems in regular and irregular waves will be carried out. The environmental loads due to waves and currents are included to conduct the ultimate state analysis. The present modified XPBD is coupled with the Morison model, and the method is validated against the experimental results of a vertical net panel and a cage net. Grid and time-step sensitivity studies are conducted for the single fish cage with a mooring system. The dynamic responses of the multiple gravity-type fish cages with mooring systems under different pretensions of mooring systems, different angles of incoming waves and currents, and regular and irregular wave conditions are compared.

1.4 Thesis outline

- **Chapter 1:** This chapter introduces the research background, motivation, and objectives.
- **Chapter 2:** The theory behind the fish cage structures and the hydrodynamic behaviors are detailed.
- **Chapter 3:** Numerical study on the lifting operations of a gravity-type fish cage. The XPBD method is introduced to investigate and demonstrate the lifting operations of both regular and damaged fish cages.
- **Chapter 4:** A numerical study on the dynamic response of gravity-type fish cages in extreme conditions under regular and irregular wave and current conditions is performed.
- **Chapter 5:** A summary of the thesis is given.

References

[1] A.K. Das et al. “Cage culture in reservoirs in India (a handbook)”. In: (2009). URL: https://digitalarchive.worldfishcenter.org/handle/20.500.12348/1423.

[2] Marta Correia et al. “Integrated Multi-Trophic Aquaculture: A Laboratory and Hands-on Experimental Activity to Promote Environmental Sustainability Awareness and Value of Aquaculture Products”. In: Front. Mar. Sci.7:156 (2020). DOI: https://doi.org/10.3389/fmars.2020.00156.

[3] SalMar ASA. *Våre viksomhetsområder*. Online; accessed April 17th 2024. URL: https://www.salmar.no/om-salmar/vare-virksomhetsomrader/.

[4] Christina Benjaminsen. “Fish farms moving onshore”. In: (2021). https://www.sintef.no/en/latest-news/2021/fish-farms-moving-onshore/.

[5] Malcolm Beveridge and Jon Arne Grøttum. “A review of cage culture: northern Europe.” In: (Jan. 2007), pp. 129–158. URL: https://www.researchgate.net/publication/257655031_A_review_of_cage_culture_northern_Europe.

[6] Leonid Bugrov. “Underwater Fish-Farming System “Sadco””. In: 1 (Jan. 2006), pp. 34–45. URL: https://www.researchgate.net/publication/324138442_Underwater_Fish-Farming_System_Sadco.

[7] J Burka and Crawford Revie. “22 Lepeophtheirus salmonis and Caligus rogercresseyi”. In: *Fish Parasites: Pathobiology and Protection* (Jan. 2012), p. 350. DOI: 10.1079/9781845938062.0350.

[8] CSSC-global. Online; accessed April 17th 2024. URL: https://twitter.com/CSSC_global/status/1505741306680979456.

[9] Maarten Elferink and Florian Schierhorn. “Global Demand for Food Is Rising. Can We Meet It?” In: (2016). https://hbr.org/2016/04/global-demand-for-food-is-rising-can-we-meet-it.

[10] FAO. “The State of World Fisheries and Aquaculture (SOFIA)”. In: (2022). https://www.fao.org/documents/card/en?details=cc0461en. ISSN: 978-92-5-130562-1.

[11] NOAA Fisheries. “Aquaculture Supports a Sustainable Earth”. In: (2020). https://www.fisheries.noaa.gov/feature-story/aquaculture-supports-sustainable-earth.

[12] Jason Holland. “DNV: Global seafood demand predicted to soar through 2050 in line with population growth”. In: (2024). https://www.seafoodsource.com/news/premium/supply-trade/dnv-global-seafood-demand-predicted-to-soar-through-2050-in-line-with-population-growth.

[13] Djene G. Kidane and Eivind H. Brækkan. “Global seafood demand growth differences across regions, income levels, and time”. In: (2021). https://munin.uit.no/bitstream/handle/10037/24554/article.pdf?sequence=4&isAllowed=n.

[14] Aquatic Network. “Pond Culture”. In: (2014). https://www.aquanet.com/pond-culture.

[15] Nordlaks. *Havfarmen ”Jostein Albert”*. Online; accessed April 17th 2024. URL: https://www.nordlaks.no/havfarmen-jostein-albert/.

[16] Nordlaks. *Havfarmen ”Jostein Albert”*. Online; accessed April 17th 2024. URL: https://www.nordlaks.no/havfarmen-jostein-albert/.

[17] REFAMED. *TLC System*. Online; accessed April 17th 2024. URL: https://refamed.com/gabbie_mare/tlc_system.html.

[18] SalMar. *Bærekraft i alt vi gjør*. Online; accessed April 17th 2024. URL: https://www.salmar.no/baerekraft/baerekraft-i-alt-vi-gjor/.

[19] D.C.B Scott and J.f Muir. “Offshore cage systems: A practical overview”. In: *Mediterranean offshore mariculture* (2000), pp. 79–89.

[20] SeaChoice. “AQUACULTURE METHODS”. In: (2022). https://www.seachoice.org/info-centre/aquaculture/aquaculture-methods/.

[21] SjømatNorge. “Nurturing growth: the Norwegian way”. In: (2021). https://sjomatnorge.no/materiell/nurturing-growth-the-norwegian-way/.

[22] STARAQ. “What Is Fish Cage”. In: (2023). https://staraq.com/what-is-fish-cage/.

[23] University of Stavanger. “100 million for a more climate-friendly aquaculture industry”. In: (2021). https://www.uis.no/en/sustainability/100-million-for-a-more-climate-friendly-aquaculture-industry.

[24] BAI Xiao-dong et al. “Prediction of Long-Term Extreme Response of Fish Cage Using Environmental Contour Method”. In: *China Ocean Eng.* 35 (2021), pp. 332–342. ISSN: 0890-5487. DOI: https://doi.org/10.1007/s13344-021-0031-2.

Chapter 2

Theory

2.1 Challenges in structural design

The main challenges met in the prediction of the structural response of a gravity-type fish cage can be divided into four parts, explained by Hui Cheng (2022) [6]:

1. How the flow field surrounding the structure should be modeled.
2. How to model environmental loads.
3. How to calculate the dynamic response of the net.
4. How the problem of the fluid-structure interaction of the net should be approached.

The first challenge is important when modeling nets under environmental loads. Different points on the fish cage can have different flow velocities caused by the wake effect. The environmental loads on the fish cage depend on the flow field surrounding the structure and can be modeled by two methods: Navier-Stokes equations and the potential flow theory[6].

The second challenge comes from the complexity of the fish cage structure. The computational cost has to be reduced and one way is to model the environmental loads. The hydrodynamic loads on the fish cage netting can be predicted using the Morison model [7] and the Screen model [17] [15], taking the flow field as the input. The Morison model focuses on individual twines in the fish net.

This hydrodynamic model is used to analyze the forces acting on these individual twines, taking drag force, inertia forces, and added mass due to water flow into account. The Screen model focuses on the larger components, the net panel. It addresses the behavior of multiple twines and is used to examine how the entire net structure interacts with the water flow. The Morison model and Screen model will be discussed further in section 2.3.1 and section 2.3.2, respectively.

The third challenge arises from the complexity of modeling the entire net structure twine by twine, as it is not a feasible method. The fish cage net structure consists of millions of twines, making it computationally expensive to model each element individually.

The fourth challenge stems from the properties of the net used, as it is flexible and has high porosity. Typically, these nets are flexible, allowing for significant displacements and deformations in response to the forces exerted by current and wave loads. These deformations have the potential to influence the surrounding flow dynamics.

2.2 Introduction to fish cage netting

Fish cage netting serves as a critical component in modern aquaculture, where its design directly impacts the efficacy of fish farming operations. The netting serves as a protective enclosure for the fish while allowing water to flow through. Commonly employed materials, such as polyethylene and nylon, are chosen for their durability and ability to withstand dynamic loads and aquatic environments. The structural design of the netting, frequently featuring square or diamond mesh patterns, significantly determines its strength and flexibility. Knot-less configurations further contribute to minimizing drag and the risk of entanglement.

Considerations regarding the design of fish cage netting include mesh size, material properties, and twine shape for better water flow circulation and to prevent the escape of juvenile fish. The material properties and the netting shape play a crucial role in contributing to surface roughness and hydrodynamic characteristics. Increased surface roughness leads to an increased drag force and increased turbulence regions [2], while low surface roughness decreases the drag force and

decreases the turbulence regions [26]. Figure 2.1 shows common net weaving methods used for offshore aquaculture farming. Table 2.1 [6] lists the properties of commonly used fish cage netting in industrial aquaculture farming.

Table 2.1: Physical properties of commonly used netting in fishing and aquaculture industries [6].

Materials	Scilicon-bronze
	Polyamide (PA)
	Polyester (PES)
	Polyethylene (PE)
	Polypropylene (PP)
	Polyethylene terephthalate (PET)
Mesh shape	Square
	Hexagonal
	Diamond
Twine shape	Monofilament
	Twisted
	Braided
Net weaving method	Knotless
	Knotted
	Welded
	Double-twisted

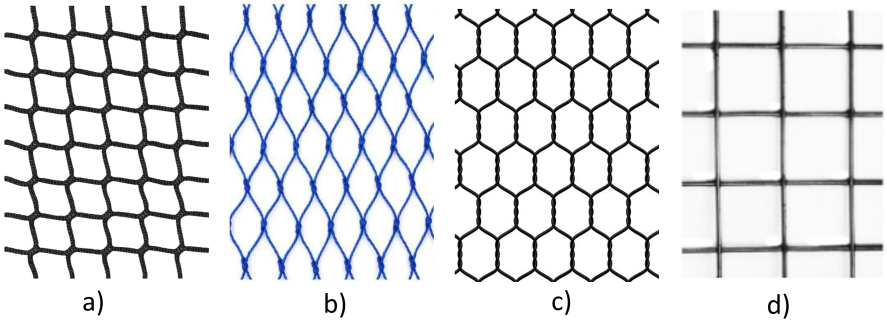

Figure 2.1: Different net weaving methods for nets: (a) Knotless net with square mesh [23], (b) Knotted net with square mesh [13], (c) Double twisted net with hexagonal mesh [28] and (d) Welded silicon-bronze net with square net [26].

Figure 2.2 displays the definitions of mesh size [11]. Half mesh is the distance from the center of one knot to the center of the adjacent knot in a net, while the whole mesh is the distance between the centers of two opposite knots. Mesh opening (aperture) is the inside distance between two opposite knots in a single pulled-out mesh of a net.

Several experimental studies have investigated the hydrodynamic characteristics of fish netting [26][16][2]. The findings have shown that the hydrodynamic characteristics also depend on the Reynolds number (Re) and the solidity (S_n). Typically, the Reynolds number for fish netting is within the range of 100 to 10,000, while the solidity typically ranges from 0.1 to 0.4 in the context of fish netting used in offshore industrial-sized fish cages [6]. These two dimensionless variables are expressed in Equations 2.1 and 2.2. The solidity equation, denoted as S_n, serves as an expression for knot-less netting; however, various weaving methods, as outlined in Table 2.1, may result in different expressions.

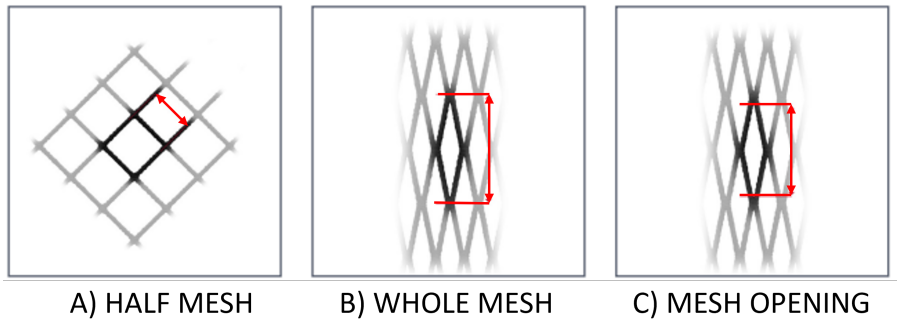

Figure 2.2: Definitions of mesh size [11]

Reynolds number is defined as:

$$Re = \frac{U * d_w}{\nu} \tag{2.1}$$

Solidity is defined as:

$$Sn = \frac{d_w(2L - d_w)}{L^2} \tag{2.2}$$

Where U is the fluid velocity, d_w is the twine diameter, ν is the kinematic viscosity of the fluid, and L is the half-mesh size.

2.3 Hydrodynamic modelling of fish cage

Hydrodynamic modeling techniques play an important role in various scientific and engineering disciplines, offering an effective method for modeling and analyzing complex events that may be impractical, too costly, or in some cases impossible to study through traditional experimental methods. These modeling techniques are tools used to gain insights, predict outcomes, and optimize designs.

2.3.1 Morison model

The Morison Equation holds a central role in the field of ocean engineering, providing a strong foundation for evaluating hydrodynamic forces exerted on sub-

merged or partially submerged structures in the context of wave and current loading. Morison et al. (1950) developed the Morison equation to calculate wave loads on slender vertical cylinders, such as rope or twine utilized in fish netting [18]. The equation identifies two forces: the fluid inertia force linked to water acceleration and the drag force tied to water velocity [19]. The Morison equation is expressed in simple and intricate terms in Equations 2.3 and 2.4, respectively.

$$F_{morison} = F_{inertia} + F_{drag} \tag{2.3}$$

$F_{inertia}$: considers the extra force due to the water around the structure moving with it.

F_{drag}: deals with the resistance the structure faces as water flows around it.

$$F_{morison} = \rho V \dot{u} + \rho C_a V(\dot{u} - \dot{v}) + \frac{1}{2} C_d A(\dot{u} - \dot{v}) \left|\dot{u} - \dot{v}\right| \tag{2.4}$$

Where ρ is the fluid density, V is the volume, $\dot{u} - \dot{v}$ is the velocity (can be denoted as $\vec{V}$). Furthermore, the volume $V = L\left(\frac{\pi}{4} \cdot d_w^2\right)$, area $A = L \cdot d_w$; and where d_w is the twine diameter and L is the length of the twine.

However, in situations where the structure's response to fluid motion involves low-frequency motions, particularly when the structure is relatively massive compared to the added mass of the surrounding fluid, the inertia term can be neglected. This is applicable when the natural frequency of the structure's response to waves or currents is much lower than the frequency of the fluid motion.

When examining a fish cage, particularly focusing on one segment of the net panel, they are constructed with numerous twines with small diameters, enabling the application of the Morison equation with the inertia term neglected. This simplification leaves the following equation:

$$F_{morison} = \frac{1}{2} C_d A(\dot{u} - \dot{v}) \left|\dot{u} - \dot{v}\right| \tag{2.5}$$

In practical applications for fish netting, the environmental load on a line-like structure can be decomposed into two components: normal drag and tangential drag [6].

$$F_n = \frac{1}{2} C_n \rho L d_w \left| u_n \right| u_n \tag{2.6}$$

$$F_t = \frac{1}{2} C_t \rho L d_w \left| u_\tau \right| u_\tau \tag{2.7}$$

Where ρ is the fluid density, C_n and C_t are the drag and tangential coefficients in the normal direction. u_n and u_τ represent the normal and tangential velocity of the fluid relative to the line element, respectively. d_w denotes the twine diameter, and L is the length of the line-element.

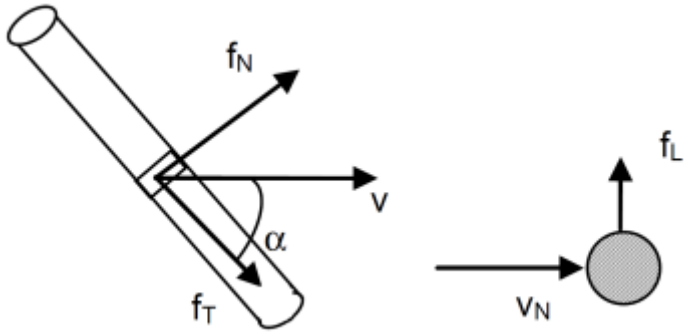

Figure 2.3: Definition of normal force f_N, tangential force f_T and lift force f_L on slender structural member exposed to a water particle velocity V [4]. Illustration from DNV [9].

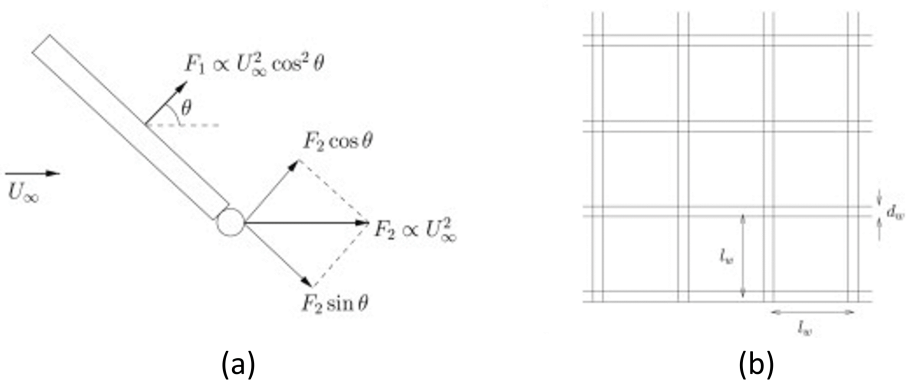

Figure 2.4: illustration of (a) Morison type force model applied to two twines in an ambient current of magnitude U_∞ and (b)net consisting of physical twines. d_w is twine diameter and l_w twine length. The solidity ratio for this square net is $S_n = 2d_w/l_2 - (d_w/l_w)^2$ [15].

Validation and verification studies have been conducted to assess the accuracy of the Morison model, applying various methodologies to increase its reliability. The impact of different environmental conditions, such as wave height, current speed, and water depth, on the model's applicability and accuracy is also a significant area of consideration. In practice, the precise determination of drag coefficients (C_n for normal drag and C_t for tangential drag) is important for accurately calculating the forces exerted on line-like structures, providing a comprehensive understanding of the hydrodynamic interactions. The selection and calibration of these coefficients significantly impact the model's predictive capabilities, rendering them essential parameters to ensure the effectiveness of the Morison model in real-world scenarios, as studied by numerous researchers [3][7][24][27][30].

Furthermore, industry standards and guidelines often recommend or prescribe the use of the Morison model in specific applications, indicating its acceptance and adoption within the field. Advancements in computational methods, including numerical simulations and computational fluid dynamics, have contributed to the ongoing refinement of the Morison model. Its interdisciplinary applications have extended its utility, fostering collaborations with fields such as structural

engineering, marine biology, and environmental science.

2.3.2 Screen model

Similar to the Morison model, the Screen model shares similar applications; however, instead of focusing on a line element, the Screen model examines the face element of a net panel. The hydrodynamic loads can be separated into two components with respect to the net panel or fluid flow [6]. In practical applications for fish netting, the environmental load on a net panel structure can be decomposed into two components: the fluid lift force (F_L) and the drag force (F_D), both associated with the direction of water velocity.

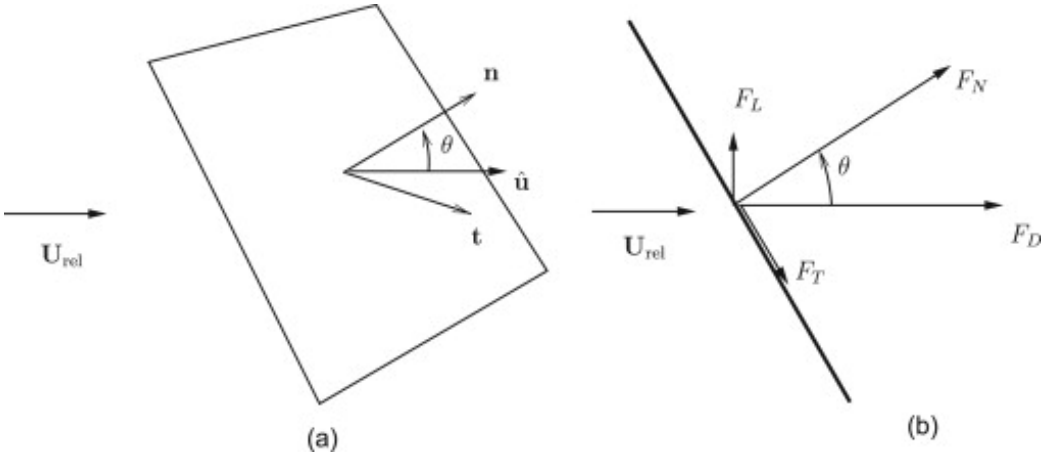

Figure 2.5: Left: unit vectors; the normal unit vector is perpendicular to the panel, the unit tangential vector lies in the plane of the panel, and the ambient current unit vector points in the direction of the local (relative) inflow. The angle is between the normal and inflow directions. Right: two-dimensional case. The force components; drag (F_D), lift (F_L), normal component (F_N), and tangential component (F_T). (a) General panel with arbitrary orientation and (b) a two-dimensional panel [15].

These forces (F_L and F_D) play a crucial role in understanding the behavior of net panels in aquatic environments. The fluid lift force (F_L) acts perpendicular to the direction of water flow and contributes to the upward forces experienced by

the net. On the other hand, the drag force (F_D) acts parallel to the water flow and represents the resistance encountered by the net in the direction of the flow.

The decomposed components of the environmental loads are expressed in equations 2.8 and 2.9, detailing the lift and drag forces acting on the net panel, respectively:

$$F_D = \frac{1}{2} C_d \rho A_\tau \left|\vec{V}\right|^2 i_D \tag{2.8}$$

$$F_L = \frac{1}{2} C_L \rho A_\tau \left|\vec{V}\right|^2 i_L \tag{2.9}$$

Where ρ is the fluid density, C_d and C_L are the drag coefficient and lift coefficient, $\vec{V}$ is the velocity, and i_D and i_L are the unit force vectors to indicate the directions of drag and lift forces. It's worth noting that these equations hold under specific conditions $0^\circ \leq \theta \leq 90^\circ$, where $\theta = \cos^{-1}\left|\vec{n} \cdot \vec{i}_D\right|$.

Validation and verification studies have been conducted to assess the accuracy and reliability of the Screen model. In practice, the precise determination of drag coefficients (C_D) and lift coefficient (C_L) is crucial for accurately calculating the forces exerted on structures. The selection and calibration of these coefficients significantly impact the predictive capabilities of the Screen model, as studied by numerous researchers' [15, 10, 2]. However, Screen models are rarely applied in FEM programs for dynamic simulations due to their complex implementation, especially when compared to the Morison model [6].

2.4 Wake flow

The wake flow occurs when a fluid, such as air or water, encounters a cylindrical obstacle, creating a wake downstream of the cylinder (See Figure 2.6 [12]). In the context of ocean fish cages, this phenomenon is evident as water encounters the fish cage sinker tube, floating collar, and netting, which is comprised of thousands of small net ropes with a cylindrical shape. This encounter causes the flow to diverge and form zones of varying velocity and pressure downstream. Such

wake formation is pivotal, driven by the interaction between the fluid and the cage structure, resulting in complex patterns of flow.

In the wake region, the flow behaves differently compared to the undisturbed flow upstream of the cylinder. Here, the fluid velocity decreases, and vortices form as the fluid attempts to fill the void left by the obstruction [12].

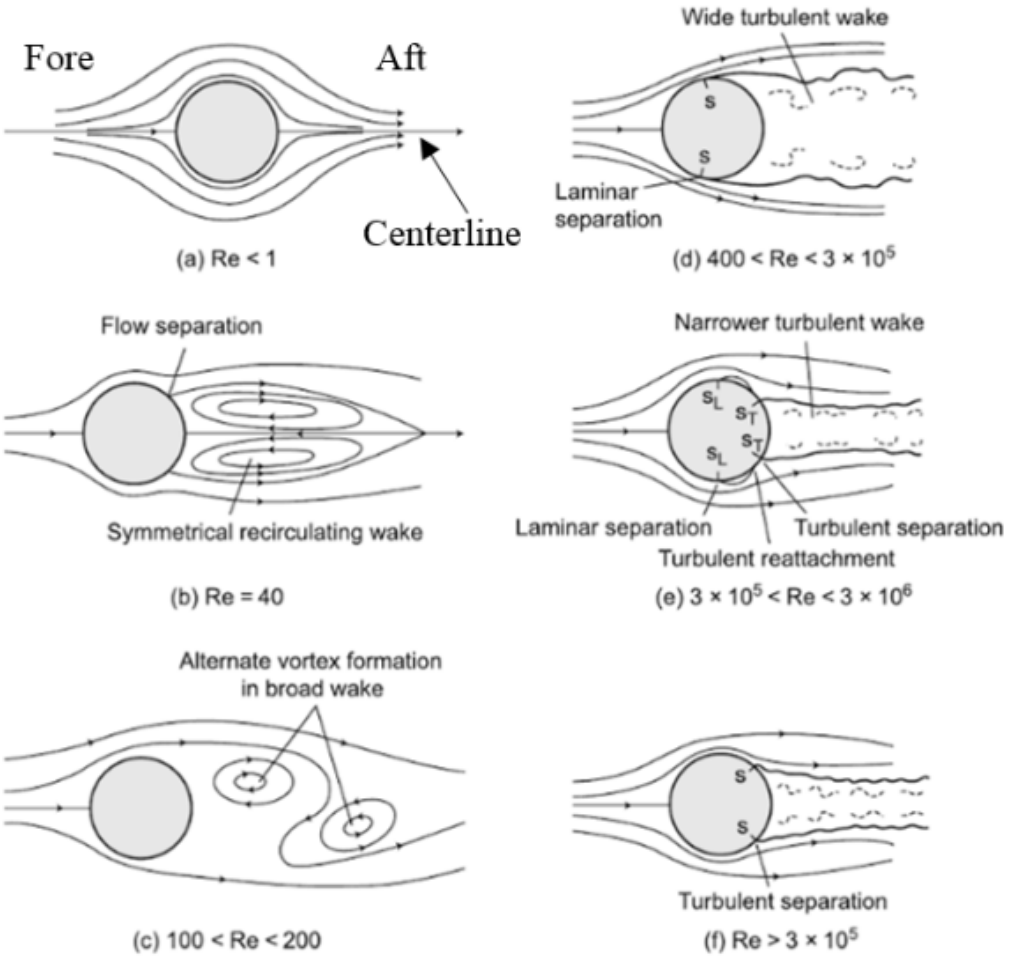

Figure 2.6: Flow over rigid circular cylinder [12]

The wake behind a cylinder is characterized by alternating zones of low and high pressure, a result of vortices shedding from the cylinder's surface. This shed-

ding occurs periodically, leading to the formation of a distinctive pattern known as the von Kármán vortex street [22], named after Theodore von Kármán.

One crucial aspect of the wake flow in ocean fish cages is its role in facilitating water exchange and nutrient transport. The turbulence generated by the cage's presence improves mixing, aiding in the dispersal of nutrients and organic matter. This process has significant implications for aquaculture practices, influencing the distribution of feed, waste, and dissolved gases, ultimately impacting the health and growth of farmed fish [14].

Additionally, the wake flow within fish cages has far-reaching effects on the surrounding environment, impacting a wide range of ecological processes. Alterations in flow patterns can affect sediment transport, benthic habitats (ocean life at seabed), and the movement of planktonic organisms. Understanding these interactions is essential for sustainable aquaculture management, enabling the mitigation of potential environmental impacts and the optimization of cage placement and design.

2.5 Regular and irregular waves

Wave-Structure Interaction

Waves interact with offshore structures through wave loading, wave-induced motion, and structural response. The dynamic interaction between waves and structures can lead to significant stresses and forces acting on the structure. Further affecting its stability and performance. Employing sophisticated numerical modeling techniques, such as computational fluid dynamics (CFD) and finite element analysis (FEA), it is possible to simulate wave-structure interaction and predict the structural response under various wave conditions [5].

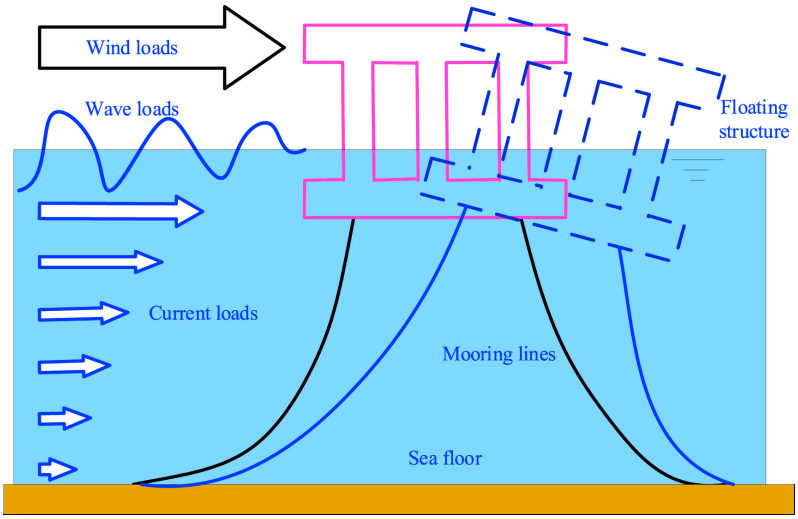

Figure 2.7: Illustration of a wave-structure interaction, by Zhao et al. (2020) [29].

Wave loading refers to the pressure exerted by waves on the surface of the structure, which can cause bending, fatigue, and instability [25]. Wave-induced motion includes the heave, pitch, and roll motions experienced by floating structures in response to wave action. Structural response involves analyzing the deformation and stresses within the structure resulting from wave loading and motion. By understanding and accurately predicting wave-structure interaction, engineers can optimize the design of offshore platforms, ships, and aquaculture structures to ensure their safety and reliability in marine environments.

2.5.1 Regular Waves

Regular waves in offshore marine environments are characterized by a consistent and predictable pattern of oscillations. These waves result from harmonic motion, where water particles move in a sinusoidal manner with uniform frequency and amplitude. Implying that the peaks and valleys of regular waves exhibit a recurring pattern, making them relatively easy to analyze and predict.

The properties of regular waves, such as their wavelength, period, and amplitude, can be precisely defined and controlled, making them valuable for experimental research and engineering design. The wave period, which refers to the

time interval between successive wave crests passing a fixed point, directly influences the dynamic response of offshore structures [8]. By subjecting structural models to regular waves of varying periods and amplitudes in laboratory wave tanks, engineers can assess the structural integrity and performance of offshore platforms, ships, and coastal infrastructure under different wave conditions. Additionally, regular waves serve as a fundamental component in theoretical models and numerical simulations used to predict wave behavior and its impact on marine structures.

Wave Parameters

The properties of regular waves, such as wavelength, period, and amplitude, play a crucial role in determining their behavior and impact on offshore structures. The wavelength (λ) is the distance between two consecutive wave crests (or troughs), and it determines the spatial extent of the wave pattern. The period (T) is the time it takes for one complete wave cycle to pass a fixed point, while the amplitude (A) represents the maximum displacement of water particles from their undisturbed position. Figure 2.8 shows an example of a regular wave with the mentioned wave parameter [1].

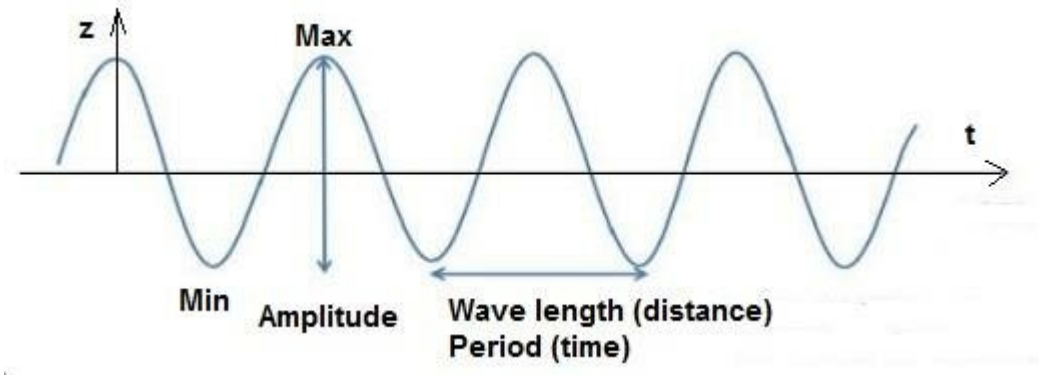

Figure 2.8: Example of a regular wave [1].

These wave parameters are interconnected and influence various aspects of wave dynamics, including wave speed, energy, and power. For example, longer wavelengths typically result in faster wave propagation speeds, while higher wave

amplitudes correspond to increased wave energy. Engineers use mathematical relationships between these parameters to characterize wave behavior and design offshore structures capable of withstanding different wave conditions.

2.5.2 Irregular Waves

In contrast to regular waves, irregular waves in offshore marine environments lack a consistent and predictable pattern of oscillations. Instead, they exhibit random variations in wave height, period, and direction, resulting from the superposition of waves generated by various meteorological and oceanographic processes. Irregular waves are prevalent in natural marine environments, where factors such as wind, storms, and seafloor topography contribute to the complex and unpredictable nature of wave motion.

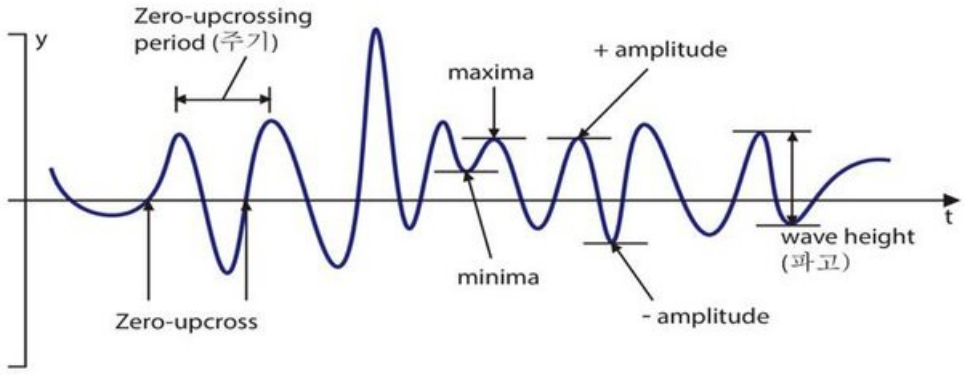

Figure 2.9: Example of an irregular wave [21].

The irregularity of waves poses significant challenges for offshore engineering and design, as predicting and mitigating their effects on marine structures can be difficult. Unlike regular waves, which can be characterized by simple mathematical equations, irregular waves require sophisticated statistical methods and computational models for analysis and prediction. Engineers often employ techniques such as spectral analysis and wave hindcasting to characterize the statistical

properties of irregular waves and assess their impact on offshore structures over extended periods.

Spectral analysis is a commonly used technique for characterizing the statistical properties of irregular waves, such as wave spectra and significant wave heights. Wave hindcasting, on the other hand, involves using numerical simulations to reconstruct historical wave conditions based on observational data, providing valuable insights into wave climate and extreme wave events. By integrating these approaches, researchers can develop comprehensive models for predicting wave behavior and assessing its impact on offshore structures over extended periods.

Wave parameters

The *significant wave height (H_s)* is a statistical measure commonly used to describe the average height of the highest one-third of waves in a wave record. It provides a useful indication of the overall wave energy. H_s is typically estimated from measured wave data or through numerical simulations, considering factors such as wave spectra and wave steepness.

The *peak wave period (T_p)* refers to the time interval between successive peaks of the highest waves in a wave record. It represents the dominant wave period and is closely related to the wave energy and wave spectrum. T_p is used for assessing wave dynamics and structural response, as it influences wave loading and wave-induced motion.

Wave steepness (H/L) is the ratio of wave height (H) to wavelength (L) and provides an indication of wave shape and steepness. It affects wave breaking, wave stability, and wave-induced forces on offshore structures.

Wave spectrum

The wave spectrum is a graphical representation of the distribution of wave energy across different frequencies and wave heights. It provides valuable insights into wave characteristics and predicts their impact on offshore structures. Common wave spectra models include the Pierson-Moskowitz spectrum and the Jonswap

spectrum, which are widely used in offshore engineering for analyzing wave dynamics and designing marine structures.

The Jonswap spectrum is a widely accepted model for describing the energy distribution of wind-generated waves, particularly in deep-water environments. The Jonswap spectrum is defined in Equation 2.10 [20]. It is based on the assumption that wave energy spectra follow a power-law distribution, with the spectral peak frequency influenced by the wind speed and duration of wind forcing. By fitting observed wave data to the Jonswap spectrum, researchers can estimate parameters such as significant wave height and peak wave period, providing valuable insights into the statistical properties of irregular waves.

$$S(f) = \frac{\alpha g^2}{16\pi^4} f^{-5} exp\left[-\frac{5}{4}(\frac{f}{f_m})^{-4}\right]\gamma^b \tag{2.10}$$

where;

$$b = exp\left[-\frac{1}{2\sigma^2}(\frac{f}{f_m} - 1)^2\right] \tag{2.11}$$

and σ => σ_1 for $f \leq f_m$, σ_2 for $f > f_m$.

Despite their complexity, irregular waves represent the true nature of wave conditions in offshore marine environments, making them essential for realistic and comprehensive engineering assessments. By accounting for the variability and randomness inherent in irregular waves, engineers can design offshore structures that are robust and resilient to the dynamic forces exerted by ocean waves, ensuring their safety and longevity in challenging marine environments.

References

[1] Arifin Arifin et al. “Numerical Prediction Of Foils Configuration In A Design of Buoy Glider System For Supporting Tsunami Early Warning”. In: *IOP Conference Series: Materials Science and Engineering* 1052 (Jan. 2021), p. 012017. DOI: 10.1088/1757-899X/1052/1/012017.

[2] Cheslav Balash et al. “Aquaculture Net Drag Force and Added Mass”. In: *Aquacultural Engineering* 41.1 (2009), pp. 14–21. ISSN: 0144-8609. DOI: https://doi.org/10.1016/j.aquaeng.2009.04.003. URL: https://www.sciencedirect.com/science/article/pii/S0144860909000338.

[3] J.S. Bessonneau and D. Marichal. “Study of the dynamics of submerged supple nets (applications to trawls)”. In: *Ocean Engineering* 25.7 (1998), pp. 563–583. ISSN: 0029-8018. DOI: https://doi.org/10.1016/S0029-8018(97)00035-8. URL: https://www.sciencedirect.com/science/article/pii/S0029801897000358.

[4] Pål Bore, Jørgen Amdahl, and David Kristiansen. “Modelling of Hydrodynamic Loads on Aquaculture Net Cages by a Modified Morison Model”. In: (May 2017). URL: https://www.researchgate.net/publication/319199317_Modelling_of_Hydrodynamic_Loads_on_Aquaculture_Net_Cages_by_a_Modified_Morison_Model.

[5] L.F. Chen et al. “Numerical investigation of wave–structure interaction using OpenFOAM”. In: *Ocean Engineering* 88 (2014), pp. 91–109. ISSN: 0029-8018. DOI: https://doi.org/10.1016/j.oceaneng.2014.06.003. URL: https://www.sciencedirect.com/science/article/pii/S0029801814002169.

[6] Hui Cheng. “Position based dynamics”. In: *Development of Advanced Numerical Tools for Dynamic Analysis of Aquaculture Structures* (2022). https://uis.brage.unit.no/uis-xmlui/handle/11250/2992729, pp. 1–343. ISSN: 1890-1387.

[7] J. DeCew et al. “Modeling of dynamic behavior of a single-point moored submersible fish cage under currents”. In: *Aquacultural Engineering* 43.2 (2010), pp. 38–45. ISSN: 0144-8609. DOI: https://doi.org/10.1016/j.aquaeng.2010.05.002. URL: https://www.sciencedirect.com/science/article/pii/S0144860910000312.

[8] M.C. Deo. *Waves and Structures*. Online; accessed April 15th 2024.

[9] DNV. *DNV-RP-C205, Environmental Conditions and Environmental Loads*. 2014.

[10] Løland Geir, Jan Aarsnes, and H. Rudi. “Current forces on cage, net deflection.” In: (Oct. 1990).

[11] AKVA Group. *User manual nets - revision 8, February 2022.pdf*. URL: https://www.akvagroup.com/nets/.

[12] Harika Gurram. “Effect of the Wake Structure on Drag Coefficient for a Thin Flexible Wire”. In: *Theses and Dissertations*. 447 (2017), pp. 3–47. URL: https://repository.fit.edu/etd/447/.

[13] indiamart. *HDPE Fishing Net*. [Online; accessed February 24, 2024]. URL: https://m.indiamart.com/proddetail/hdpe-fishing-net-20586423155.html.

[14] Pascal Klebert and Biao Su. “Turbulence and flow field alterations inside a fish sea cage and its wake”. In: *Applied Ocean Research* 98 (2020), p. 102113. ISSN: 0141-1187. DOI: https://doi.org/10.1016/j.apor.2020.102113. URL: https://www.sciencedirect.com/science/article/pii/S0141118719306716.

[15] Trygve Kristiansen and Odd M. Faltinsen. “Modelling of current loads on aquaculture net cages”. In: *Journal of Fluids and Structures* 34 (2012), pp. 218–235. ISSN: 0889-9746. DOI: https://doi.org/10.1016/j.jfluidstructs.2012.04.001. URL: https://www.sciencedirect.com/science/article/pii/S0889974612000783.

[16] Pål Lader et al. “Forces on a cruciform/sphere structure in uniform current”. In: *Ocean Engineering* 82 (2014), pp. 180–190. ISSN: 0029-8018. DOI: https://doi.org/10.1016/j.oceaneng.2014.03.007. URL: https://www.sciencedirect.com/science/article/pii/S0029801814000882.

[17] Chun-Woo Lee et al. “Dynamic simulation of a fish cage system subjected to currents and waves”. In: *Ocean Engineering* 35.14 (2008), pp. 1521–1532. ISSN: 0029-8018. DOI: https://doi.org/10.1016/j.oceaneng.2008.06.009. URL: https://www.sciencedirect.com/science/article/pii/S0029801808001303.

[18] John Morison, J. W. Johnson, and Samuel A. Schaaf. “The Force Exerted by Surface Waves on Piles”. In: *Journal of Petroleum Technology* 2 (1950), pp. 149–154. URL: https://api.semanticscholar.org/CorpusID:110216127.

[19] Orcaflex. *Morison's equation*. [Online; accessed February 27, 2024]. URL: https://www.orcina.com/webhelp/OrcaFlex/Content/html/Morison'sequation.htm.

[20] Orcaflex. *Waves: Wave spectra*. Online; accessed April 15th 2024. URL: https://www.orcina.com/webhelp/OrcaFlex/Content/html/Waves,Wavespectra.htm.

[21] Heeyoung Park, Cheongtag Kim, and Youngjin Park. “The Variables of Surface of Revolution and its effects on Human Visual Preference”. In: *Journal of the Korea Computer Graphics Society* 28 (Sept. 2022), pp. 31–40. DOI: 10.15701/kcgs.2022.28.4.31.

[22] L. Skrbek and W.F. Vinen. “Quantum Turbulence”. In: *Profress in Low Temperature Physics* 16 (2009), pp. 1–414. DOI: https://doi.org/10.1016/j.apor.2020.102113. URL: https://www.sciencedirect.com/bookseries/progress-in-low-temperature-physics/vol/16/suppl/C.

[23] InCord Custom Safety Netting Solution. *N815BK*. [Online; accessed February 24, 2024]. URL: https://incord.com/product/n815bk/.

[24] Tsutomu Takagi et al. “Validity and layout of “NaLA”: a net configuration and loading analysis system”. In: *Fisheries Research* 66.2 (2004), pp. 235–243. ISSN: 0165-7836. DOI: https://doi.org/10.1016/S0165-7836(03)00204-2. URL: https://www.sciencedirect.com/science/article/pii/S0165783603002042.

[25] Peter Tromans and Luc Vanderschuren. “WAVE LOADS ON OFFSHORE STRUCTURES”. In: Mar. 2018.

[26] Igor Tsukrov et al. “Characterization of geometry and normal drag coefficients of copper nets”. In: *Ocean Engineering* 38.17 (2011), pp. 1979–1988. ISSN: 0029-8018. DOI: https://doi.org/10.1016/j.oceaneng.2011.09.019. URL: https://www.sciencedirect.com/science/article/pii/S0029801811002137.

[27] R. Wan et al. “Statics of a gillnet placed in a uniform current”. In: *Ocean Engineering* 31.14 (2004), pp. 1725–1740. ISSN: 0029-8018. DOI: https://doi.org/10.1016/j.oceaneng.2004.02.005. URL: https://www.sciencedirect.com/science/article/pii/S0029801804000678.

[28] WAYSAIL. *Fishing Net PET Net*. [Online; accessed February 24, 2024]. URL: https://www.qdwaysail.com/fishing-net-pet-net.html.

[29] Yuliang Zhao and Sheng Dong. “A multi-load joint distribution model to estimate environmental design parameters for floating structures”. In: *Ocean Engineering* 217 (2020), p. 107818. ISSN: 0029-8018. DOI: https://doi.org/10.1016/j.oceaneng.2020.107818. URL: https://www.sciencedirect.com/science/article/pii/S0029801820307927.

[30] Yun-Peng Zhao et al. “Numerical simulation of the effects of structure size ratio and mesh type on three-dimensional deformation of the fishing-net gravity cage in current”. In: *Aquacultural Engineering* 36.3 (2007), pp. 285–301. ISSN: 0144-8609. DOI: https://doi.org/10.1016/j.aquaeng.2007.01.003. URL: https://www.sciencedirect.com/science/article/pii/S0144860907000027.

Chapter 3

Numerical study on the lifting operation of a gravity-type fish cage

This content is published as part of the marine and offshore technology project, and part of it is published as a conference paper:
A. Gjerde, X. Wen and M.C. Ong, 2023, Numerical study on the lifting operation of a gravity-type fish cage. Mater. Sci. Eng. 1294 012017. DOI 10.1088/1757-899X/1294/1/012017.

Abstract

The dynamic behaviors of the lifting operations of a gravity-type fish cage under calm sea conditions are investigated in this study using an extended position-based dynamics (XPBD) method. The structural deformations of the aquaculture nets and the lifting forces are obtained. The original XPBD is improved to accurately predict the tensions of the aquaculture nets by applying correction forces. The present XPBD is validated against the experimental results of a flexible horizontal net. The time-step sensitivity is verified for the case of a lifting operation of the fish cage. Results show that the lifting force increases rapidly resulting from the weight of the sinkers at the bottom of the side net. The maximum tension of the net is located at the net ropes connected to the center point of the bottom net. For the damaged nets with broken net rope at the bottom net, the lifting force and tension of the net do not have significant changes. The structure of the bottom net should be enhanced for safe lifting operations.

Keywords:

Aquaculture; gravity-type fish cage; lifting operations; extended position-based dynamics.

3.1 Introduction

Fish cages are the most used equipment in aquaculture [6, 5, 10]. As technology advances, the number of different types of fish cages used in aquaculture are becoming less [2]. The gravity-type fish cages have become the more frequently used as a fish cage for the aquaculture in many countries such as Norway, China, and Japan. The gravity-type fish cages usually consist of aquaculture nets made of nylon or polyethylene (PE), high-density polyethylene (HDPE) floating collars and sinker tubes, concrete center sinker at the bottom of the net and related mooring system. All the materials can be produced in the manufactories and transported to specific sea sites to be assembled. The usage of the gravity-type fish cages can help reduce the capital cost for the industrial-scaled fish farming. Another important way to increase to the harvest and the profits of the industrial-scaled fish farming is to ensure the health and the good quality of the fish by monitoring the sea lice and conducting the de-lice operations [1]. One type of de-lice operations is to pump the fish into the de-lice machines and clean the fish by fresh water. Before the de-lice of the fish, the aquaculture nets need to be lifted and the fish will gather for pumping. The extra oxygen supply is required when the fish is gathering. The lifting operation is conducted by a crane installed on a vessel, which is very similar to the harvest operation. The lifting operations of a gravity-type fish cage are important for the fish farming and the dynamic response of the fish cage during the lifting operation is investigated in the present study.

A numerical method is adopted to study the dynamic response of the fish cage during the lifting operation in the present study. For numerical simulations, there are a few approaches and methods that can be used, such as finite element method (FEM) [4], OrcaFlex [3], and mass-spring model [7]. Rui Dou [4] used the FEM method together with a panel model, a mass model and Morison model [5] to model and analyse a semi-submersible fish cage. Cifuentes and Kim [3] calculated the current load acting on a fish cage using a Morison-force model applied at instantaneous positions of equivalent-net modeling using Orcaflex [3]. Lee et al. (2005) used the mass-spring model to simulate the flexible structures' behavior to understand the movements and design an appropriate system [7]. A new efficient method called extended position-based dynamic (XPBD) method [9, 8]

was proposed to simulate the cloth dynamics in games. It is an implicit method and more robust compared with the explicit method of mass-spring model. The method will be used in the present study to simulate the dynamic behaviors of the flexible fish cage. The present study focuses on the dynamic analysis of the lifting operations of a gravity-type fish cage using the XPBD method. The present paper is organized as follows. The fish cage specifications and the XPBD method is given in Section 2. Section 3 presents a validation case of a flexible horizontal net, and the results and discussions of the dynamic process of the lifting operations of the normal and damaged fish cages. The conclusions are summarized in Section 4.

3.2 Numerical Model

3.2.1 Fish cage specifications

Figure 3.1 displays the full-scale structure of a gravity-type fish cage. The cage has a circumference of 160m and a total height of 35m. It consists of two main parts: a 30m high side net and a 5m high bottom net. The fish cage includes thousands of panels which are enclosed by net ropes. The net ropes are constructed using PE lines. For the side net, each net rope has a length of 1.25m. The bottom net has 8 net ropes from the center to the outer boundary and 128 net ropes at the outer boundary. Inside the net panels, there are small inner nets made of nylon with square mesh patterns. These inner nets have a diameter of 2.85mm and a length of 25mm. There are side net sinkers installed at the bottom of the side net and a center sinker installed at the center point of the bottom net. Table 1 shows the specifications of the gravity-type fish cage, including the dimensions, materials, and key features.

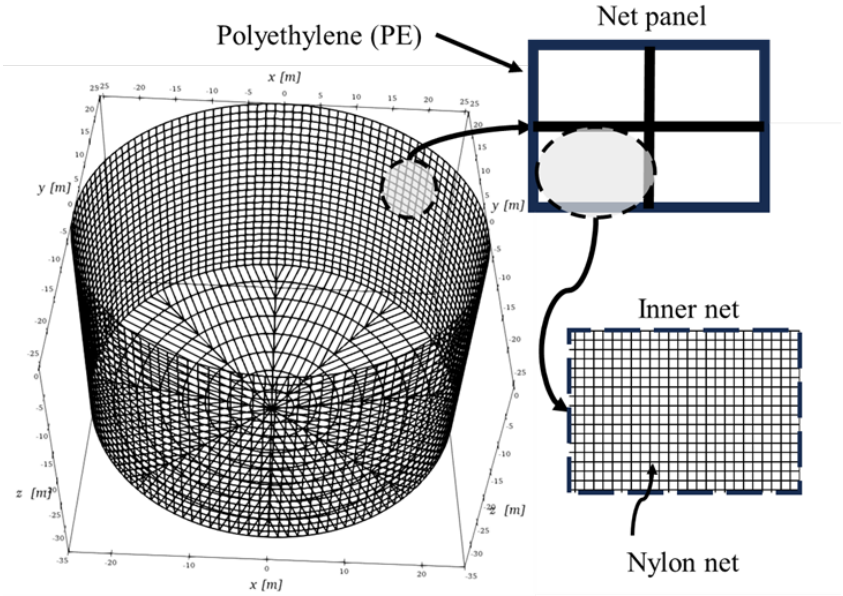

Figure 3.1: Illustration of the fish cage structure and the net design.

Table 3.1: Specifications of the gravity-type fish cage.

	Unit	Value
Cage circumference	m	160
Cage height	m	35
Side net height	m	30
Bottom net height	m	5
Side net sinkers' mass	kg/m	80
Bottom net sinker's mass	kg	200
Polyethylene Density	kg/m^3	960
Nylon Density	kg/m^3	1140
Elastic modulus polyethylene	Pa	1.5e9
Net rope diameter (PE)	mm	10
Inner twine diameter (nylon)	mm	2.85
Length inner net	mm	25
Solidity Sn	-	0.2

During the lifting operation of the fish cage, the center point of the bottom net is lifted from the lowest point to a specific position. The present lifting speeds are 0.25m/s, 0.5m/s, and 1m/s, as shown in Figure 3.2. For the lifting speed of 0.25m/s, the crane starts at 0s and accelerates to the normal lifting speed in 20s. The crane totally stops at 200s. The crane acceleration times for 0.5 m/s and 1 m/s are 10 seconds and 5 seconds, respectively. Additionally, the cranes totally stop at 100 seconds and 75 seconds for 0.5 m/s and 1 m/s, respectively.

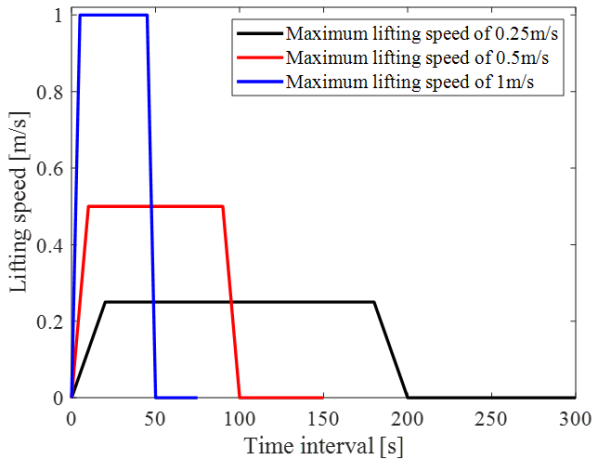

Figure 3.2: Description of the lifting speeds of 0.25m/s, 0.5m/s, and 1m/s during the lifting operation of the fish cage.

3.2.2 XPBD Method

The extended position-based dynamics (XPBD) is an implicit method and serves as a numerical simulation technique used for simulating complex dynamic behavior of deformable objects, making it a valuable tool for investigating the fish case behavior and optimizing the design parameters. XPBD was developed as an extension of the position-based dynamics (PBD) approach, introducing distinct advantages in terms of stability, easy implementations, and computational efficiency. Algorithm 1 shows the original XPBD simulation loop.

Algorithm 1: original XPBD simulation loop	
1:	predict position $\tilde{\boldsymbol{x}} \leftarrow \boldsymbol{x}^n + \Delta t \boldsymbol{v}^n + \Delta t^2 \boldsymbol{M}^{-1} \boldsymbol{F}_{ext}$
2:	**for all** constrains **do**
3:	compute $\Delta\lambda$ using Equation (7)
4:	compute Δx using Equation (6)
5:	**end for**
6:	update positions $\boldsymbol{x}^{n+1} \leftarrow \tilde{\boldsymbol{x}} + \Delta \boldsymbol{x}$
7:	update velocities $\boldsymbol{v}^{n+1} \leftarrow \frac{1}{\Delta t}(\boldsymbol{x}^{n+1} - \boldsymbol{x}^n)$

The method first updates the positions of the nodes based on the external forces $\mathbf{F}_{ext}$ using Newton's second law. Then, the positions of the nodes need to be corrected according to the inner force resulting from every constraint. For a single constraint, the changing of the positions of these two nodes is given by evaluating Equation (3.1 - 3.2).

$$\Delta \mathbf{X_1} = +\Delta\lambda m_1^{-1} \mathbf{q} \tag{3.1}$$

$$\Delta \mathbf{X_2} = -\Delta\lambda m_2^{-1} \mathbf{q} \tag{3.2}$$

The changing of Lagrange multiplier λ is given by Equation (3.3).

$$\Delta\lambda = \frac{-C}{m_1^{-1} + m_2^{-1} + \tilde{\alpha}} \tag{3.3}$$

Where $\tilde{\alpha} = \frac{1}{k\Delta t^2}$ and $C = l - l_0$.

Compared with the mass spring model, XPBD can provide a quick result for the net dynamics in an implicit way. However, XPBD has its inevitable error for calculating the tensions of the constraints. It is because the masses of the nodes are involved when evaluating the Lagrange multiplier change. It is against the physics intuition that the elastic force is only determined by the stiffness and the constraint. To correct the results of XPBD, the term of $m_1^{-1} + m_2^{-1}$ in the denominator of Equation (3.3) should be removed. However, the simulation loop as shown in Table 1 will become unstable if $m_1^{-1} + m_2^{-1}$ is removed. To maintain the stable simulation loop and correct the results of XPBD at the same time, an

XPBD correction is proposed by applying extra forces acting on the two nodes of the constraint, where the expression is shown in Equation (3.4 - 3.5).

$$\mathbf{F_1} = +\gamma\mathbf{q} \tag{3.4}$$

$$\mathbf{F_2} = -\gamma\mathbf{q} \tag{3.5}$$

Where γ is evaluated by Equation (3.6).

$$\gamma = \frac{-C(m_1^{-1} + m_2^{-1})}{(m_1^{-1} + m_2^{-1} + \tilde{\alpha})\tilde{\alpha}\Delta t^2} \tag{3.6}$$

The new simulation loop is shown in Algorithm 2. Before predicting the position, the correction forces $\mathbf{F}_{cor}$ are calculated for every constraint. It will increase the computational cost when using the same time step and the same structure configuration. However, a small-time step close to the mass-spring model as shown in Equation (3.4 - 3.5) is required to ensure a close prediction accuracy, which reduces the advantage of an implicit method of XPBD. The present modified XPBD not only enhances the precision of predictions and but also significantly lowers computational expenses. As a result, the previously incurred drawback of introducing correction force calculations is effectively mitigated.

Algorithm 2: modified XPBD simulation loop	
1:	**for all** constrains **do**
2:	compute γ using Equation (4)
3:	compute correction force $\boldsymbol{F}_{cor}$ using Equation (3)
4:	**end for**
5:	predict position $\tilde{\boldsymbol{x}} \leftarrow \boldsymbol{x}^n + \Delta t\boldsymbol{v}^n + \Delta t^2 M^{-1}[\boldsymbol{F}_{ext} + \boldsymbol{F}_{cor}]$
6:	**for all** constrains **do**
7:	compute $\Delta\lambda$ using Equation (2)
8:	compute Δx using Equation (1)
9:	**end for**
10:	update positions $\boldsymbol{x}^{n+1} \leftarrow \tilde{\boldsymbol{x}} + \Delta\boldsymbol{x}$
11:	update velocities $\boldsymbol{v}^{n+1} \leftarrow \frac{1}{\Delta t}(\boldsymbol{x}^{n+1} - \boldsymbol{x}^n)$

3.3 Results and Discussions

3.3.1 Validation study

The validation case is based on Lee et al.'s [7] experimental test of a flexible horizontal net, as shown in Figure 3.3 in its top view. The net consists of 214 nodes and 424 line elements. The twine length is 100mm in the inner net and 141.4mm on the boundaries. The twine diameter is 0.4 mm. Additionally, the net incorporates three sinkers with masses: F1 = 1.5kg (middle), F2 = 0.5kg (left), and F3 = 0.7kg (right). The specifications of the flexible horizontal net are shown in Table 4. During the experiment, the four corner nodes were fixed. The three sinkers are dropped from the initial positions and reached their final positions as shown in Figure 3.4(a). During the calculations, the velocities of each node are damped into 99% at every 0.5ms to approach the final convergent position of the flexible horizontal net. Figure 3.4(b) presents the results of the final position of the flexible horizontal net obtained using three time-steps of 0.025ms, 0.05ms and 0.1ms. The results of the three time-steps exhibit a good agreement and they show good consistent with the experiment result, which confirms the feasibility of the present XPBD method used to simulate the flexible fish cage.

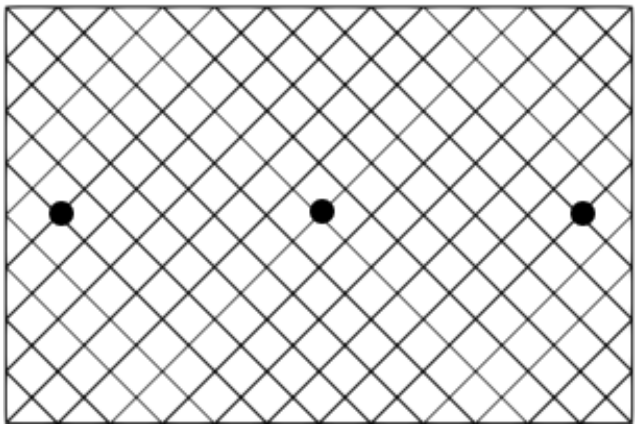

Figure 3.3: Initial position of the flexible horizontal net (top view).

Table 3.2: Validation case specifications.

Parameters	Values
Net dimensions (meshes)	12x8
Node number	214
Element number	424
Stiffness	15 000 N/m
Mass	0.0015 kg
Twine diameter	0.4 mm
Half mesh size	100mm
Sinker 1's mass	1.5 kg
Sinker 2's mass	0.5 kg
Sinker 3's mass	0.7kg

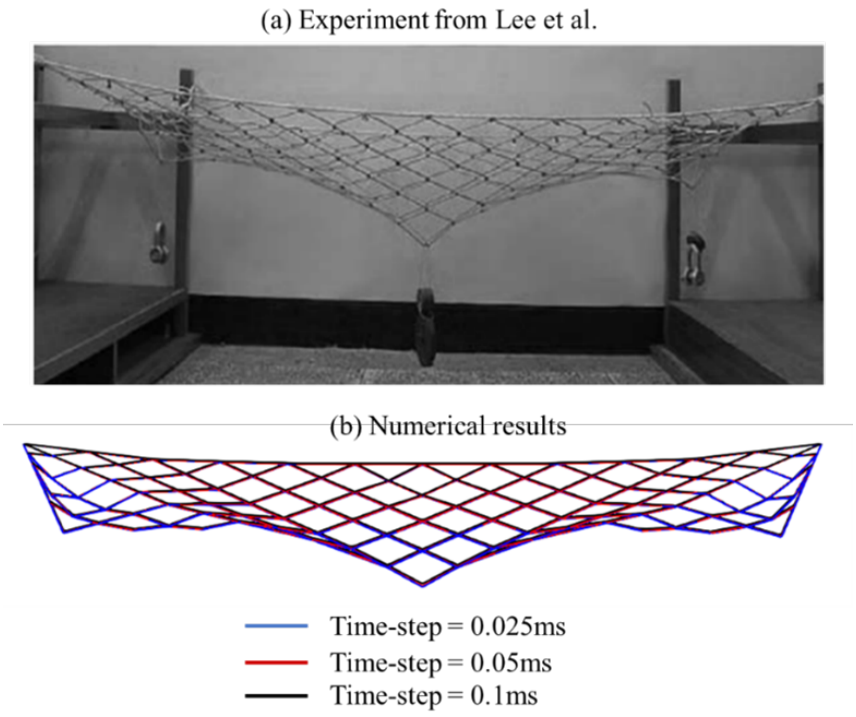

Figure 3.4: Comparison between the experiment result of Lee et al. [7] (a) and the numerical results of the present XPBD (b).

3.3.2 Lifting operation of a normal gravity-type fish cage

Before the lifting operation, the initial position of the fish cage is calculated using the similar way of the validation case. Figure 3.5 shows a time-step sensitivity study of the lifting force acting on a fish cage in still water. Three time-steps of 0.25ms, 0.5ms and 1ms are examined in this analysis. The results of all the tested time-steps exhibit remarkable agreement. Consequently, the time-step of 1ms is chosen as the preferred time-step for subsequent calculations to reduce the computational cost.

Figure 3.5 shows the time-step sensitivity studies of the tensions of the fish cage in XZ- and YZ-planes at 50s. There is a slight reduction in tension on one side of the cage during the initial phase of the lifting operation, specifically at the time-step of 0.25ms in XZ-plane. The overall tensions remain uniform across all time-steps, while some variations in tension are observed during the lifting of the net. Looking at the results of the time-step of 0.25ms in Figure 3.6, the maximum tension reaches 1400N.

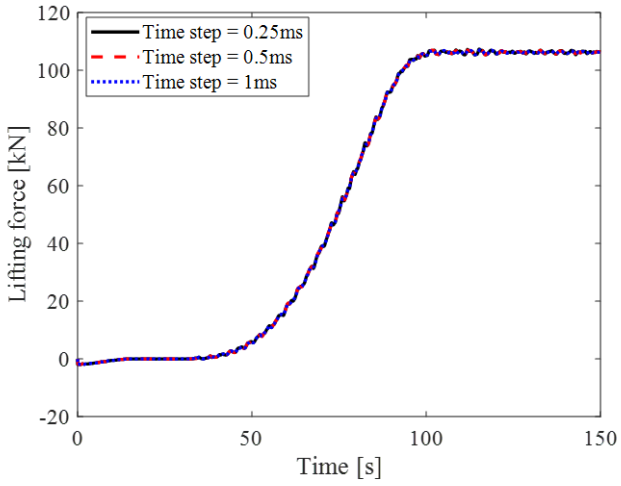

Figure 3.5: Time-step sensitivity study of the lifting force acting on the fish cage.

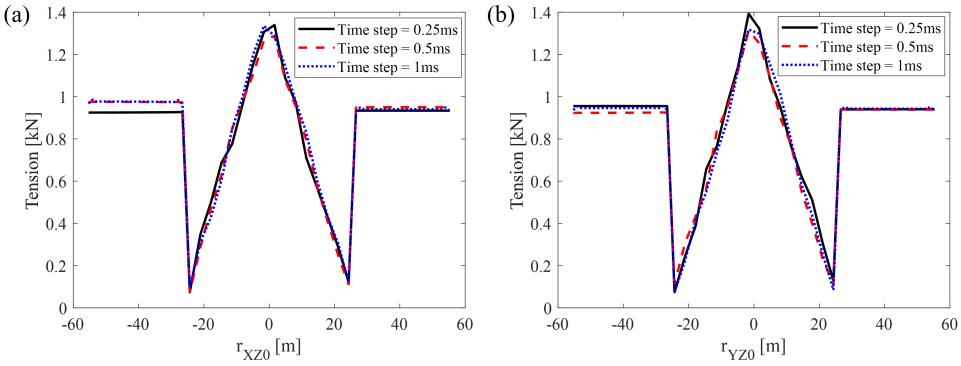

Figure 3.6: Time-step sensitivity study of the tensions of the fish cage in (a) XZ- and (b) YZ-planes at 50s.

As shown in Figure 3.5, the lifting force is small in [0s, 50s] and quickly increases over a short duration of [50s, 100s]. The force keeps the same value as the crane stops operation. The reason for the rapid increase of the lifting force is that the bottom net starts to support the weight of the sinkers at the bottom of the side net in [50s, 100s]. Figures 3.7 shows the comparisons of tensions in XZ- and YZ-planes at different time during the lifting operation. The time instants shown in this figure are chosen as 50s, 75s, and 100s. As can be seen, the tension on the bottom net has a significant increase in [50s, 100s]. The maximum tension can reach 12.5kN, which is almost 13 times of the value of the side net in Figure 3.7. The reason can be attributed to the special structure of the bottom net. As can be seen from the deformations and tensions of the fish cage in side- and top views at different times in Figure 3.8, the maximum tension of the net is observed to be located at the net ropes connected to the center point of the bottom net. Only eight net ropes support the sinkers' weight, while for the side net, there are 128 net ropes supporting the total sinkers' weight. It can be concluded that the net ropes of the bottom net experience the maximum tension during the lifting operation of a fish cage. The structure of the bottom net, especially for the eight net ropes, should be enhanced.

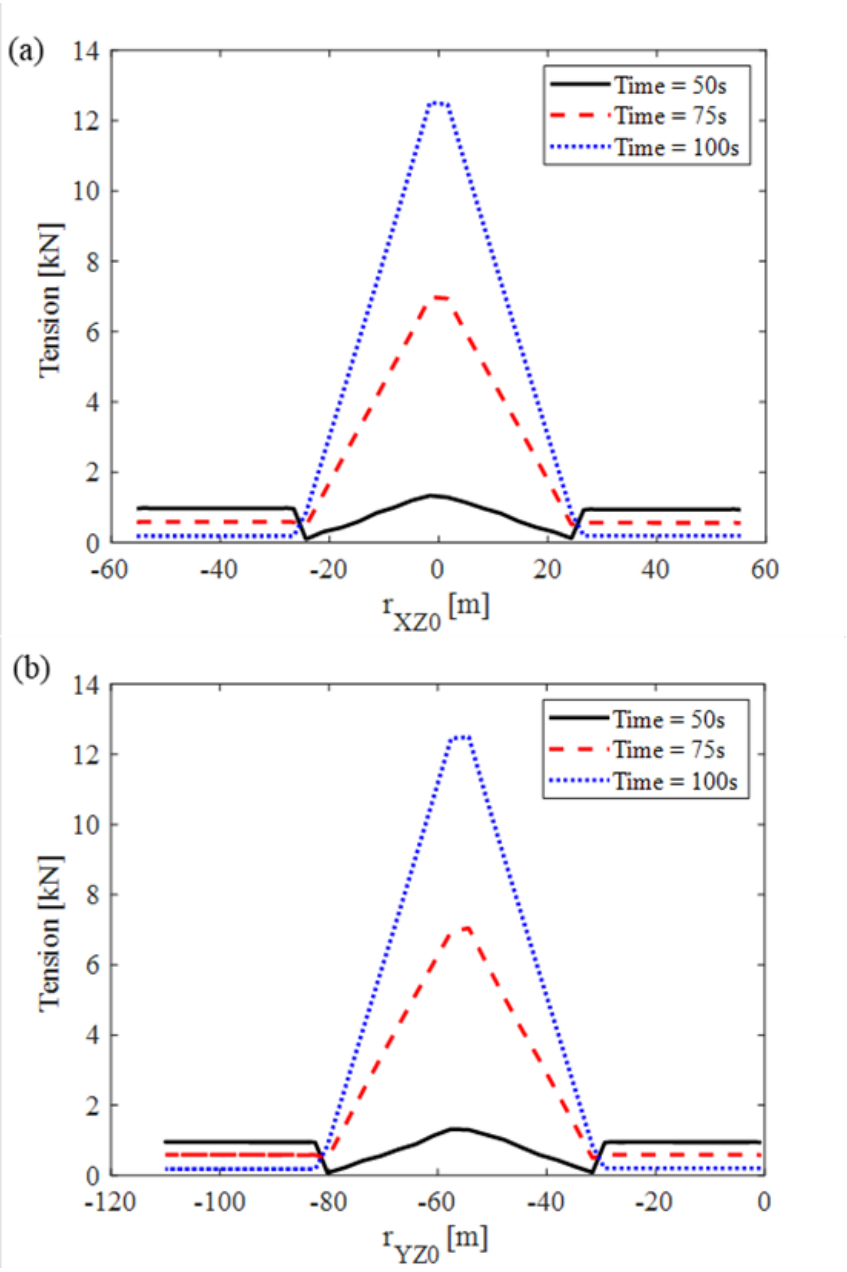

Figure 3.7: Comparisons of tensions in (a) XZ- and (b) YZ-planes at different time during the lifting operation, with lifting speed of 0.5m/s and 1ms time step.

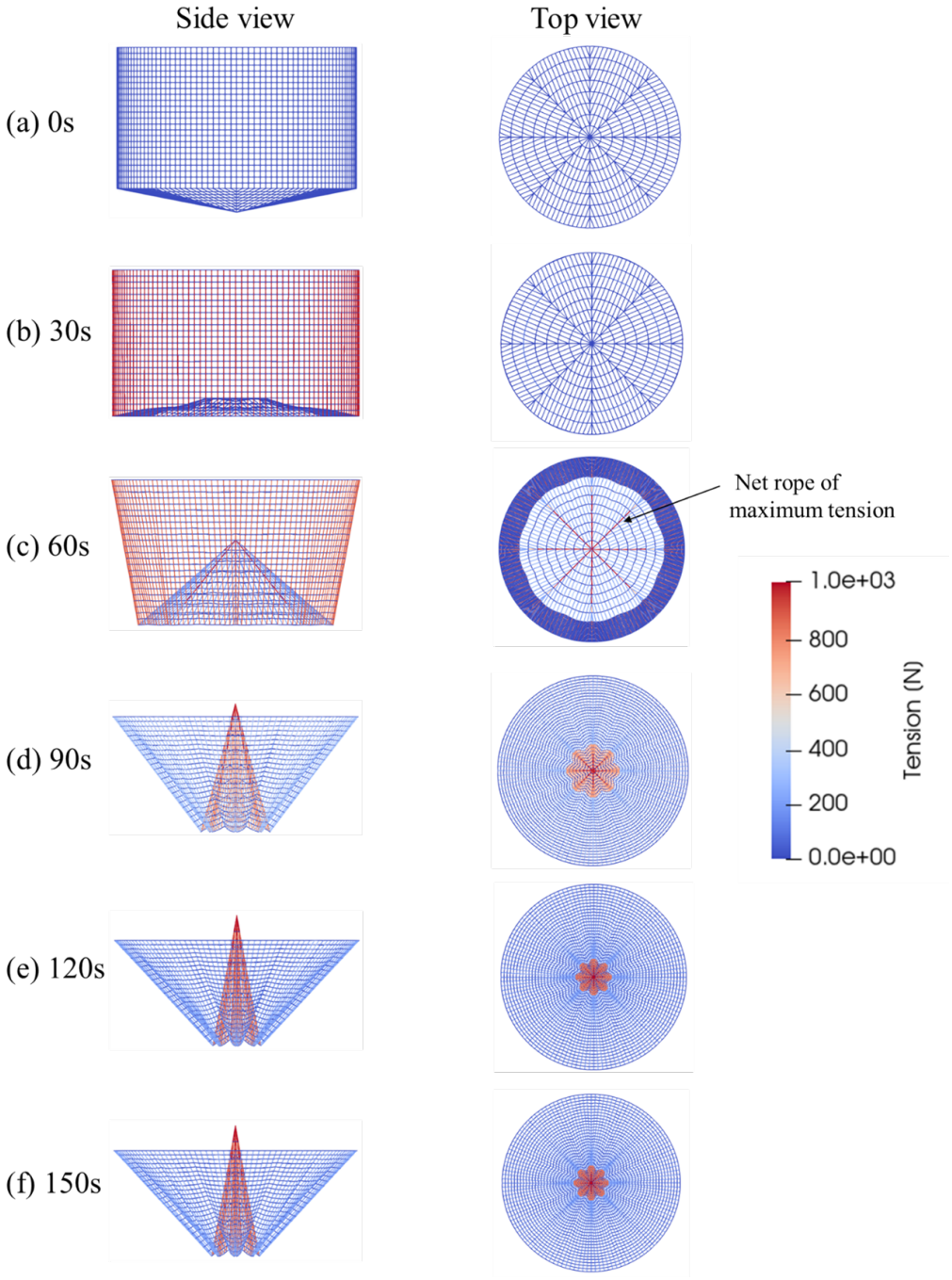

Figure 3.8: Deformations and tensions of the fish cage from (a) 0s to (f) 150s, with time increments of 30s, of a lifting operation with a lifting speed of 0.5m/s and time-step of 1ms, in side-view and top-view.

3.3.3 Effects of the maximum lifting speed

Figures 3.9 show the comparisons of lifting force for the lifting speeds with their respective time histories shown in Figure 3.2. The lifting speeds in this figure are 0.25m/s, 0.5m/s, and 1m/s. The maximum lifting force can be found for the lifting speed of 1 m/s reaching 111.6kN. It can be observed that the fish cage will experience more fluctuations in the lifting force when the lifting speed is increased. The maximum lifting force for the lifting speed of 0.25m/s and 0.5m/s are 106.5kN and 107kN, respectively. The maximum lifting forces of these two speeds are relatively similar. Therefore, the lifting speed should be reduced for smooth transitions and to avoid the fluctuation of forces when the crane totally stops.

Figure 3.10 shows the comparisons of tensions in the XZ- and YZ-planes at different lifting speeds. The maximum tension is observed at a lifting speed of 1 m/s, reaching a total of 12.5kN in both the XZ- and YZ-planes, similar to the results at lifting speeds of 0.25 m/s and 0.5 m/s.

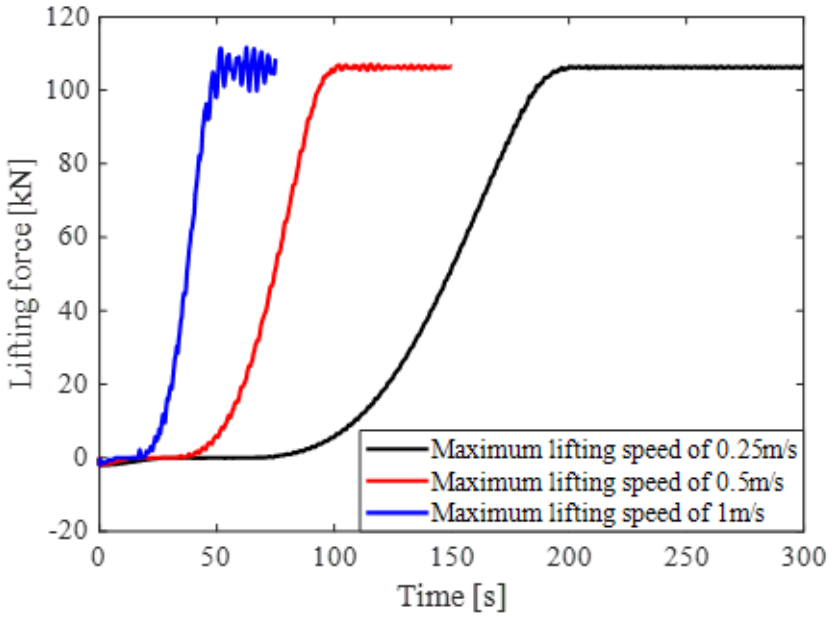

Figure 3.9: Comparison of the lifting forces for different lifting speeds of 0.25m/s, 0.5m/s, and 1m/s.

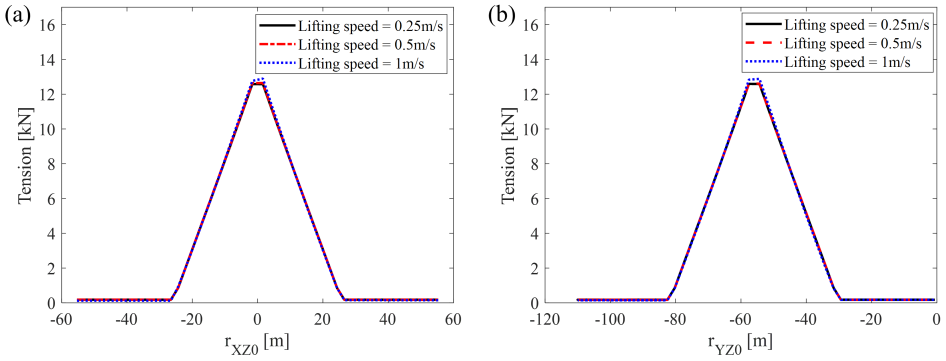

Figure 3.10: Comparisons of tensions in (a) XZ- and (b) YZ-planes at different lifting speeds of 0.25m/s, 0.5m/s and 1m/s.

3.3.4 Lifting operations of a damaged gravity-type fish cage

Figure 3.11 shows the illustration of the broken net rope in the bottom net for the damaged gravity-type fish cages, where the broken net rope of Damaged fish cage 1 is located at the center, while that of Damaged fish cage 8 is located at the edge next to side net. To simplify the analysis, the broken net ropes are aligned with the x-axis. The lifting speed for the present lifting operations is set to 0.5m/s with the time-step of 1ms. A total of 8 cases will be analysed in this section. Each case has one broken net rope, beginning with the net rope located in the center, corresponding to 'Damaged fish cage 1'. The last case analysed will be the 'Damaged fish cage 8', shown in Figure 3.11.

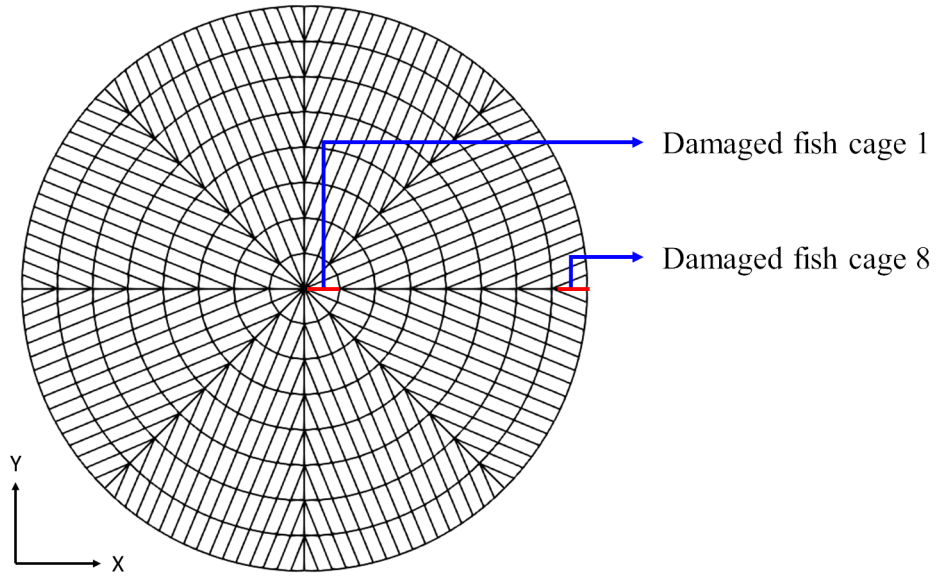

Figure 3.11: Illustration of the broken net rope in the bottom net for the damaged gravity-type fish cages, where the broken net rope of Damaged fish cage 1 is located at the center, while that of Damaged fish cage 8 is located at the edge next to side net.

Figure 3.12 shows the comparison of the lifting forces of the normal and damaged fish cage, with the maximum lifting speed of 0.5m/s and the time-step of 1ms. Similarly to the time-step sensitivity study, the lifting force is small in [0s, 50s] and quickly increases over a short duration of [50s, 100s]. It can be observed that the lifting forces for all eight cases of the damaged fish cage and the normal case are similar with each other. The maximum lifting force reaches up to 107kN.

Figures 3.13 and 14 show the comparisons of the maximum tensions in the XZ- and YZ-plane at 100s for the normal and damaged fish cages, respectively. It can be observed that the maximum tensions in both XZ- and YZ-planes remain almost the same, especially in YZ-plane. It can be attributed to the symmetry of the fish cage. In the XZ-planes it can be observed that the tension distribution between the normal cage and the damaged cages are different. The maximum tension in the XZ-plane can be found in Damaged cage 8 reaching up to 12.61kN, while for the maximum tension in YZ-plane it can be found in damaged cage 7

reaching up to 12.63kN.

It can be concluded that the lifting forces of the damaged nets will remain relatively stable in the cases with a single broken net rope. Consequently, the fish cage can sustain its operational functionality. However, if the net rope happens to break, it may cause tearing of the inner net as shown in Figure 3.11. Then the hole is large enough to cause a significant loss in fish, as they can easily escape.

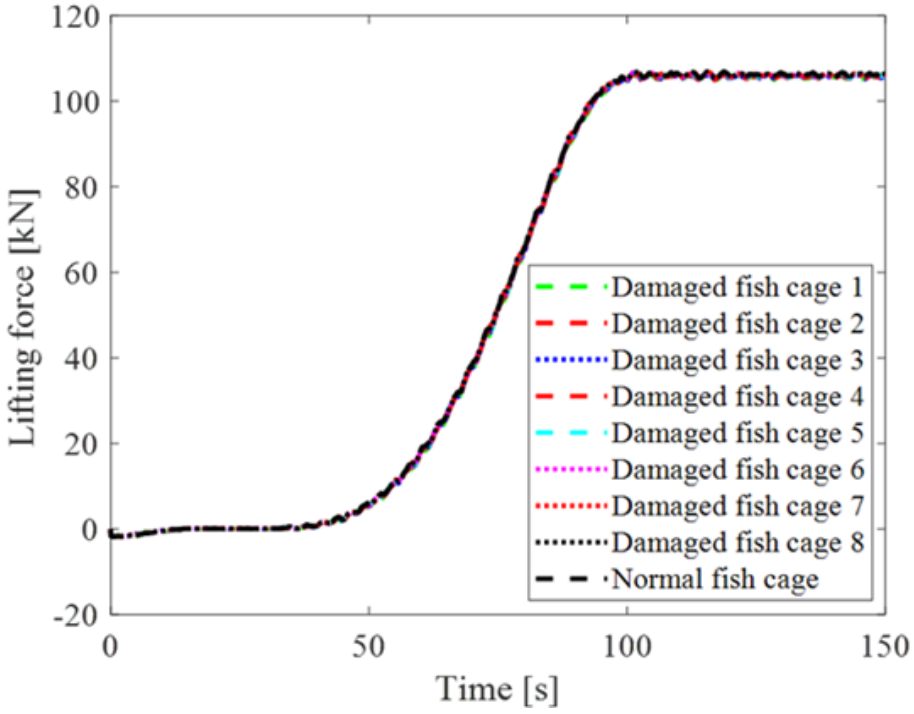

Figure 3.12: Comparison of the lifting forces in the normal- and damaged fish cages, with the maximum lifting speed of 0.5m/s and the time-step of 1ms.

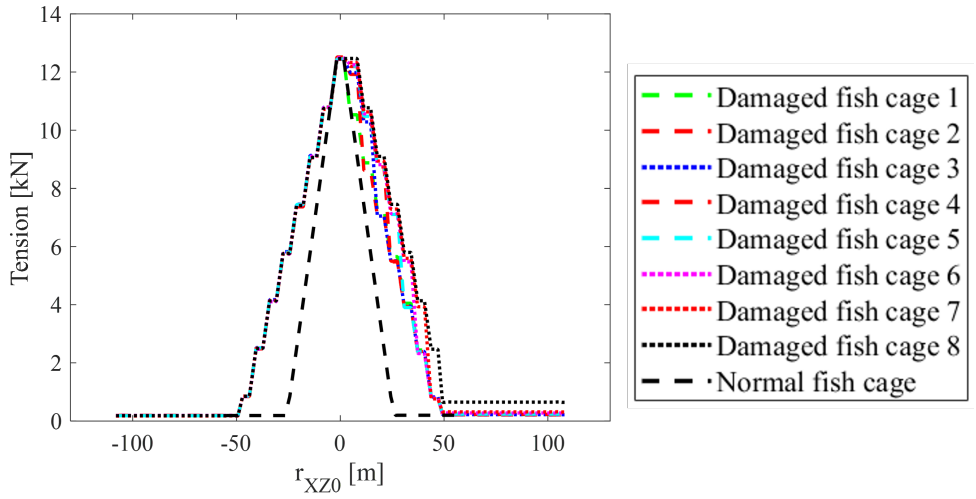

Figure 3.13: Comparison of the maximum tensions in the XZ-plane after at 100s for the normal and damaged fish cages, with a maximum lifting speed of 0.5m/s and the time-step of 1ms.

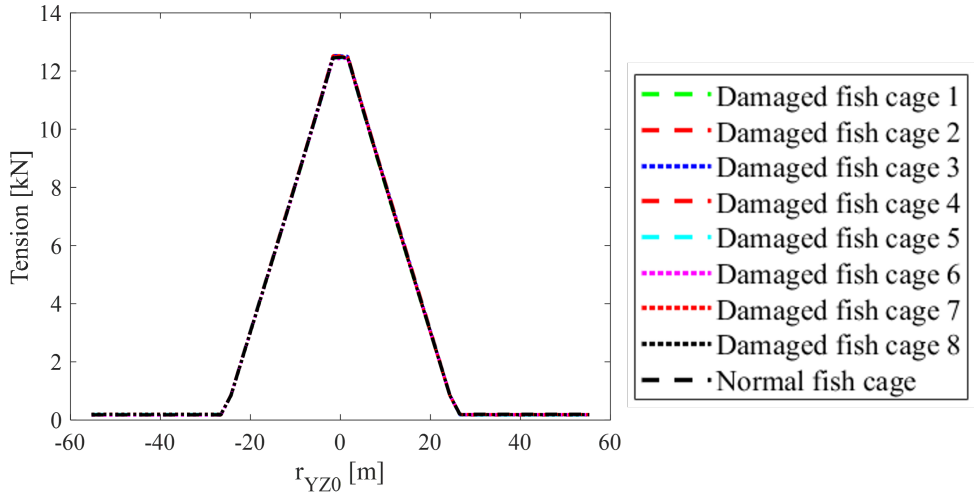

Figure 3.14: Comparison of maximum tensions in the YZ-plane after 100 seconds for the normal and damaged fish cages, with a maximum lifting speed of 0.5m/s and the time-step of 1ms.

Figure 3.15 shows the top views of the deformations and tensions of the bottom net of the normal fish cage and the damaged fish cage 1. It can be observed that the maximum tension is located at the center of the bottom nets and their tension distribution remains similar. The difference of the broke net rope can be found to the right side of the center lifting point in Figure 3.15(b).

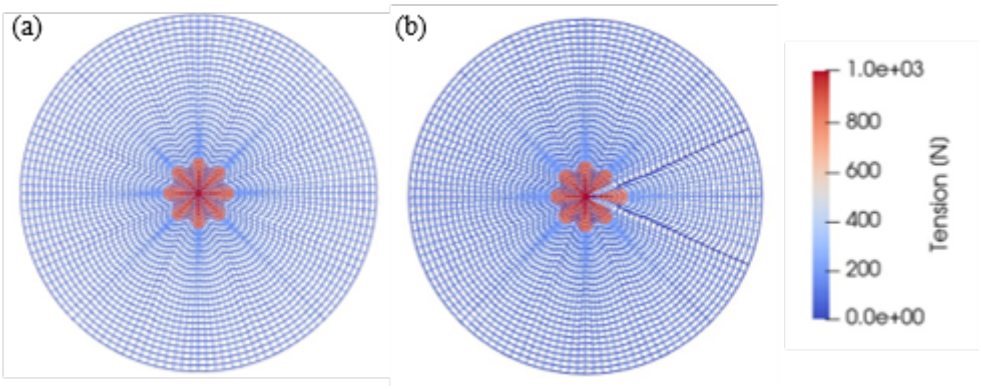

Figure 3.15: Top views of the deformations and tensions of the bottom nets of the normal fish cage (a) and Damaged fish cage 1 (b), with maximum lifting speed of 0.5m/s and the time-step of 1ms.

Figure 3.16 shows the comparisons of the tensions in XZ- and YZ-planes for Damaged fish cage 1 at different times during the lifting operation. The time instants shown in this figure are chosen as 50s, 75s, and 100s. As can be seen, the tension on the bottom net has a significant increase in [50s, 100s]. The tensions in the XZ-planes show uneven tension distributions, where the tension on the left side of the bottom net is larger than that on the right side of the bottom net. The reason for this is that the broken net rope results in the loss of connection between the center lifting point and the net rope and thus leads to less load. As a result, the tension in the XZ-plane will not remain symmetrical during the lifting operation. The tension in the YZ-planes remains uniform throughout the lifting operation. The reason for this can be attributed to the symmetry of the fish cage in this plane, since the effect of the broken net rope will not affect this area, as can be seen from the deformations and tensions of the fish cages in top view in Figure 3.15(b).

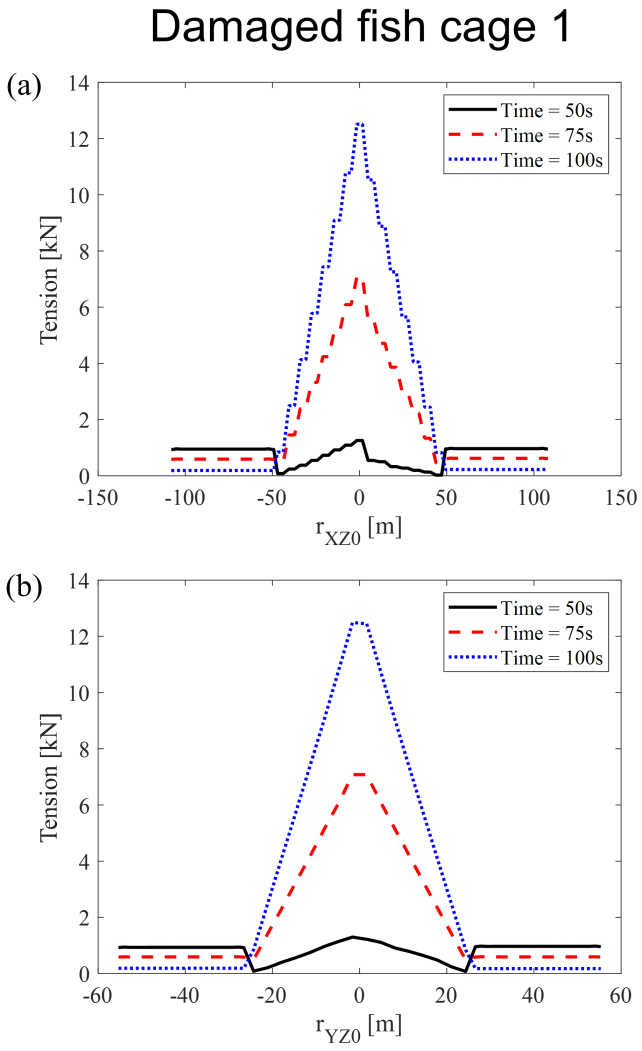

Figure 3.16: Comparisons of the tensions in XZ- (a) and YZ- plane (b) in Damaged fish cage 1 with a lifting speed of 0.5m/s and the time-step of 1ms.

Figures 3.17-3.19 shows the comparisons of tensions in the damaged fish cage 2-8 in XZ- and YZ- planes at different times. The times chosen are the same with that in Figure 3.16. It can be observed that as the broken net rope move from the center to the side net, the tension distribution in XZ- and YZ-planes are gradually become symmetrical. It can be concluded that the broken net rope does not have any significant effect on the overall tension in all these cases.

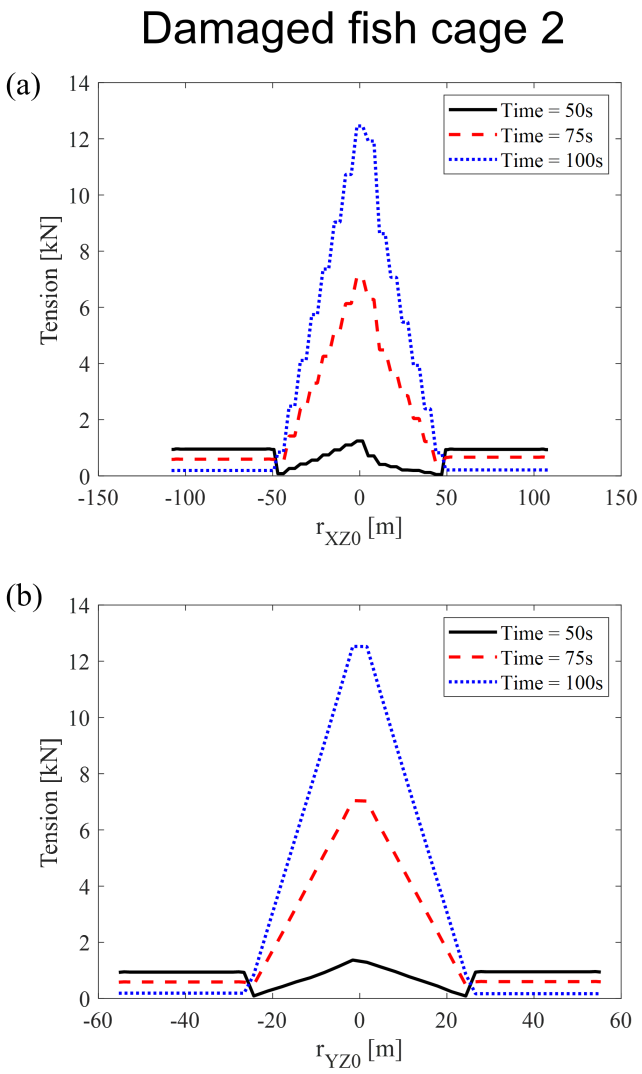

Figure 3.17: Comparisons of tensions in the Damaged fish cage 2-3 in (a) XZ- and (b) YZ- planes with a lifting speed of 0.5m/s and the time-step of 1ms.

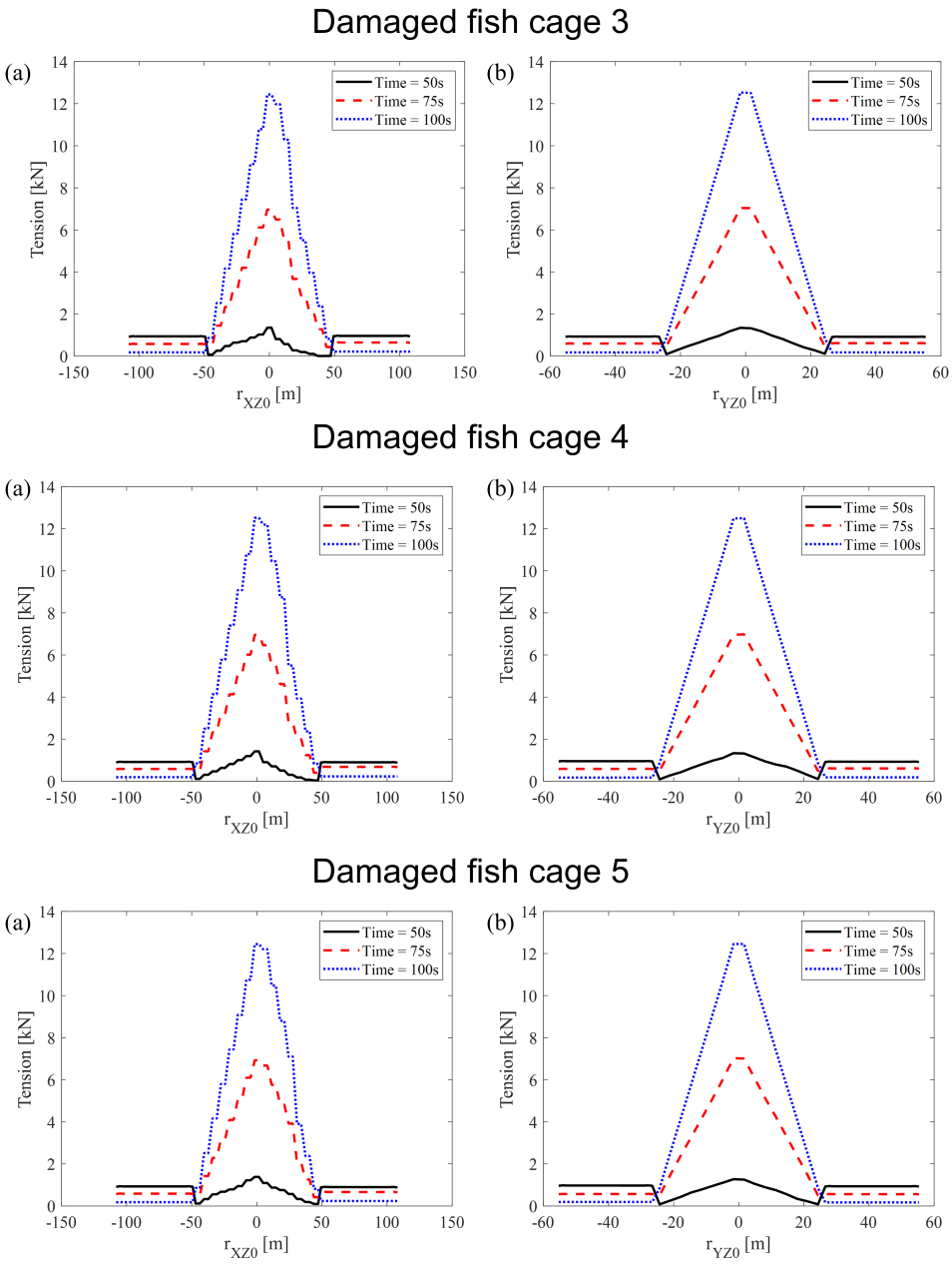

Figure 3.18: Comparisons of tensions in Damaged fish cage 4-5 in (a) XZ- and (b) YZ- planes with a lifting speed of 0.5m/s and the time-step of 1ms.

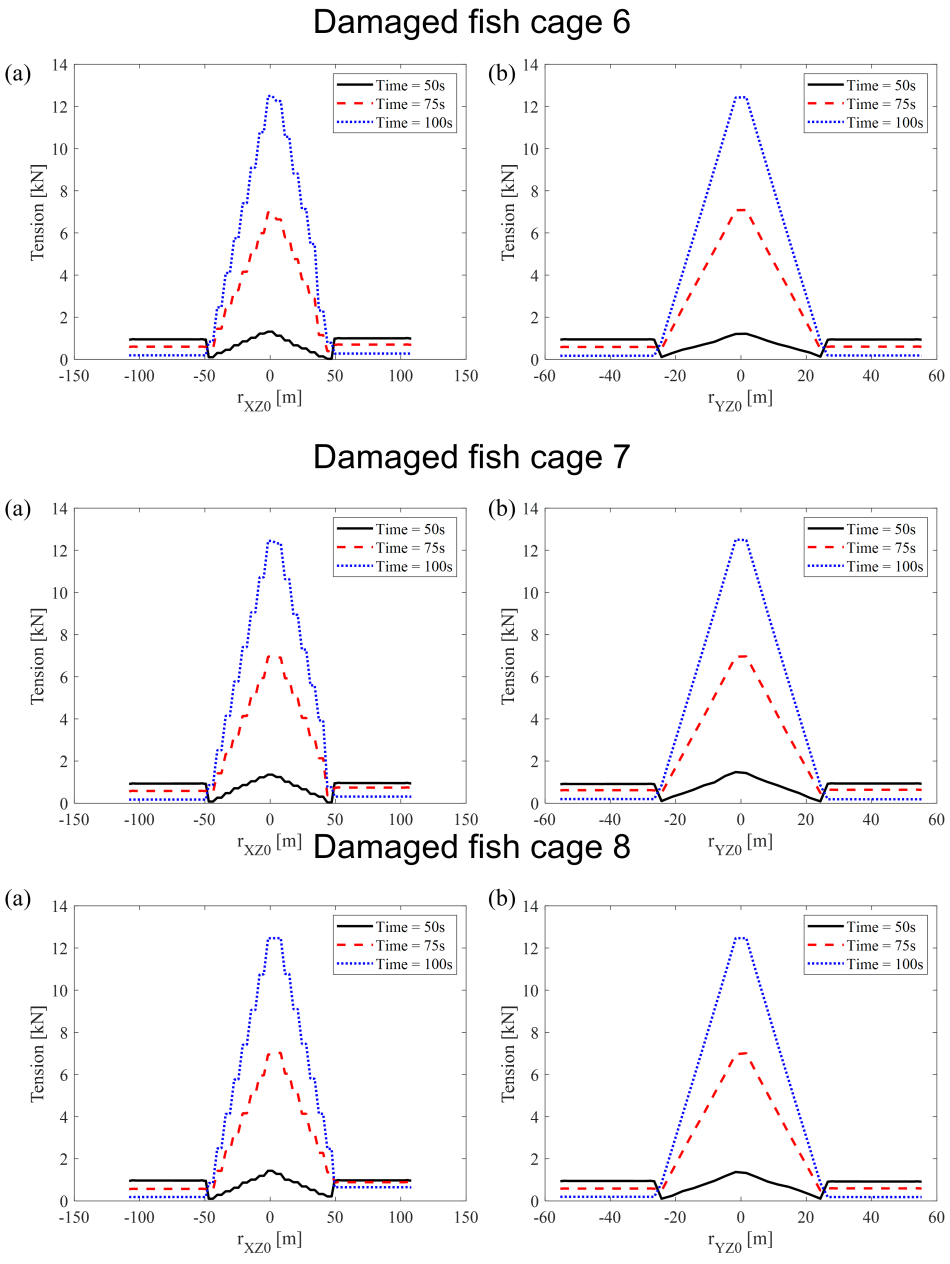

Figure 3.19: Comparisons of tensions in Damaged fish cage 6-8 in (a) XZ- and (b) YZ- planes with a lifting speed of 0.5m/s and the time-step of 1ms.

Figure 3.20 shows the top views of the deformations and tensions in the bottom net after the crane totally stops. It can be observed that the maximum tension is located at the center of the bottom net, and the differences between all these cases can be seen on the right side of the center. As mentioned earlier, it was concluded that the effect of the broken net ropes does not have a significant impact on the tension distribution of the net. The deformations of the bottom nets of the fish cages are slightly different between all these cases.

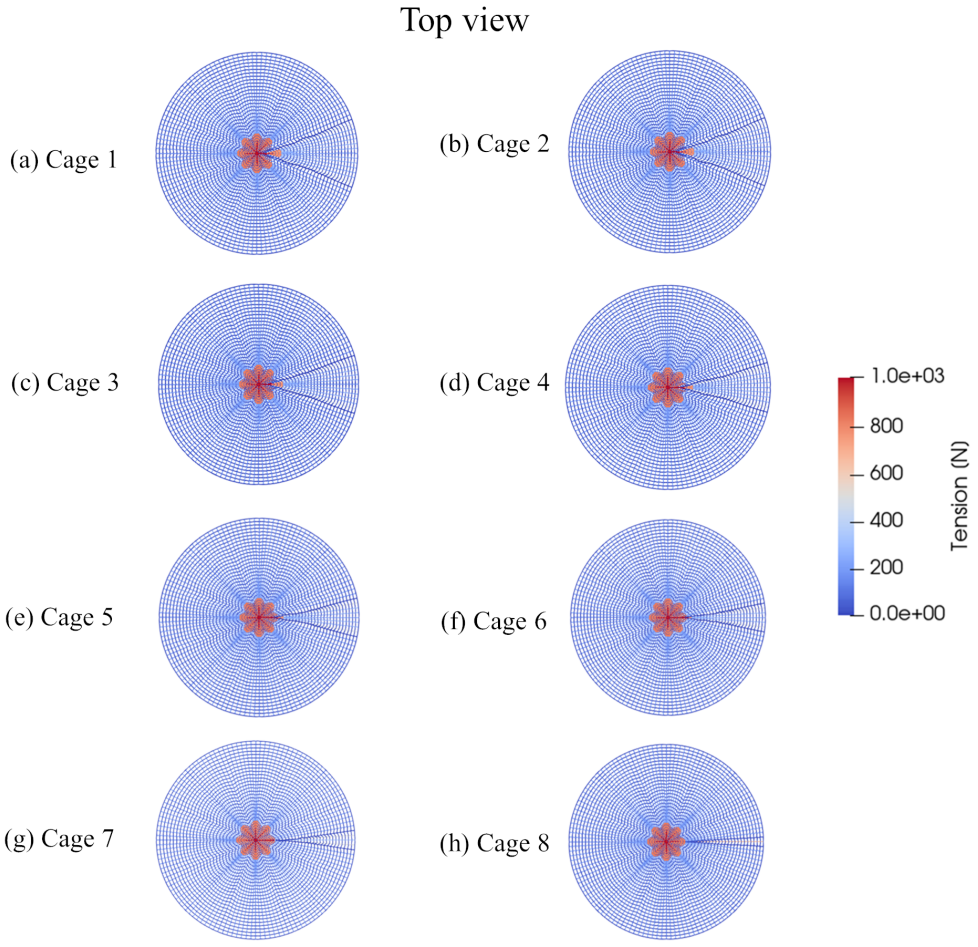

Figure 3.20: Top views of the deformations and tensions in the bottom net of the damaged fish cages, with a maximum lifting speed of 0.5m/s and the time-step of 1ms.

3.4 Conclusion

The dynamic behaviors of the lifting operations of a gravity-type fish cage under calm sea conditions are investigated in this study. The structural deformations of the aquaculture net are obtained using an improved XPBD method. Correction forces are applied to the aquaculture net to predict the accurate tensions. The present XPBD is validated against the experimental results of a flexible horizontal net. The time-step sensitivity study is conducted for the lifting operation of the fish cage. Results show that the lifting force increases rapidly resulting from the weight of the sinkers at the bottom of the side net. The maximum tension of the net is located at the net ropes connected to the center point of the bottom net. The lifting force and tension of the net do not have significant changes in damaged fish cages with broken net rope at the bottom net. The structure of the bottom net should be enhanced for safety lifting operations.

References

[1] A. J. Berstad et al. “Enhancement of design criteria for fish farm facilities including operations”. In: *Conference on Offshore Mechanics and Arctic Engineering* 41960 (2005), pp. 825–832.

[2] Malcolm Beveridge. *Cage Aquaculture. 3d Edition.* Jan. 2004. ISBN: 978-1-4051-0842-3.

[3] Cristian Cifuentes and M.H. Kim. “Numerical simulation of fish nets in currents using a Morison force model”. In: *Ocean Systems Engineering* 7 (June 2017), pp. 143–155. DOI: 10.12989/ose.2017.7.2.143.

[4] Rui Dou. *Numerical Modeling and Analysis of a Semi-submersible Fish-cage*. 2018. URL: https://ntnuopen.ntnu.no/ntnu-xmlui/handle/11250/2615064.

[5] Y.C. Guo, S.C. Mohapatra, and C. Guedes Soares. “Review of developments in porous membranes and net-type structures for breakwaters and fish cages”. In: *Ocean Engineering* 200 (2020), p. 107027. ISSN: 0029-8018. DOI: https://doi.org/10.1016/j.oceaneng.2020.107027. URL: https://www.sciencedirect.com/science/article/pii/S0029801820301025.

[6] John E. Huguenin. “The design, operations and economics of cage culture systems”. In: *Aquacultural Engineering* 16.3 (1997), pp. 167–203. ISSN: 0144-8609. DOI: https://doi.org/10.1016/S0144-8609(96)01018-7. URL: https://www.sciencedirect.com/science/article/pii/S0144860996010187.

[7] Chun-Woo Lee et al. “Physical modeling for underwater flexible systems dynamic simulation”. In: *Ocean Engineering* 32 (Mar. 2005), pp. 331–347. DOI: 10.1016/j.oceaneng.2004.08.007.

[8] M. Miles, M. Müller, and N. Chentanez. *XPBD: position-based simulation of compliant constrained dynamics. Proceedings of the 9th International Conference on Motion in Games.* 2007.

[9] Matthias Müller et al. “Position based dynamics”. In: *Journal of Visual Communication and Image Representation* 18.2 (2007), pp. 109–118. ISSN: 1047-3203. DOI: https://doi.org/10.1016/j.jvcir.2007.01.005. URL: https://www.sciencedirect.com/science/article/pii/S1047320307000065.

[10] Michael Sievers et al. “Submerged cage aquaculture of marine fish: A review of the biological challenges and opportunities”. In: *Reviews in Aquaculture* 14.1 (2022), pp. 106–119. DOI: https://doi.org/10.1111/raq.12587. URL: https://onlinelibrary.wiley.com/doi/abs/10.1111/raq.12587.

Chapter 4

Numerical study on the dynamic response of gravity-type fish cages in extreme conditions

Abstract

The dynamic responses of multiple fish cages with mooring lines under regular and irregular wave and current conditions are investigated in the present study. The structural deformations of the fish cages and mooring system are obtained using a modified XPBD algorithm, with correction forces to accurately predict tensions. The present modified XPBD algorithm is validated against the experimental results of a vertical net panel and a cage net. Grid and time-step sensitivity studies are conducted for the dynamic response of the single fish cage with a mooring system. Results show that the fish cage system experiences the maximum horizontal force, pitch angle of the floating collar and sinker tube, horizontal displacement, and vertical displacement when the flow angle is 0 degrees. The different modeling of regular and irregular waves does not result in significant changes for the maximum calculated values. However, the fish cage will experience an increased pitch angle under regular waves. The extension of the mooring lines to ensure the pretension is suggested to be 2%. For the multiple fish cage configuration, the mooring lines along the wave and current direction should be enhanced by increasing the mooring line numbers or diameter.

Keywords:

Aquaculture; gravity-type fish cage; extended position-based dynamics; regular wave and current conditions; irregular wave and current conditions; extreme conditions.

4.1 Introduction

Aquaculture, or fish farming, plays an important role in meeting the world's growing demand for seafood [5] [10]. Gravity-type fish cages are commonly used in aquaculture, particularly in Norway, to produce fish in natural water bodies such as fjords [1]. These cages are submerged in water and allow for the controlled cultivation of fish species while maintaining environmental sustainability.

One promising location renowned for its suitability for fish farming is Bjørnafjorden, a fjord located south of Bergen in Norway (see Figure 4.1). With its pure water quality and abundant space, Bjørnafjorden offers an ideal setting for aquaculture operations [2]. The fjord's nutrient-rich waters support the growth of various fish species, contributing to Norway's thriving aquaculture industry.

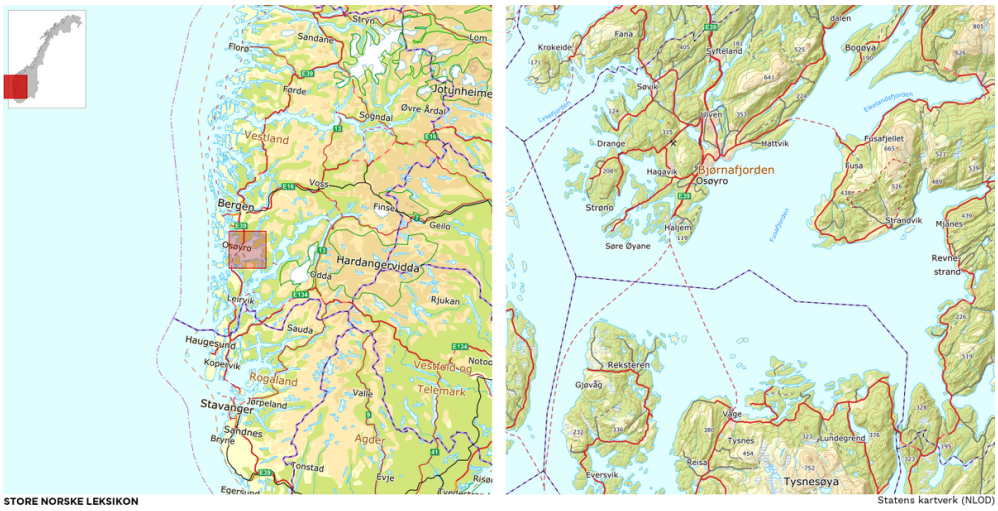

Figure 4.1: Location of Bjørnafjorden in Norway, picture by SNL.no [11].

Studying the effect of the mooring system is important because it ensures the stability and safety of fish cages in aquaculture operations. By anchoring the cages, the mooring system prevents drifting or displacement caused by waves and currents [12]. Understanding the behavior of the mooring system helps optimize its design and operation, ensuring the security of the fish cages and minimizing the risk of damage or loss [4].

Furthermore, multiple fish cages are essential for scaling up aquaculture production. By deploying several cages, farmers can cultivate a larger quantity of fish, thereby increasing their overall yield. Additionally, managing fish stocks becomes more efficient with multiple cages, facilitating tasks like sorting, feeding, and monitoring [6]. Spreading fish across several cages helps mitigate the risks of disease or environmental impacts affecting the entire population.

In present study, the hydrodynamics of fish farming using moored gravity-type cages in Bjørnafjorden are examined using the XPBD method. The unique characteristics of Bjørnafjorden, the design and functioning of gravity-type cages, and the challenges associated with aquaculture in this region are investigated.

4.2 Numerical model

4.2.1 Fish cage specifications

Figure 4.2 displays the full-scale structure of a single gravity-type fish cage with a mooring system. The fish cage design is the same as the one displayed in Chapter 3, section 3.2.1, and it consists of two main parts: a 30m high side net and a 5m high bottom net. The mooring system consists of three main parts: 80m long grid lines, 31.33m long bridle lines, and 188.68m long mooring lines. The specifications, including the dimensions and materials, of the gravity-type fish cage with a mooring system, are listed in Table 4.1.

Figure 4.3 displays six cases studied in Section 4.5. For simplicity, the cases are labeled according to the number of fish cages in the mesh in the x- and y-directions, respectively. The cases are labeled as (a) 1x1 fish cage, (b) 2x1 fish cages, (c) 2x2 fish cages, (d) 3x1 fish cages, (e) 3x2 fish cages, and (f) 4x2 fish cages (see Figure 4.3).

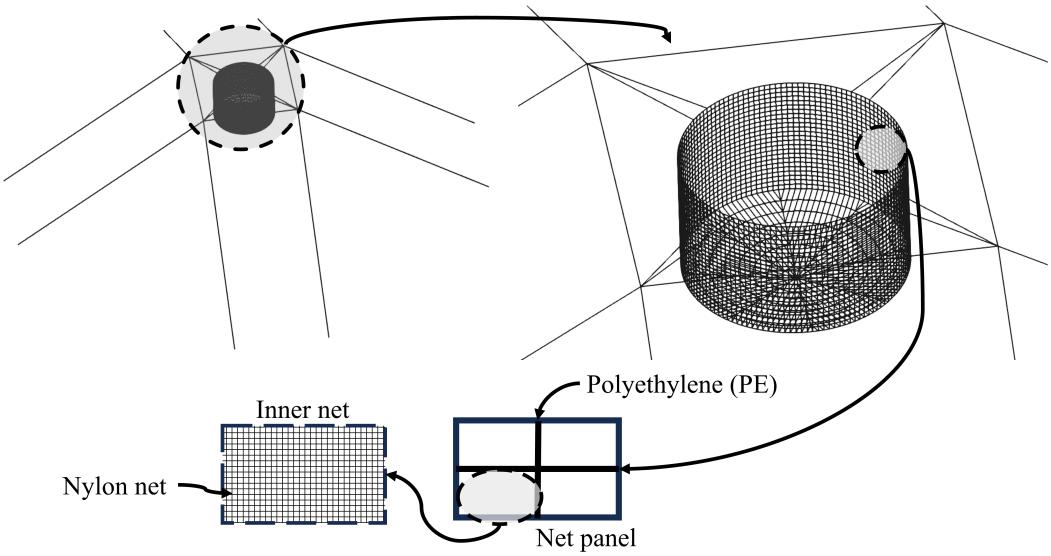

Figure 4.2: Illustration of the gravity-type fish cage with mooring systems and the net design.

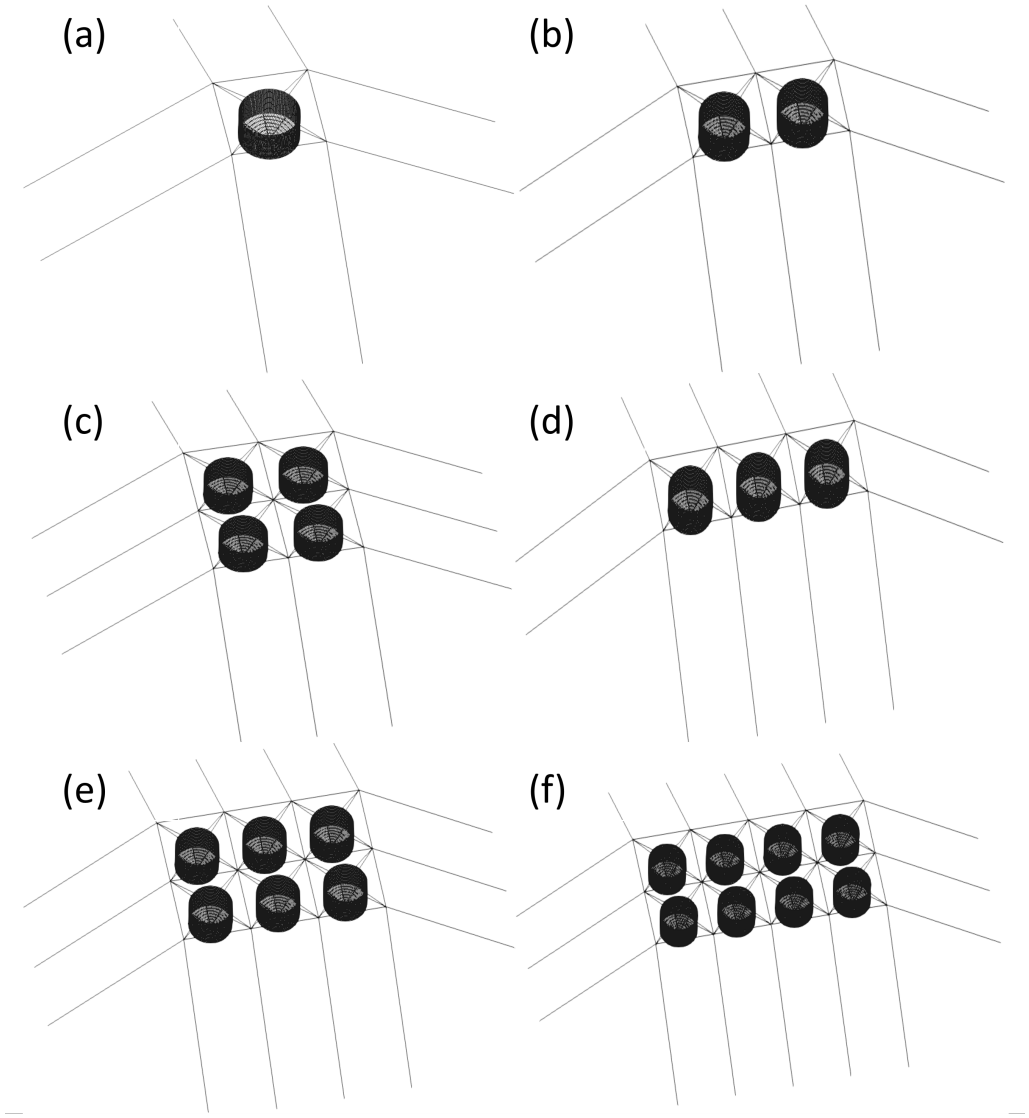

Figure 4.3: Illustration of gravity-type fish cages with mooring systems used in section 4.5, where (a) 1x1 fish cage to (f) 4x2 fish cage are studied.

Table 4.1: Specification of the gravity-type fish cage with mooring lines.

Parameters	Unit	Value
Cage circumference	m	160
Cage height	m	35
Side net height	m	30
Bottom net height	m	5
Side net sinkers' mass	kg/m	80
Bottom net sinkers' mass	kg	200
Density polyethylene	kg/m^3	960
Density nylon	kg/m^3	1140
Density concrete	kg/m^3	2500
Elastic modulus polyethylene	Pa	1.5 e9
Net rope diameter	mm	10
Inner twine diameter	mm	2.85
Length inner net	mm	25
Solidity (Sn)	-	0.2
Mooring line diameter	m	0.1
Grid line diameter	m	0.05
Bridle line diameter	m	0.05

Table 4.2: Specification of the current velocity profile for a 100-year round condition.

Depth [m]	Velocity [m/s]
0-5	1.2
15	0.8
25	0.5
50	0.45
100	0.25

4.2.2 XPBD Method

In the present study, extended position-based dynamics (XPBD) is employed to simulate the dynamic behavior of the fish cages. For a detailed explanation of the method, please refer to Section 3.2.2, as the currently implemented algorithm remains unchanged.

4.2.3 6-DOF Model

The 6-DOF model is adopted to calculate the motions of the sinker tube. The governing equations of the translational motions in the global coordinate system are given in Equation (4.1) based on Newton's Second Law.

$$\frac{d\nu_G}{dt} = m^{-1} \sum F_G \tag{4.1}$$

$$\frac{d\mathbf{x}_G}{dt} = \nu_G \tag{4.2}$$

Where $\mathbf{x}_{\text{CG}} = (x_{\text{CG}}, y_{\text{CG}}, z_{\text{CG}})$ is the location of the CoG of the sinker tube, m is the mass of the sinker tube. $\mathbf{F}_G$ is the vector of external forces applied to the CoG of the sinker tube. The angular velocity vector of the sinker tube in the body-fixed coordinate system is calculated using Equation (4.3) [9].

$$\frac{d\omega_{\mathbf{B}}}{dt} = \boldsymbol{I}^{-1} \left[\sum \boldsymbol{M_B} - \boldsymbol{\omega_B} \times (\boldsymbol{I}\boldsymbol{\omega_B}) \right] \tag{4.3}$$

Where $\mathbf{I}$ is the inertial tensor, $\mathbf{M}_B$ is the moment vector acting on the CoG of the sinker tube and $\boldsymbol{\omega}_B = (\omega_{B1}, \omega_{B2}, \omega_{B3})$ is the angular velocity vector. The subscript "B" means that the variables are in the body-fixed coordinate system. The rotational angles of the rigid body are computed using Equation (4.4) [9].

$$\begin{cases} \frac{d\phi}{dt} &= (\omega_{B2} sin\gamma + \omega_{B3} cos\gamma / cos\psi) \\ \frac{d\psi}{dt} &= (\omega_{B2} cos\gamma - \omega_{B3} sin\gamma) \\ \frac{d\gamma}{dt} &= (\omega_{B2} sin\gamma + \omega_{B3} cos\gamma) tan\psi \end{cases} \tag{4.4}$$

Where ϕ, ψ, and γ are the yaw, pitch, and roll angles, respectively. The global and body-fixed coordinate systems of the sinker tube are shown in Figure 4.4. The position of a point on the sinker tube in the global coordinate system can be obtained from its position in the body-fixed coordinate systems using Equation (4.5) based on the coordinate transformations of rotation axes.

$$\begin{bmatrix} x & - & x_{CG} \\ y & - & y_{CG} \\ z & - & z_{CG} \end{bmatrix} = \boldsymbol{R} \begin{bmatrix} X & - & X_{CG} \\ Y & - & Y_{CG} \\ Z & - & Z_{CG} \end{bmatrix} \tag{4.5}$$

where

$$\boldsymbol{R} = \begin{bmatrix} cos\phi & -sin\phi & 0 \\ sin\phi & cos\phi & 0 \\ 0 & 0 & 1 \end{bmatrix} \begin{bmatrix} cos\psi & 0 & sin\psi \\ 0 & 1 & 0 \\ -sin\psi & 0 & cos\psi \end{bmatrix} \begin{bmatrix} 1 & 0 & 0 \\ 0 & cos\gamma & -sin\gamma \\ 0 & sin\gamma & cos\gamma \end{bmatrix} \tag{4.6}$$

The velocities on the sinker tube are updated using Equation (4.7), where $\mathbf{x} = (x, y, z)$.

$$\nu = \nu_G + (\boldsymbol{R^{-1}\omega_B}) \times (\boldsymbol{x - x_G}) \tag{4.7}$$

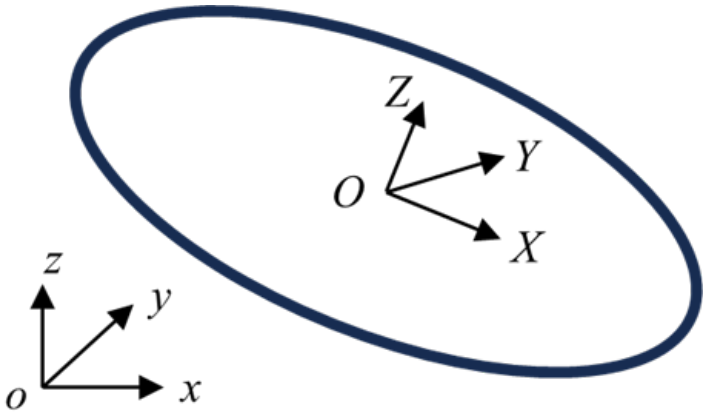

Figure 4.4: Illustration of the global and body-fixed coordinate systems of the sinker tube or floating collars.

4.2.4 Coupling between Modified XPBD and 6-DOF model

The coupling between the modified XPBD and 6-DOF is conducted as follows [13].

1. The modified XPBD provides the tensions of the brindles and the net ropes for the 6-DOF model.

2. The 6-DOF model is adopted to update the positions and speeds of the nodes located at the center lines of the sinker tube.

In this study, the modified XPBD and 6-DOF model share the same nodes at the center lines of the sinker tube. For the modified XPBD, the inverse masses of these nodes are set to zero, meaning that their positions and velocities are not updated by the modified XPBD. Instead, these motions are updated using the 6-DOF model, as described in Equations (4.5) – (4.7). For the 6-DOF model, the tensions of the brindles and the net ropes are provided by the modified XPBD.

4.2.5 Regular and irregular wave modeling

The regular and irregular waves are created by the combination of a series of linear Airy waves.

$$\eta = \eta_0 sinA \tag{4.8}$$

where $A = \omega t - x\cos\theta - y\sin\theta + \phi_0$, η_0 is the amplitude of the waves with a frequency of ω, θ is the wave direction, and ϕ_0 is the initial wave phase. The velocities of the fluid are given in Equations 4.9 - 4.11.

$$u_x = \omega B\eta_0 \times sinA \times cos\theta \tag{4.9}$$

$$u_y = \omega B\eta_0 \times sinA \times sin\theta \tag{4.10}$$

$$u_z = \omega B\eta_0 \times cosA \tag{4.11}$$

where $B = \cosh[k(z+H)]/\sinh(kH)$.

The wave amplitudes are calculated using Equation 4.12.

$$\eta_{0,i} = \sqrt{2\pi S(\omega_i)\Delta\omega} \tag{4.12}$$

where ω_i is the frequency of the group of waves. The chosen frequencies vary in a range of $[0.04$ rad/s$, 4$ rad/s$]$. $\Delta\omega$ is the difference between two successive frequencies. The initial wave phase $\phi_{0,i}$ for each group of waves is given as a random angle in a range of $[0, 360^\circ]$. $S(\omega)$ is the JONSWAP wave spectrum.

$$S(\omega) = 5.558 g^2 h_s^2 t_p^4 \omega^{-5} \exp\left(-1.25\lambda^{-4}\right)\left(1 - 0.287\ln\gamma\right)\gamma^b \tag{4.13}$$

where h_s is the significant height, t_p is the wave period at the peak value of S, $\lambda = \omega t_p/2\pi$, and $\gamma = 3.3$. b is given as follows.

$$b = \exp\left[-\frac{1}{2}\left(\frac{\lambda - 1}{\sigma}\right)^2\right] \tag{4.14}$$

$$\sigma = \begin{cases} 0.07, & \omega \leq 2\pi/t_p \\ 0.09, & \omega > 2\pi/t_p \end{cases} \tag{4.15}$$

The combination of the elevations and velocities has the following forms.

$$\eta = \sum_{i=1}^{N} \eta_i, \quad u_x = \sum_{i=1}^{N} u_{x,i}, \quad u_y = \sum_{i=1}^{N} u_{y,i}, \quad u_z = \sum_{i=1}^{N} u_{z,i} \tag{4.16}$$

4.2.6 Morison model

The Morison model has been applied to calculate the drag forces acting on the net ropes. In practical applications for fish netting, the environmental load on a line-like structure can be decomposed into two components: normal drag and tangential drag, expressed in equation 4.17.

$$F_n = \frac{1}{2} C_n \rho L d |U_n| U_n, \quad F_\tau = \pi \mu C_t L U_t \tag{4.17}$$

Where L and d denote the length and diameter of the line element, respectively. The coefficients $C_n$and C_t represent the normal and tangential drag coefficients, respectively, as determined from experimental results [3]. The coefficients are shown in Equation 4.19.

The normal and tangential velocities are expressed in Equation 4.18.

$$U_n = (U - v) - U_\tau, \quad U_\tau = [(U - v) \cdot \tau] \, \tau \tag{4.18}$$

Where U and v represent the velocities of the fluid and structure, respectively, while τ denotes the vector of the line element.

$$C_n = \begin{cases} 8\pi \left(1 - 0.87 s^{-2}\right) / s \mathrm{Re}_n, & 0 < \mathrm{Re}_n \leq 1 \\ 1.45 + 8.55 \mathrm{Re}_n^{-0.9}, & 1 < \mathrm{Re}_n \leq 30 \\ 1.1 + 4 \mathrm{Re}_n^{-0.5}, & 30 < \mathrm{Re}_n \leq 2.33 \times 10^5 \\ -3.41 \times 10^{-6} \left(\mathrm{Re}_n - 5.78 \times 10^5\right), & 2.33 \times 10^5 < \mathrm{Re}_n < 4.92 \times 10^5 \\ 0.401 \left(1 - e^{-(Re_n / 5.99 \times 10^5)}\right), & 4.92 \times 10^5 < \mathrm{Re}_n < 1 \times 10^7 \end{cases}$$

$$C_t = 0.55 \mathrm{Re}_n^{0.5} + 0.084 \mathrm{Re}_n^{2/3} \tag{4.19}$$

4.3 Validation and comparative assessment of the XPBD-method applicability

4.3.1 Validation study

The validation case is based on Lader et al. (2007) [7] experimental study on wave forces acting on a stationary vertical net structure, shown in Figure 4.5. The net has a width of 0.5m and a height of 1m, comprising 861 nodes and 2460 line elements. The half-mesh length is 25mm, and the twine diameter is 3.6mm, resulting in a solidity of 0.288. During the experiment, the top and bottom sections of the net were fixed. The net is subjected to regular waves in freshwater. The specifications of the net design and the studied wave cases are listed in Table 4.3 and Table 4.4, respectively. Figures 4.6-4.8 present the experimental and numerical results of the horizontal force acting on the vertical net. The results show remarkable agreement, indicating that the Morison model is viable for further simulation of the flexible fish cage in wave conditions.

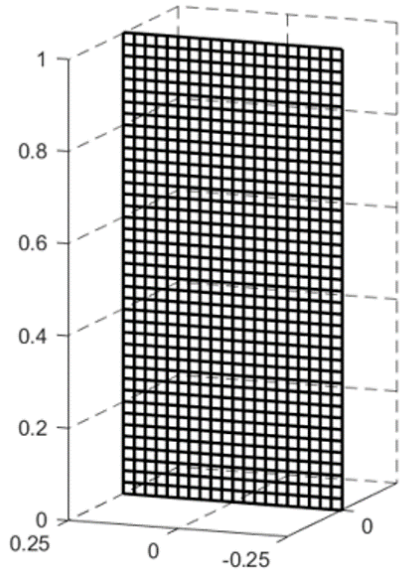

Figure 4.5: Illustration of the vertical net panel of the net used in the experiment (front view).

Table 4.3: Validation case specifications.

Parameters	Values
Net dimensions (meshes)	40x20
Node number	861
Element number	2460
Solidity	0.288
Twine diameter	3.6 mm
Bar length	25 mm

Table 4.4: Wave case specifications.

Wave case	3	4	5
Wave frequency	1.42 Hz	1.00 Hz	1.25 Hz
Wavelength	0.77 m	1.54 m	0.77 m
Wave period	0.7 s	1.00 s	0.8 s
Wave height	8.4 cm	16.5 cm	10.4cm

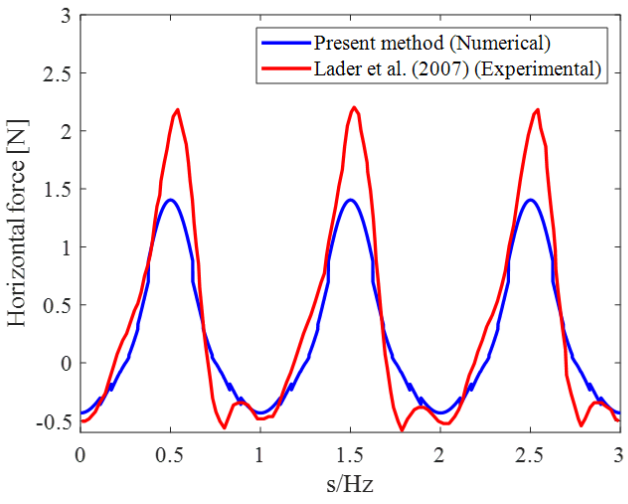

Figure 4.6: Comparison between the experiment results of Lader et al. [7] (Wave case 3) and the numerical results of the Morison model.

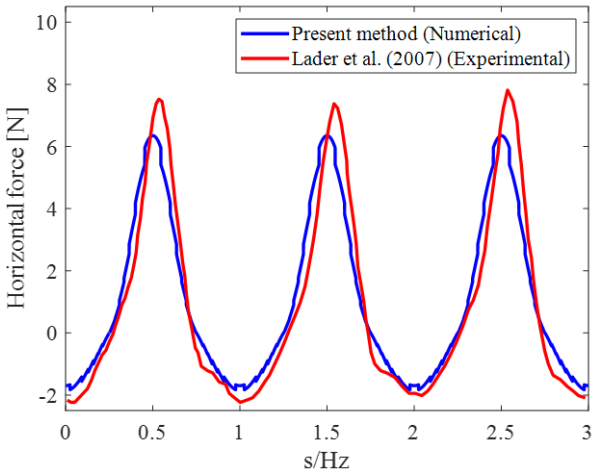

Figure 4.7: Comparison between the experiment results of Lader et al. [7] (Wave case 4) and the numerical results of the present Morison model.

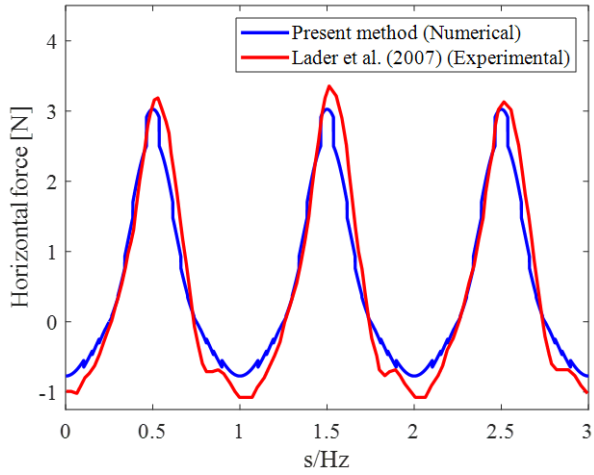

Figure 4.8: Comparison between the experiment results of Lader et al. [7] (Wave case 5) and the numerical results of the present Morison model.

4.3.2 Comparison study

Figure 4.9 and Figure 4.10 show the time-step sensitivity study of (a) the drag force and (b) the lift force acting on a fish cage in a current flow, using N19 and N35 net, respectively. This analysis considers three time steps: 0.1ms, 0.25ms, and 0.5ms. The results of the tested time steps exhibit strong agreement. To minimize computational costs for further calculations, a time step of 0.5ms is selected as the preferred option for the present study. Specifications of the comparison cases are listed in Table 4.5.

Table 4.5: Specifications of the comparison cases.

Net model	N19	N35
Diameter of net cage [m]	1.75	
Height of net cage [m]	1.5	
Young's Modulus Polyethylene [Pa]	40e6	
Density Nylon [kg/m^3]	1140	
Density water [kg/m^3]	1000	
Sinker's mass [kg]	0.6	
Half mesh [mm]	25.5	8.3
Twine diameter [mm]	2.42	1.41
Solidity	0.194	0.347

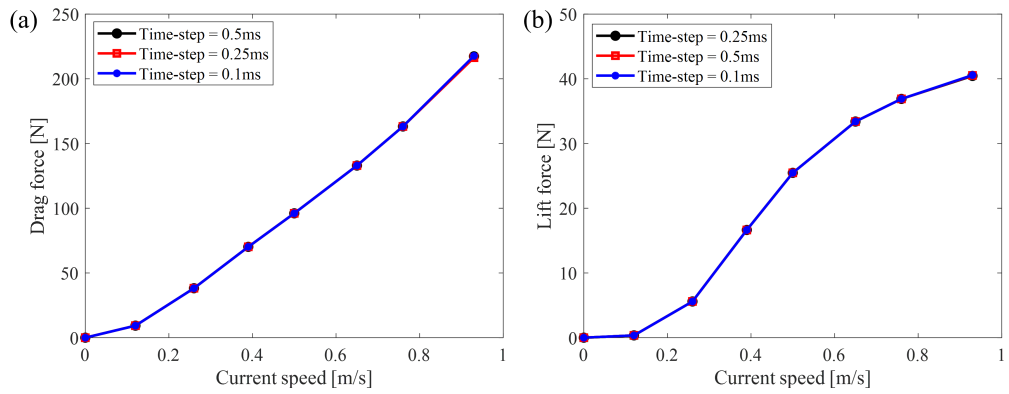

Figure 4.9: Comparison of the time-step sensitivity study of (a) the drag force and (b) the lift force acting on a fish cage in a current flow, using N19 net.

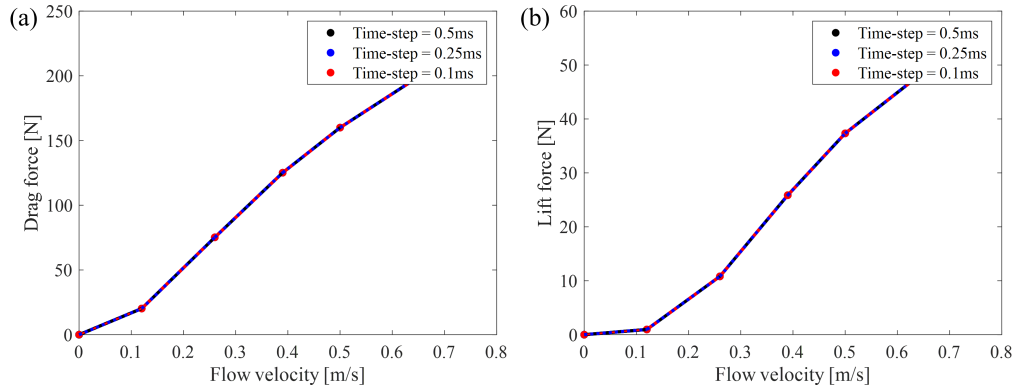

Figure 4.10: Comparison of the time-step sensitivity study of (a) the drag force and (b) the lift force acting on a fish cage in a current flow, using N35 net.

Figure 4.11 illustrates the net model configurations for the bottomless fish cage. Three fish cage mesh models, sized 16x5 (a), 32x9 (b), and 64x18 (c), are analyzed, considering the net dimensions (meshes) of the circumferential and vertical directions of the net panels. These net dimensions are listed in Table 4.6. For simplicity in this study, the fish cage mesh models are named coarse mesh, normal mesh, and fine mesh, as shown in Figure 4.11. Additionally, the fish cage nets N19 and N35 used by Moe-Føre et al. [8] are examined and compared in this

study, considering different current velocities ranging from 0.12m/s to 0.76m/s.

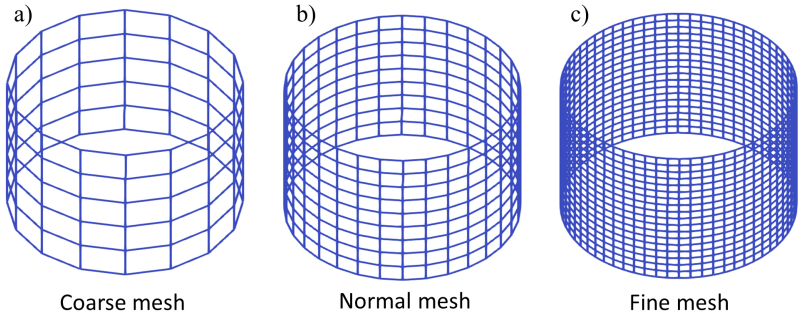

Figure 4.11: Illustration of the net model configurations for the bottomless fish cage, showcasing mesh net-panel size of (a) coarse mesh, (b) normal mesh, and (c) fine mesh, with consideration given to the circumferential and vertical numbers of net panels.

Table 4.6: Specification of mesh model configurations.

Net configuration	Number of horizontal net panels	Number of vertical net panels
Coarse mesh	16	5
Normal mesh	32	9
Fine mesh	64	18

Table 4.7 presents a comparison of the calculated drag forces on the N19 and N35 net models between the experimental and numerical results by Moe-Føre et al. (2016) [8] and the values calculated using the XPBD algorithm for different flow velocities. For N19, the calculated drag force values using the XPBD method increase from 9.3N at 0.12m/s to 163.2N at 0.76m/s. Similarly, for N35, the calculated drag force values increase from 12.5N at 0.12m/s to 201.6N at 0.76m/s. Table 4.8 compares the calculated lift force values on the N19 and N35 net models using the fine mesh configuration. For N19, the calculated lift force values using the XPBD method start at 0.35N at a flow velocity of 0.12m/s and increase to 36.6N at 0.76m/s. For N35, the lift force ranges from 0.67N to 38.6N at flow velocities of 0.12m/s and 0.76m/s, respectively.

Table 4.7: Comparison of the calculated values of drag force between the experiment conducted by Moe-Føre et al. (2016) [8] and the numerical simulation based on the XPBD method with the fine mesh configuration.

Values for drag force							
Flow velocity [m/s]		0.12	0.26	0.39	0.5	0.65	0.76
Moe-Føre et al. Experiment	N19	8.7 N	36.0 N	70.7 N	105.4 N	136.4 N	152.4 N
	N35	18.0 N	58.3 N	104.1 N	146.3 N	171.1 N	181.0 N
More-Føre et al. Numerical	N19	10.5 N	37.0 N	69.1 N	92.0 N	122.8 N	151.2 N
	N35	13.0 N	53.1 N	92.6 N	119.8 N	164.2 N	206.8 N
XPBD Method Numerical	N19	9.3 N	38.2 N	70.2 N	96.1 N	133.0 N	163.2 N
	N35	12.5 N	48.3 N	83.7 N	114.0 N	161.2 N	201.6 N

Table 4.8: Comparison of the calculated values of Lift force between the experiment conducted by Moe-Føre et al. (2016) [8] and the numerical simulation based on the XPBD method with the fine mesh configuration.

Values for lift force							
Flow velocity [m/s]		0.12	0.26	0.39	0.5	0.65	0.76
Moe-Føre et al. Experiment	N19	0.1 N	4.6 N	14.2 N	26.1 N	39.5 N	47.6 N
	N35	1.9 N	12.7 N	28.4 N	40.0 N	64.5 N	72.1 N
More-Føre et al. Numerical	N19	0.39 N	5.03 N	17.9 N	27.9 N	37.6 N	41.2 N
	N35	0.4 N	10.8 N	27.5 N	36.0 N	43.8 N	47.2 N
XPBD Method Numerical	N19	0.35 N	5.6 N	16.6 N	25.5 N	33.4 N	36.9 N
	N35	0.67 N	9.3 N	22.2 N	30.0 N	36.1 N	38.6 N

Figure 4.12 shows the comparisons of the drag forces for the N19 net model (a) and N35 net models (b), with the mesh configurations of coarse mesh, normal mesh, and fine mesh. It can be observed that the drag force and the lift force remain consistent across the different mesh configurations of the fish cage for flow velocities ranging from 0.12m/s to 0.76m/s.

Figure 4.13 shows the comparisons of the lift force for (a) N19 and (b) N35 net models, with the mesh configuration of coarse mesh, normal mesh, and fine

mesh. It can be observed that there is a more noticeable difference in the lift force of the coarse mesh netting configuration compared to the normal mesh and fine mesh netting. This difference can be explained by the scaling factor for the coarse mesh (1:4 scaling to fine mesh, 1:2 scaling to normal mesh), where the horizontal net panels are rounded up to 5 net panels in the vertical direction (supposed to be 4.5 net panels). The lift force can also be observed to be larger in the N35 net model.

It can be concluded that the drag force is larger in the N35 mesh model compared to N19 because the drag force and lift force depend on the solidity of the fish cage net and the flow velocity.

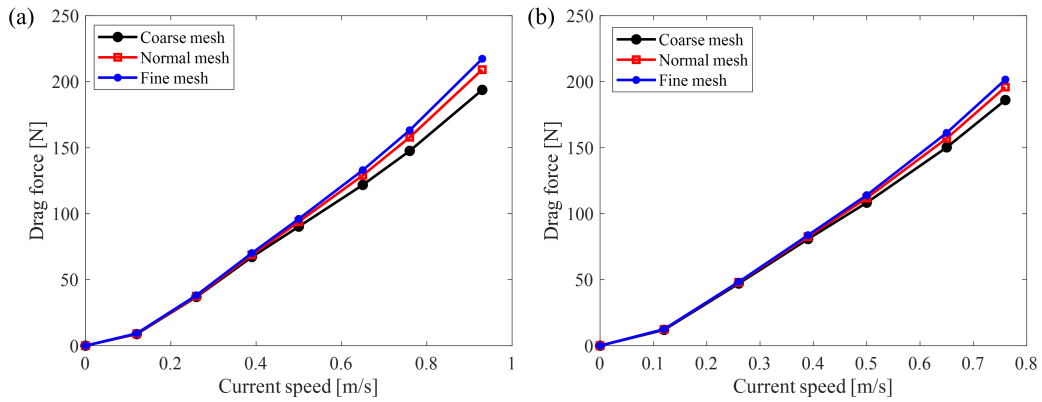

Figure 4.12: Comparison of drag force in (a) net model N19 and (b) net model N35 with coarse mesh, normal mesh, and fine mesh setup.

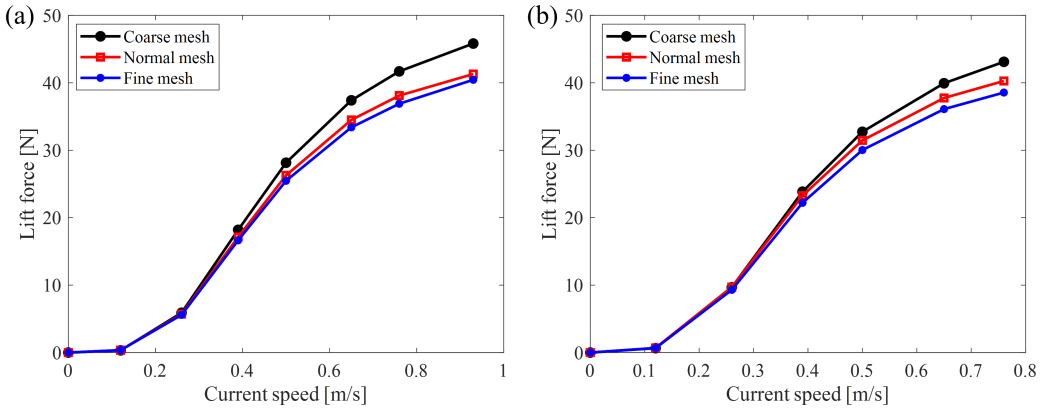

Figure 4.13: Comparison of lift force in (a) net model N19 and (b) net model N35 with coarse mesh, normal mesh, and fine mesh setup.

Figure 4.14 illustrates a comparison of deformations among the physical model, finite element model, and the present method using the N35 net model (fine mesh) utilized in the experiment by Moe-Føre et al. (2016) [8], at current velocities of 0m/s, 0.12m/s, 0.26m/s, 0.5m/s, and 0.76m/s. It can be observed that the deformations simulated by the present method exhibit remarkable alignment with the results of the simulation done with the finite element method.

Figure 4.15 shows a comparison of the deformation of the N19 and N35 net models using the present method. The current velocities range from 0.12m/s to 0.76m/s. It can be observed that the deformation of the net is larger in the N35 net compared to the N19 net, which is consistent with the findings presented in Table 4.7 and Table 4.8. This can be explained by the solidity of the net, which is larger in the N35 net compared to the N19 net.

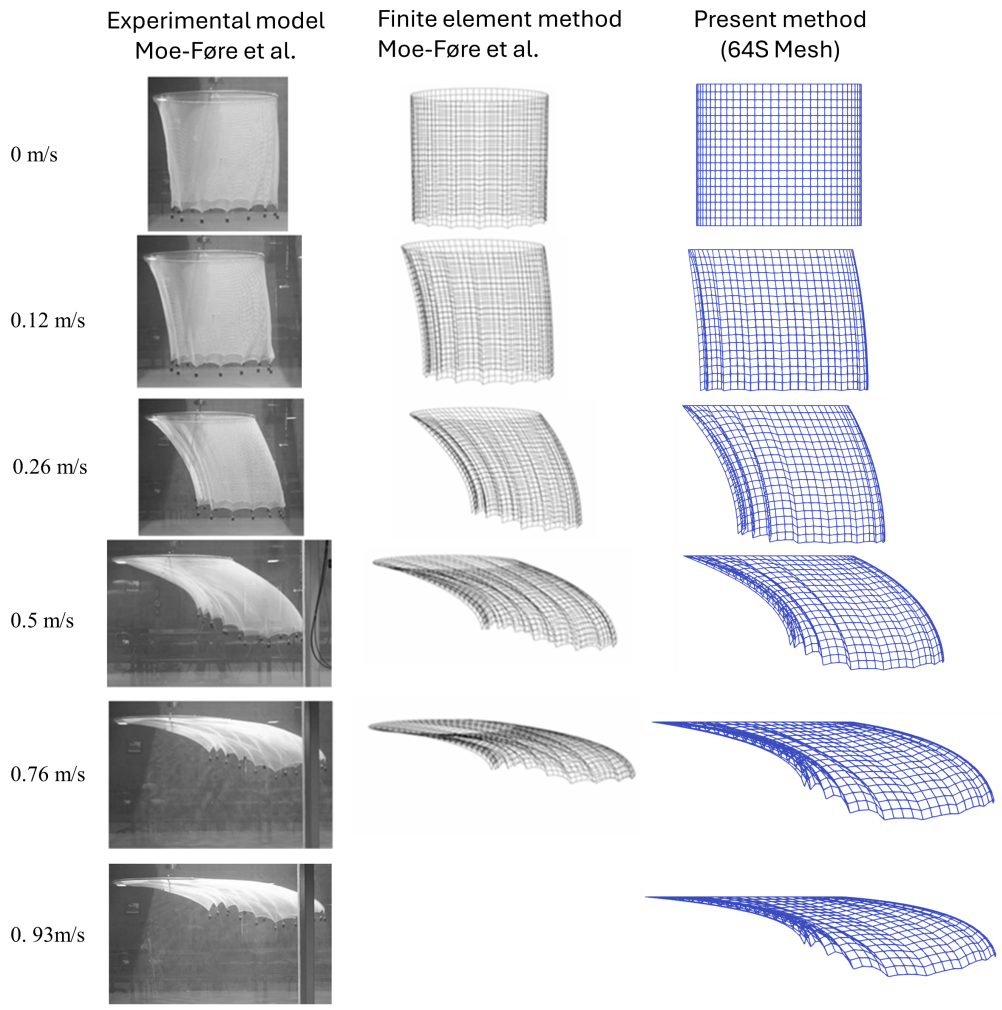

Figure 4.14: Comparison of deformation of N35 net between the experimental model [8], finite element model, and present model (fine mesh), in flow velocity of 0.12m/s, 0.26m/s, 0.5m/s, and 0.76m/s, in XZ-plane (Side view).

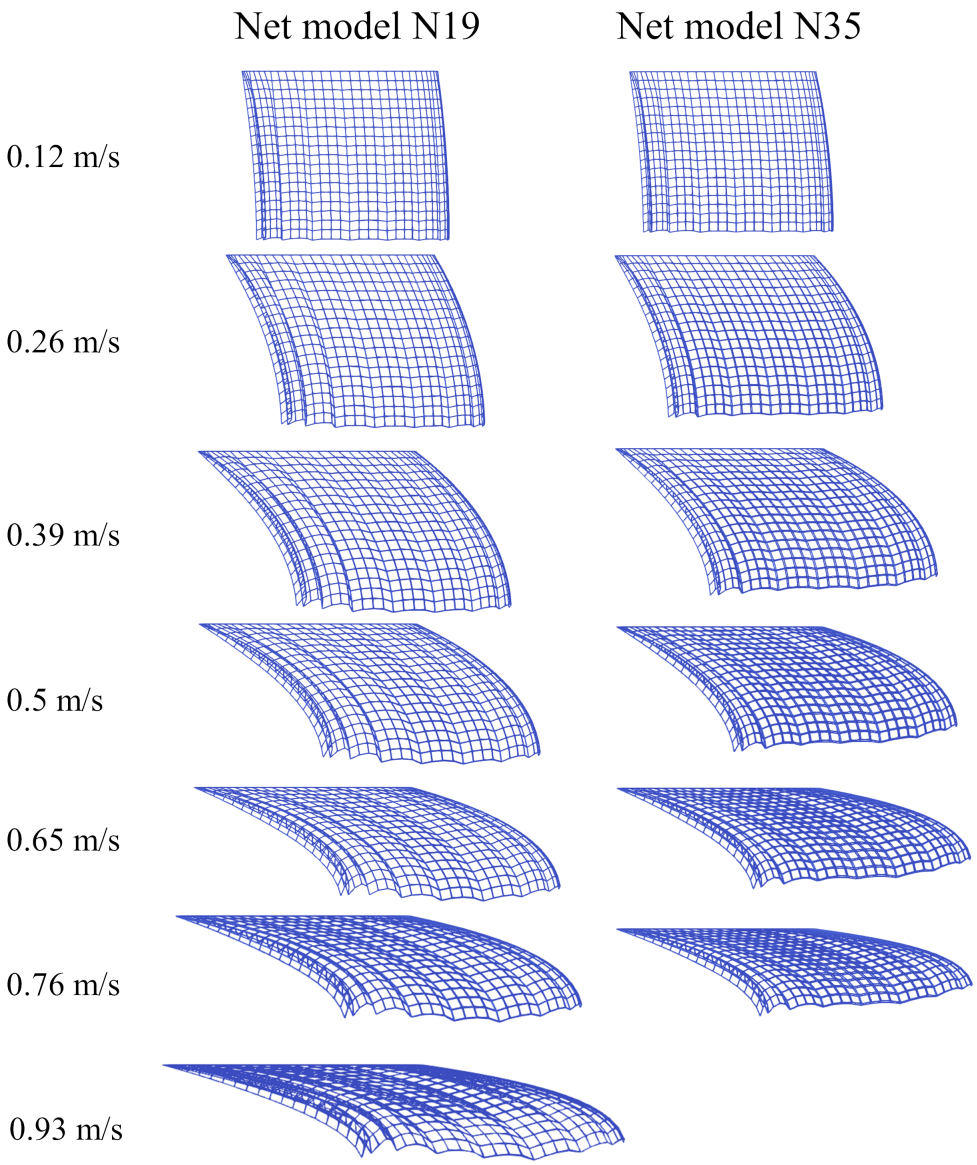

Figure 4.15: Comparison of the deformation of N19 and N35 net model using the present method, in flow velocity of 0.12m/s, 0.26m/s, 0.39m/s 0.5m/s, 0.65m/s, 0.76m/s, and 0.93m/s, in XZ-plane (Side view).

Figures 4.16 and Figure 4.17 present a comparative analysis of drag and lift forces, respectively, for the N19 net model (a) and N35 net model (b), both utilizing the fine mesh net mesh configuration. The figures compare the measured values and the calculated numerical values of the experiment with those obtained through the present method. Remarkably, the drag and lift forces show excellent agreement between the numerical methods. The largest drag force reaches 163.2N at a current velocity of 0.76m/s for N19 (present method) and 206.8N at 0.76m/s for N35 (Moe-Føre et al. (2016) [8] numerical). Similarly, the largest lift force reaches 47.6N in the N19 net model and 72.1N for the N35 net model at a current velocity of 0.76m/s (Moe-Føre et al. (2016) [8] Experiment).

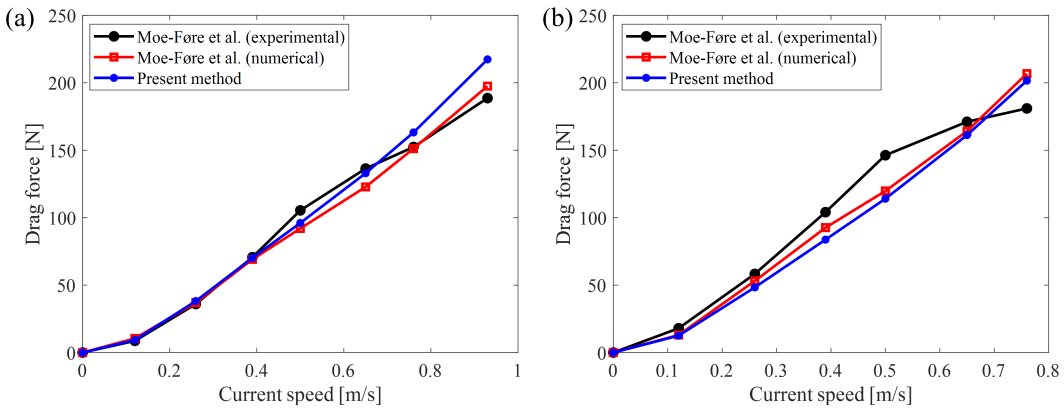

Figure 4.16: Comparison of drag force between the measured and numerical values of the experiment and the numerical values from the present method in (a) N19 net model and (b) N35 net model, with fine mesh configuration.

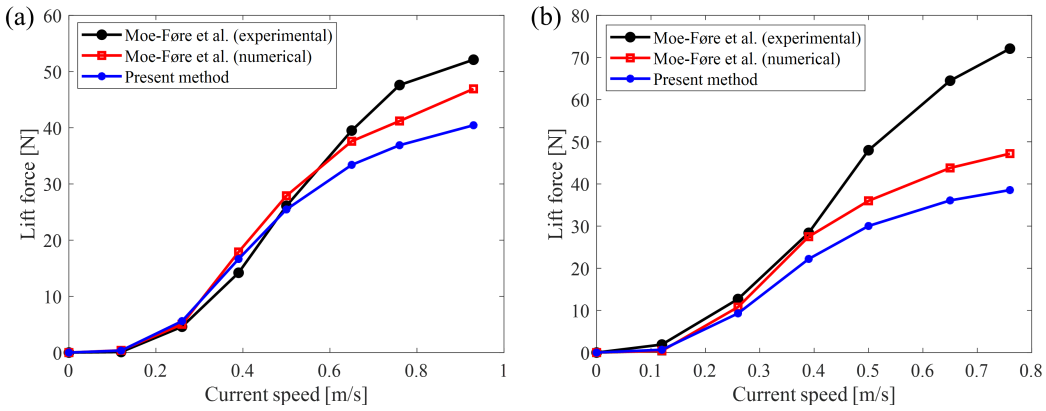

Figure 4.17: Comparison of lift force between the measured and numerical values of the experiment and the numerical values present method in (a) N19 net model and (b) N35 net model, with fine mesh configuration.

4.4 Hydrodynamic behavior of gravity-type fish cage with mooring system in extreme wave and current conditions

4.4.1 Time-step and grid sensitivity study of the fish cage with mooring system

The initial position of the fish cage is calculated using the XPBD algorithm, consistent with the one employed in Chapter 3.2.2. The present sensitivity study is conducted on a single gravity-type fish cage in regular waves. The following wave and current conditions are; wave period $T_{wave} = 6.6$s and wave height $H_{wave} = 2.8$m. The mooring lines are pre-tensioned with an extension of 2%, flow direction is 0 degree.

Figure 4.18 shows the time-step sensitivity study of the horizontal force acting on a single fish cage with a mooring system, utilizing the normal mesh. Three different time steps of 0.25 ms, 0.5 ms, and 1.0 ms are applied and examined. The results of time steps 0.25 ms and 0.5 ms show good alignment. However, the

time step of 1.0 ms can be considered too large to accurately calculate the force acting on the structure.

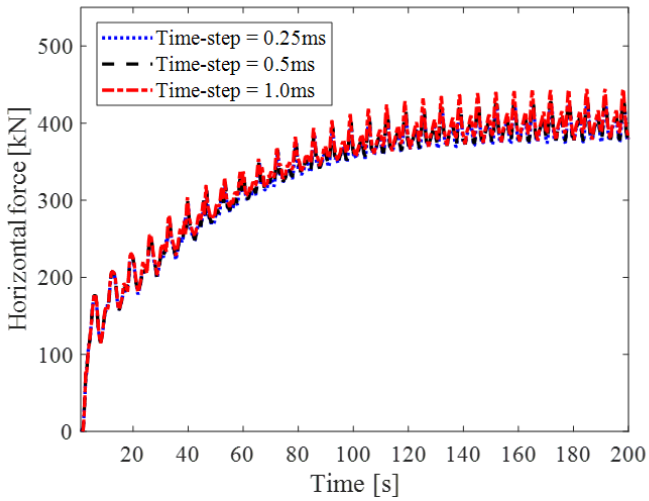

Figure 4.18: Time-step sensitivity study of the horizontal force acting on a single fish cage with mooring system, utilizing the normal mesh.

Figure 4.19 shows the time-step sensitivity study of the pitch angles of (a) the floating collar and (b) the sinker tube. Figure 4.20 shows the time-step sensitivity study of the horizontal displacements of the center of gravity (CoG) of (a) the floating collar and (b) the sinker tube. Figure 4.21 shows the time-step sensitivity study of the vertical displacements of the center of gravity (CoG) of (a) the floating collar and (b) the sinker tube.

The results from all tested time steps show remarkable agreement between 0.25 ms and 0.5 ms. However, the time step of 1.0 ms is considered too large in some of the studied cases. This can be observed in the sensitivity study of the pitch angles for both the floating collar and the sinker tube (see Figure 4.19), and it is more noticeable for the vertical displacements of the floating collar and sinker tube (see Figure 4.21). Consequently, the time step of 0.5 ms is chosen for further study.

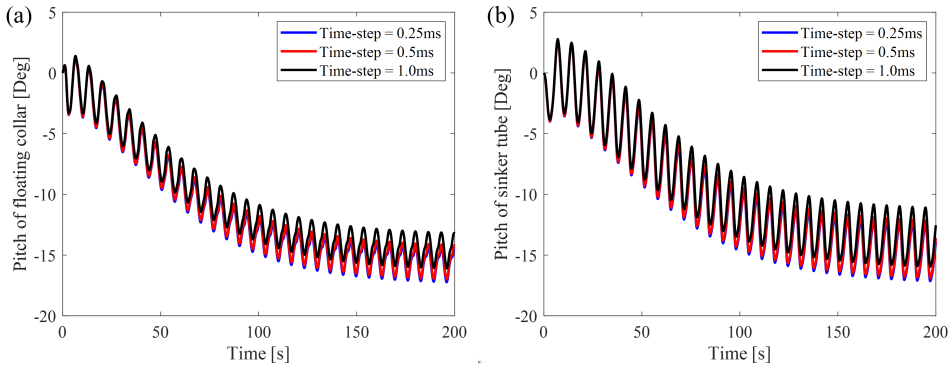

Figure 4.19: Time-step sensitivity study of the pitch angle of (a) the floating collar and (b) the sinker tube.

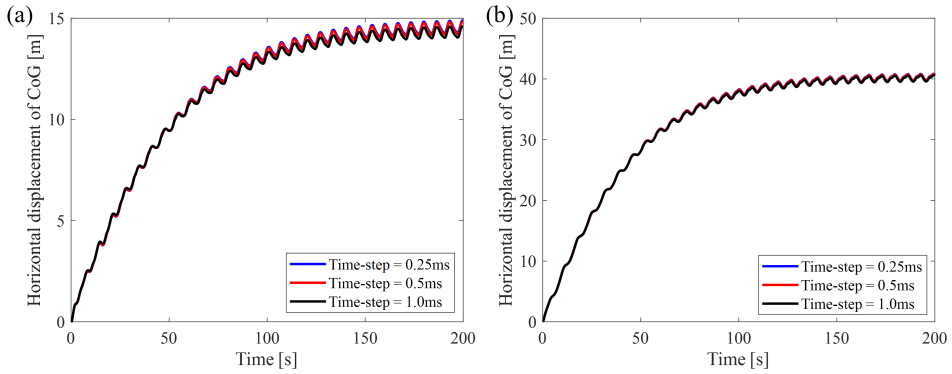

Figure 4.20: Time-step sensitivity study of the horizontal displacement of the center of gravity (CoG) of (a) the floating collar and (b) the sinker tube.

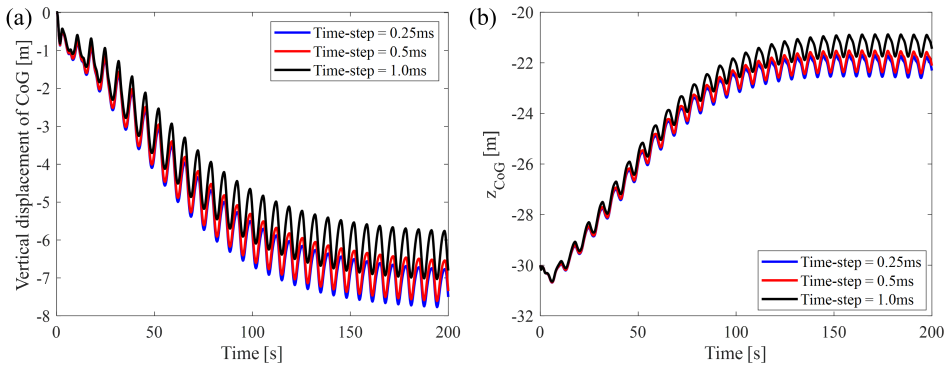

Figure 4.21: Time-step sensitivity study of the vertical displacement of the center of gravity (CoG) of (a) the floating collar and (b) the sinker tube.

Furthermore, three cases of different grids are tested for a mooring system and a fish cage. For simplicity, the grids are given the name; coarse mesh, normal mesh, and fine mesh for the mooring system. The mooring system consists of bridle lines, frame lines, and mooring lines. The mesh of the fish cage structure is held constant between the cases. Table 4.9 shows the specification of the grids utilized for the mooring system. Figure 4.22 shows a comparison of the grid sensitivity study between the coarse mesh, medium mesh, and fine mesh for the mooring system, with a single fish cage. It can be observed that the horizontal force remains consistent between the different cases.

Table 4.9: Specifications of the element size for mesh-sensitivity study of the mooring systems.

Mesh type:		Fine	Normal	Coarse
Bridle lines	Number of Element	20	10	5
	Element Length	1.5663m	3.1326m	6.2652m
Frame lines	Number of Element	40	20	10
	Element Length	2.0m	4.0m	8.0m
Mooring lines	Number of Element	100	50	25
	Element Length	2.0m	3.774m	7.547m

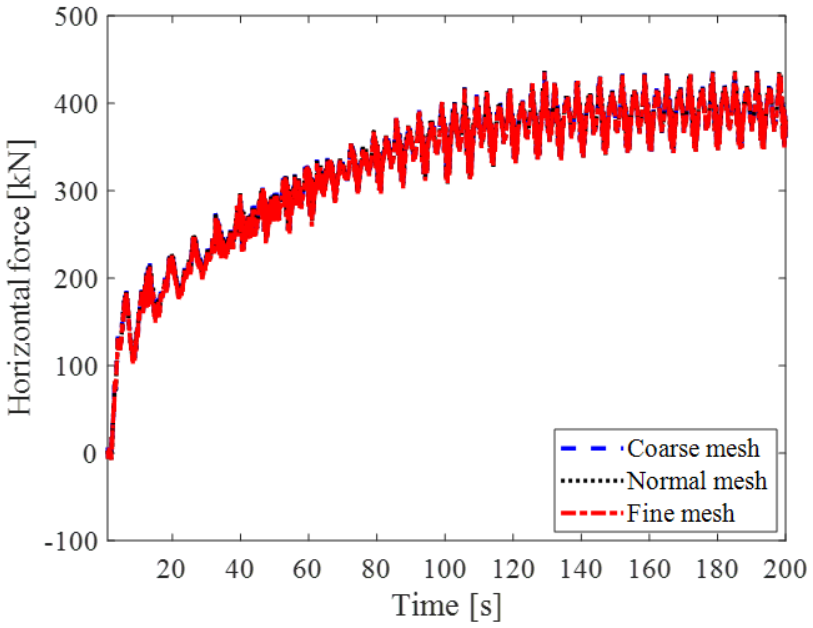

Figure 4.22: Grid sensitivity study conducted with coarse, normal, and fine mesh configurations for the mooring system of a single fish cage, under waves and currents conditions.

Figure 4.23 shows the comparison of the grid sensitivity study of the pitch angle for (a) the floating collar and (b) the sinker tube using coarse, normal, and fine mesh configurations. The pitch for the floating collar and the sinker tube remains relatively consistent between the different cases.

Figure 4.24 shows the comparison of the horizontal displacement of the pitch angle for (a) the floating collar and (b) the sinker tube using coarse, normal, and fine mesh configurations. It can be observed that the displacement is larger for the floating collar with the fine mesh compared to the coarse mesh and normal mesh. However, for the sinker tube, the displacement remains similar between the cases. Figure 4.25 shows the comparison of the vertical displacement of the pitch angle for (a) the floating collar and (b) the sinker tube using coarse, normal, and fine mesh configurations. Similar to the comparison of the horizontal displacement, it can be observed that the fine mesh differs compared to those of the coarse and normal mesh.

Overall, the tested grids can effectively capture the motion of the fish cage under the influence of waves and currents and calculate the horizontal force, pitch, horizontal displacement, and vertical displacement. The limitations of the tested grids are most noticeable for the horizontal displacement of the CoG of the floating collar (see Figure 4.24(a)) and the vertical displacement of the CoG of both the floating collar and the sinker tube (see Figure 4.25). For further study, the fine mesh should be employed for the fish cage system because the element size is small enough to accurately capture the fish cage motion and correctly calculate the studied parameters. Moreover, it can be concluded that the element sizes in the coarse and normal mesh are too large for accurate calculation.

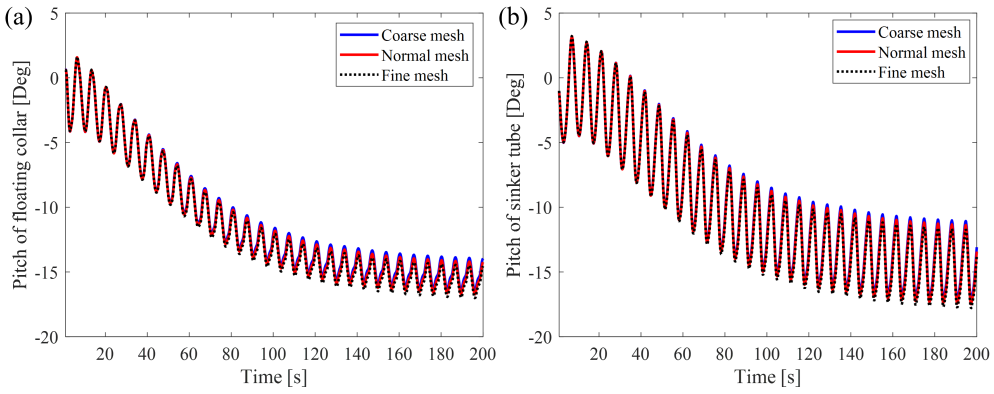

Figure 4.23: Comparison of the grid sensitivity study of the pitch angle for (a) the floating collar and (b) the sinker tube using coarse, normal, and fine mesh configurations.

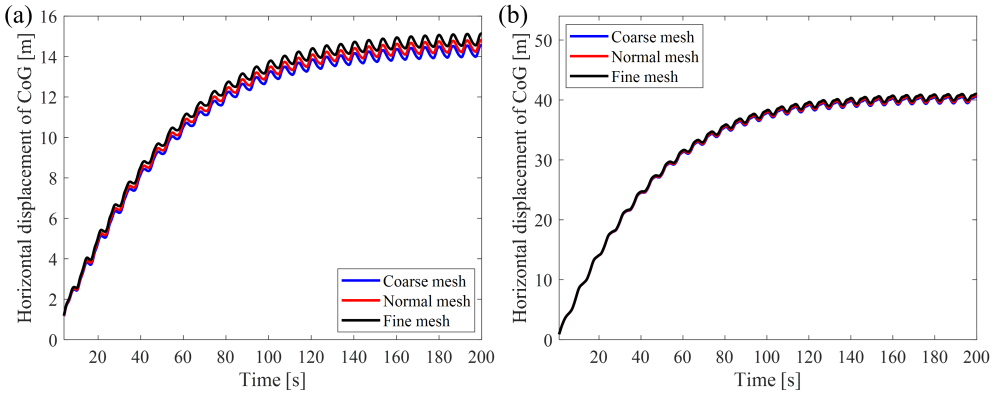

Figure 4.24: Comparison of the horizontal displacement of the pitch angle for (a) the floating collar and (b) the sinker tube using coarse, normal, and fine mesh configurations.

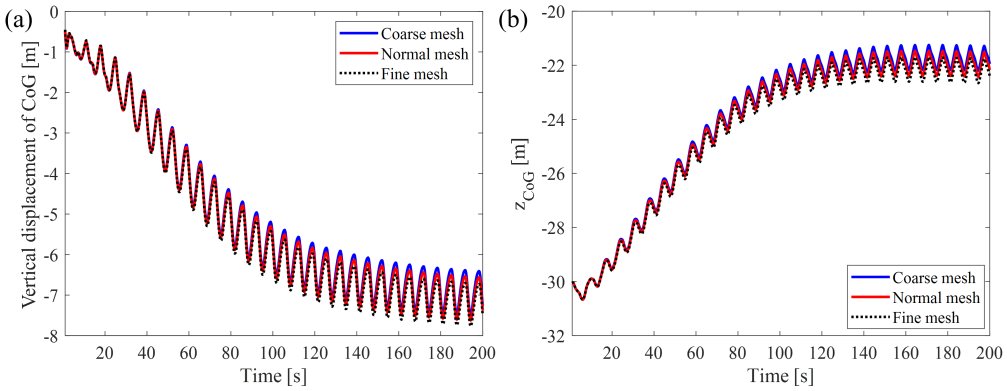

Figure 4.25: Comparison of the vertical displacement of the pitch angle for (a) the floating collar and (b) the sinker tube using coarse, normal, and fine mesh configurations.

4.4.2 Effect of wave height and current speed for different flow directions

Four different cases are examined and compared, each characterized by a distinct flow direction: 0, 15, 30, and 45 degrees, aligned with the x-axis within the

XY-plane. Figure 4.26 illustrates a single gravity-type fish cage with four different flow directions: 0, 15, 30, and 45 degrees. The following wave and current conditions are applied in the present study: wave period T=6.6s and wave height H=2.8m. The mooring lines are pre-tensioned.

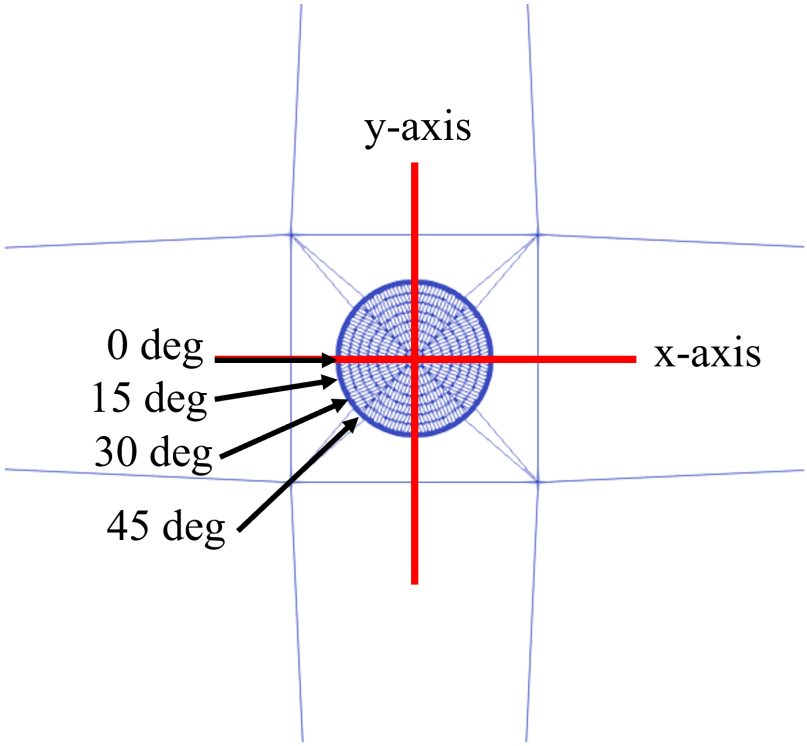

Figure 4.26: Illustration of a single gravity-type fish cage with 4 different cases where the flow directions are set at 0, 15, 30, and 45 degrees.

Figure 4.27 shows the comparison of the horizontal forces acting on the fish cage with different flow directions. It can be observed that the maximum horizontal force reaches 437.42 kN and is obtained when the flow angle is 30 degrees (aligned with the x-direction). Furthermore, as the flow angle increases, the horizontal force decreases, as the force no longer acts solely in the horizontal direction.

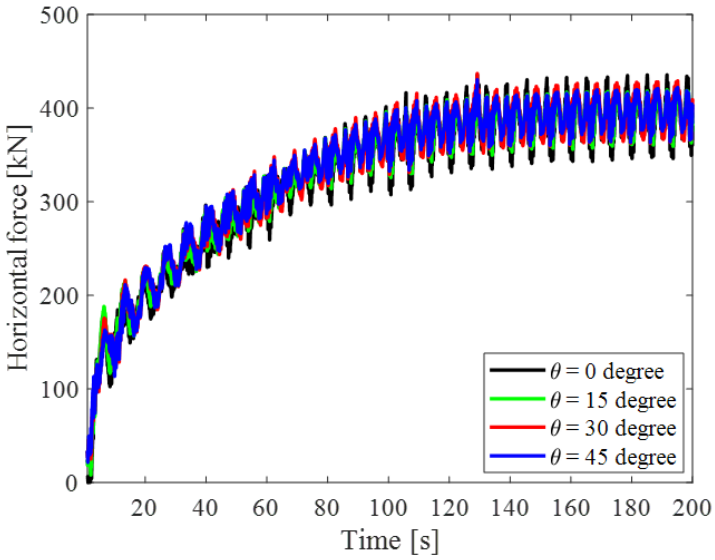

Figure 4.27: Comparison of the horizontal forces acting on the fish cage, with flow directions set to 0, 15, 30, and 45 degrees.

Figure 4.28 shows the comparison of the roll angle of (a) the floating collar and (b) the sinker tube under various flow directions. It can be observed that the maximum roll occurs for a flow direction of 45 degrees for the floating collar and the sinker tube. The maximum roll angle reaches 15.55 degrees and 12.51 degrees for the floating collar and sinker tube respectively. Furthermore, it can be observed that there will be almost no roll for the flow angle of 0 degrees.

Figure 4.29 compares the pitch angle of (a) the floating collar and (b) the sinker tube under various flow directions. Both the floating collar and the sinker tube exhibit the highest pitch when the flow angle is 0 degrees. Specifically, the maximum pitch angles for the floating collar and sinker tube are 17.61 degrees and 17.65 degrees, respectively. Interestingly, the sinker tube experiences a more pronounced pitch motion compared to the floating collar. This discrepancy can be attributed to the mooring system's role in restraining the movement of the floating collar.

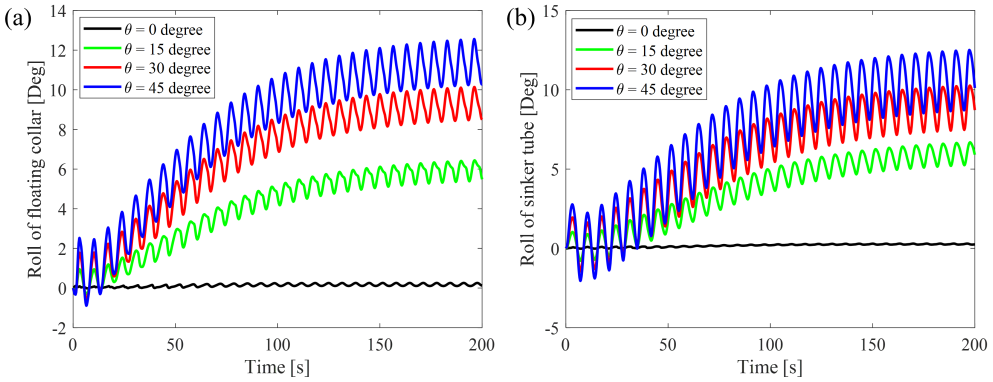

Figure 4.28: Comparison of the roll angle of (a) the floating collar and (b) the sinker tube, with flow directions set to 0, 15, 30, and 45 degrees.

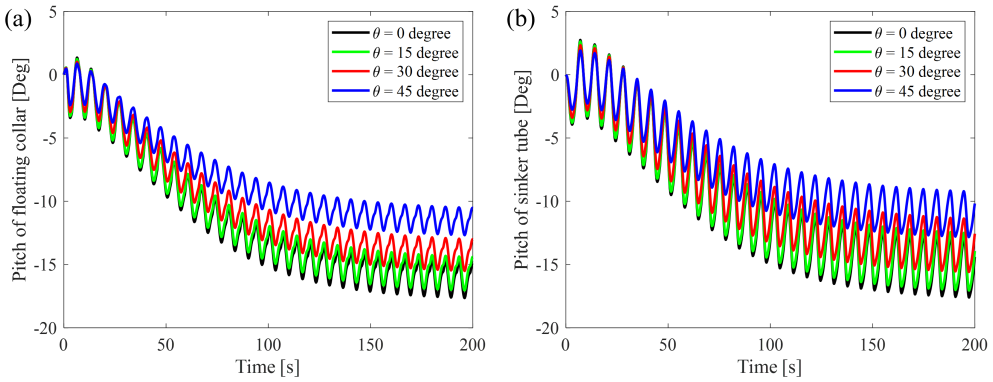

Figure 4.29: Comparison of the pitch angle of (a) the floating collar and (b) the sinker tube, with flow directions set to 0, 15, 30, and 45 degrees.

Figure 4.30 compares the horizontal displacement of the center of gravity (CoG) for (a) the floating collar and (b) the sinker tube under various flow directions. The maximum horizontal displacement for the floating collar is 15.5m, occurring when the flow angle is 0 degrees. In contrast, the sinker tube experiences a maximum horizontal displacement of 41.4m under the same flow angle.

Figure 4.31 compares the vertical displacement of the center of gravity (CoG) for (a) the floating collar and (b) the sinker tube under various flow directions. The floating collar exhibits its maximum vertical displacement of -8.16m at a flow

angle of 15 degrees. In contrast, the sinker tube's vertical displacement ranges from -30m to -22.1m under a flow direction of 0 degrees.

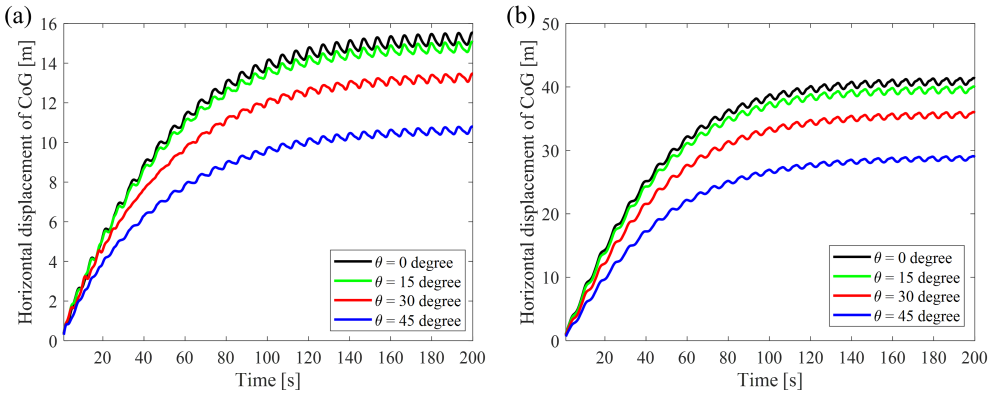

Figure 4.30: Comparison of the horizontal displacement of the center of gravity (CoG) of (a) the floating collar and (b) the sinker tub, with flow directions set to 0, 15, 30, and 45 degrees.

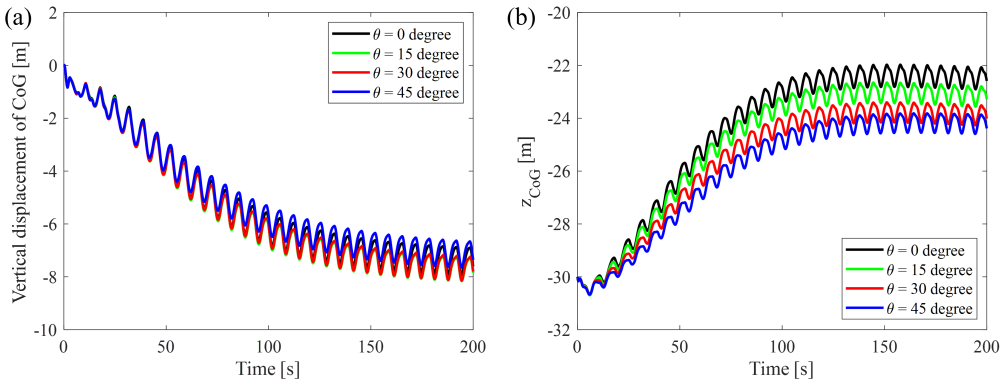

Figure 4.31: Comparison of the vertical displacement of the center of gravity (CoG) of (a) the floating collar and (b) the sinker tub, with flow directions set to 0, 15, 30, and 45 degrees.

4.4.3 Hydrodynamic behaviors of a fish cage in regular and irregular wave and current conditions

This chapter investigates and compares the hydrodynamic behaviors of a fish cage under both regular and irregular wave and current conditions. The regular wave and current parameters include a wave period of $T_{wave} = 6.6$s and wave height $H_{wave} = 2.8$m. For irregular waves, the significant wave height is $H_s = 2.8$m, and the peak period is $T_p = 6.6$s. The mooring lines are pre-tensioned with a 2% extension, and the flow direction is set at 0 degrees (refer to Figure 4.26).

Figure 4.32 compares the horizontal force acting on the pre-tensioned fish cage under both regular and irregular wave and current conditions. It is evident that the force exerted on the structure due to regular waves increases uniformly, whereas, for irregular waves, the force increases more gradually and non-uniformly. However, the maximum horizontal force under regular and irregular wave and current conditions reaches 426.92 kN and 435.49 kN, respectively.

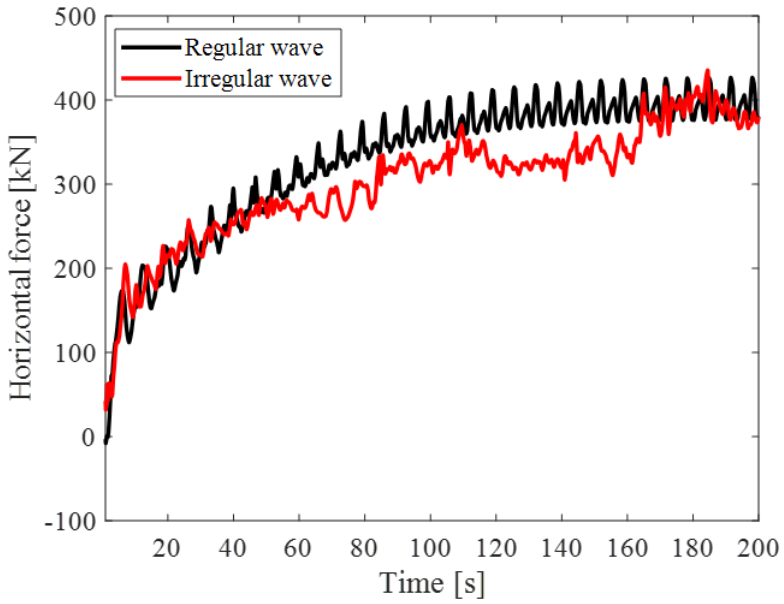

Figure 4.32: Comparison between the horizontal forces in regular wave ($T_{wave} = 6.6$s, $H_{wave} = 2.8$m) and irregular ($H_s = 2.8$m, $T_p = 6.6$s) wave and current conditions.

Figure 4.33 compares the pitch angle of (a) the floating collar and (b) the sinker tube under regular and irregular wave and current conditions. As shown in Figure 4.33(a), the pitch angle of the floating collar is higher for regular waves compared to irregular waves. The maximum pitch angle under regular and irregular wave and current conditions reaches 17.65 degrees and 16.1 degrees, respectively. Similarly, in Figure 4.33(b), it can be observed that the pitch angle for the sinker tube is larger in regular waves, reaching 17.56 degrees, while the maximum pitch angle in irregular waves is 15.88 degrees.

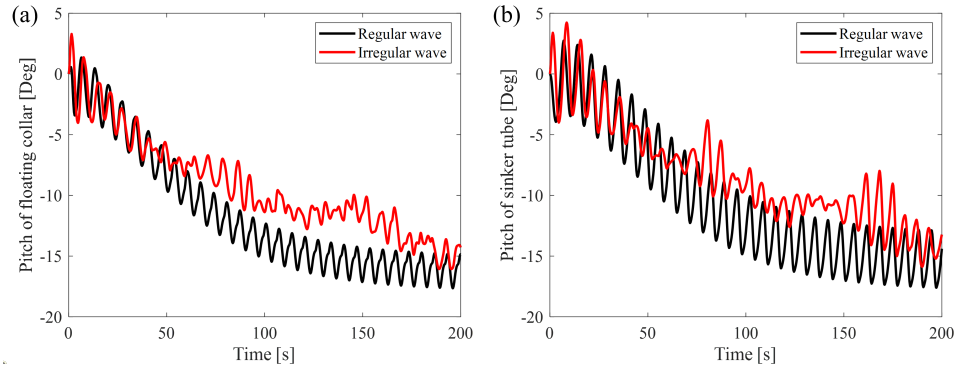

Figure 4.33: Comparison between the pitch angle of (a) the floating collar and (b) the sinker tube, in regular wave ($T_{wave} = 6.6$s, $H_{wave} = 2.8$m) and irregular ($H_s = 2.8$m, $T_p = 6.6$s) wave and current condition.

Figure 4.34 compares the horizontal displacement of the center of gravity CoG of (a) the floating collar and (b) the sinker tube of the pre-tensioned fish cage under regular and irregular wave and current conditions. It can be observed that the maximum horizontal displacement of the CoG of the floating collar is 15.54m in regular waves and 15.21m in irregular waves. For the sinker tube, the maximum horizontal displacement of the CoG is 40.41m and 41.35m for regular and irregular waves, respectively.

Figure 4.35 compares the vertical displacement of the center of gravity CoG of (a) the floating collar and (b) the sinker tube of the pre-tensioned fish cage under regular and irregular wave and current conditions. The displacement of the CoG is larger for the floating collar in regular waves, reaching 7.93m compared

to 7.35m in irregular waves. However, for the sinker tube, the Z_{CoG} is largest in irregular waves going from its original point at Z=-30m to -21.59m, compared to -30 to -22.07m in regular waves.

Figure 4.36 and Figure 4.37 show the deformations and tensions of the fish cage from (a) 0s to (f) 200s under regular and irregular wave and current conditions, respectively. It can be observed that the maximum tensions are located in the mooring lines in front of the fish cage, as well as the outer bridle lines connecting the fish cage to the grid frame.

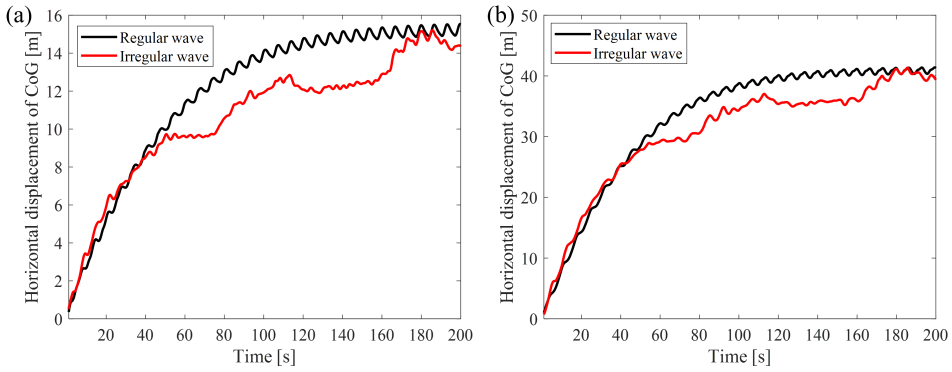

Figure 4.34: Comparison between the horizontal displacements of CoG of (a) the floating collar and (b) the sinker tube, in regular wave ($T_{wave} = 6.6$s, $H_{wave} = 2.8$m) and irregular ($H_s = 2.8$m, $T_p = 6.6$s) wave and current conditions.

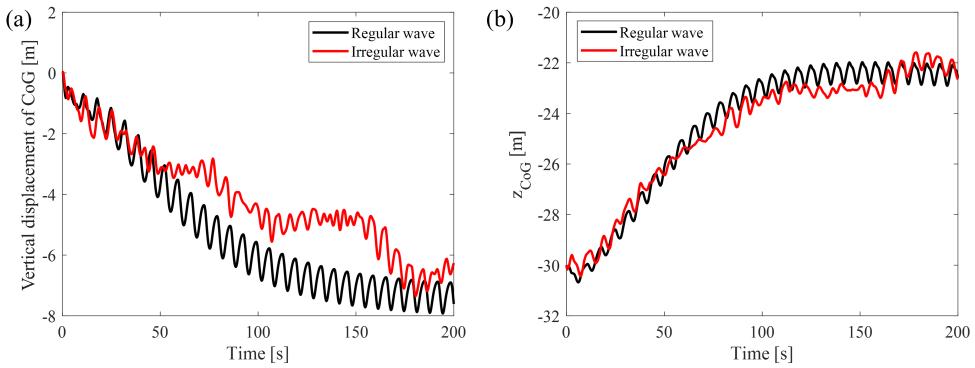

Figure 4.35: Comparison between the vertical displacement of CoG of (a) the floating collar and (b) the sinker tube, in regular wave ($T_{wave} = 6.6$s, $H_{wave} = 2.8$m) and irregular ($H_s = 2.8$m, $T_p = 6.6$s) wave and current condition.

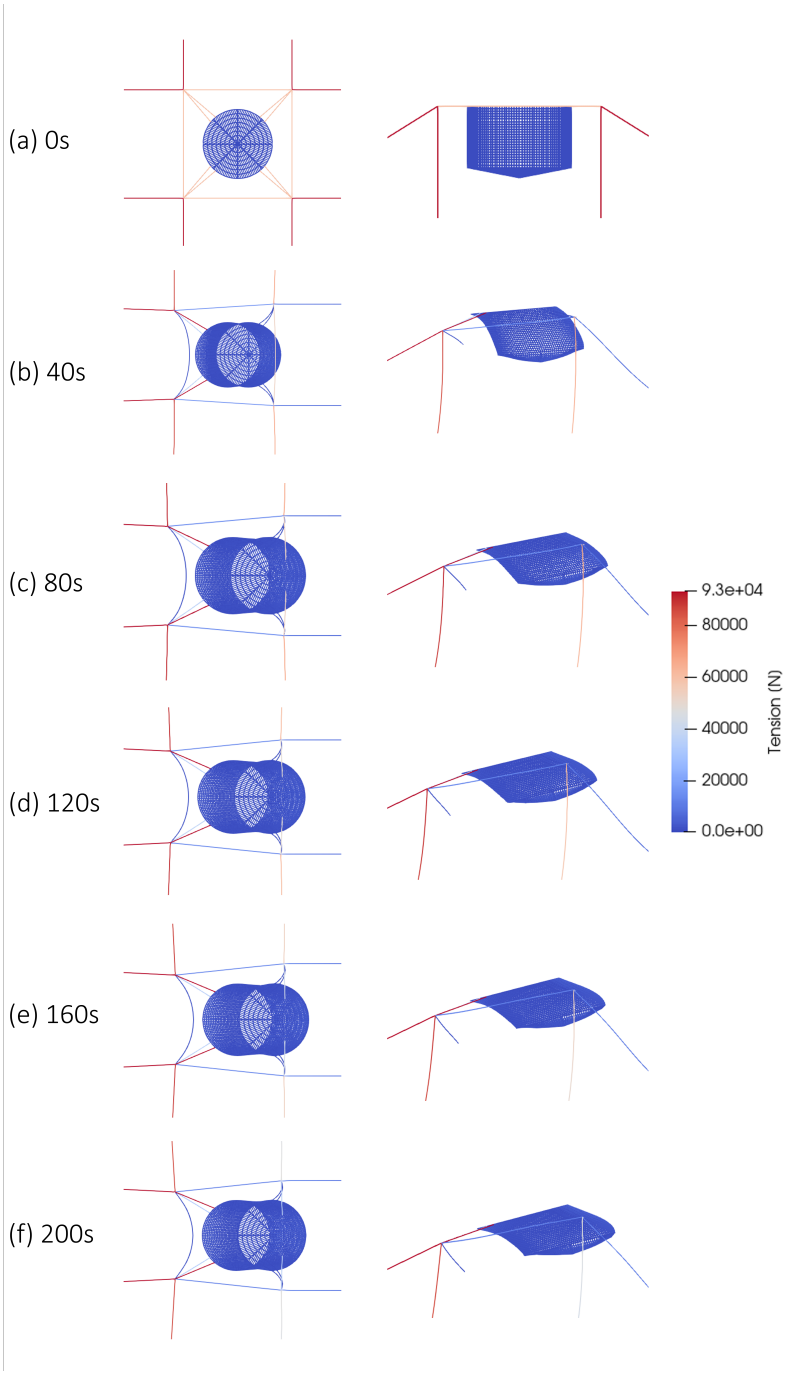

Figure 4.36: Deformations and tensions of the fish cage from (a) 0s to (f) 200s, with time increments of 40s, of the hydrodynamic response with time-step of 0.5ms, in top-view and side-view, under regular wave and current conditions.

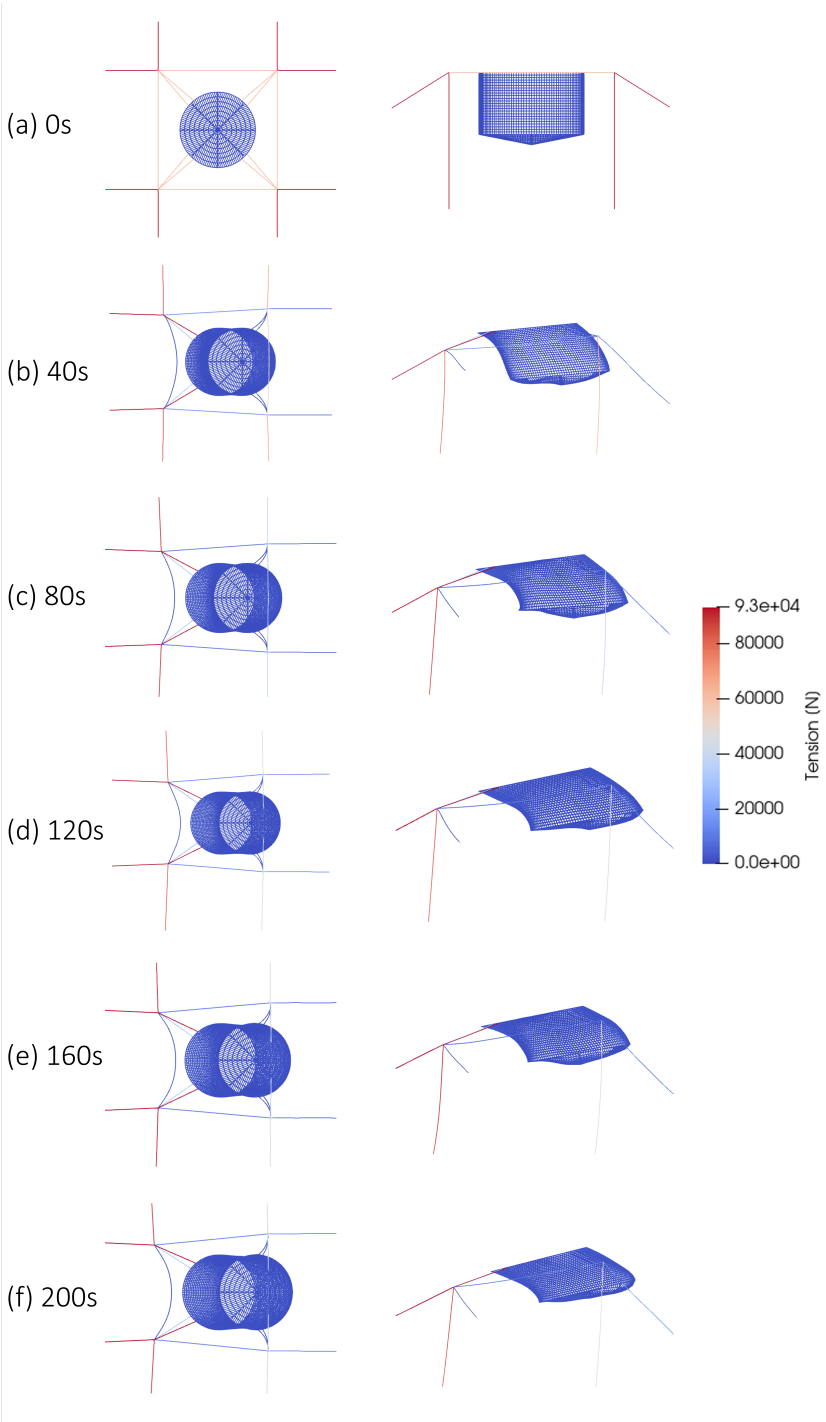

Figure 4.37: Deformations and tensions of the fish cage from (a) 0s to (f) 200s, with time increments of 40s, of the hydrodynamic response with time-step of 0.5ms, in top-view and side-view, under irregular wave and current conditions.

4.4.4 Effect of pre-tension on fish cage mooring systems

The effect of pre-tension on the mooring system for a fish cage will be examined and compared. Two critical areas are important to study. The first part involves applying tension to the mooring system, which helps to mitigate the initial impact force on the mooring system caused by waves and currents. The second part concerns the behavior of the mooring system when submerged in water: the mooring lines tend to shrink. By adding extensions to the mooring lines, it can influence the dynamic behavior of the structure. Three cases are tested, where the extensions on the mooring lines are chosen as 0%, 2%, and 4%. Figure 4.38 shows the comparison of the horizontal forces acting on the fish cage. The maximum horizontal force for 0%, 2%, and 4% reaches 447.9kN, 426.7kN, and 409.1kN, respectively. It can be observed that without pre-tension in the mooring system, the forces acting on the fish cage structure will build up to be larger compared to applying pre-tension. However, it can be observed at the beginning of the simulation, during the time interval [0s-7s], for the extension of 0%, that it takes some extra time before the force starts increasing. Between [30s-80s], the increasing force acting on the structure is similar. After 80s, the force acting on the mooring system with an extension of 0% increases more rapidly.

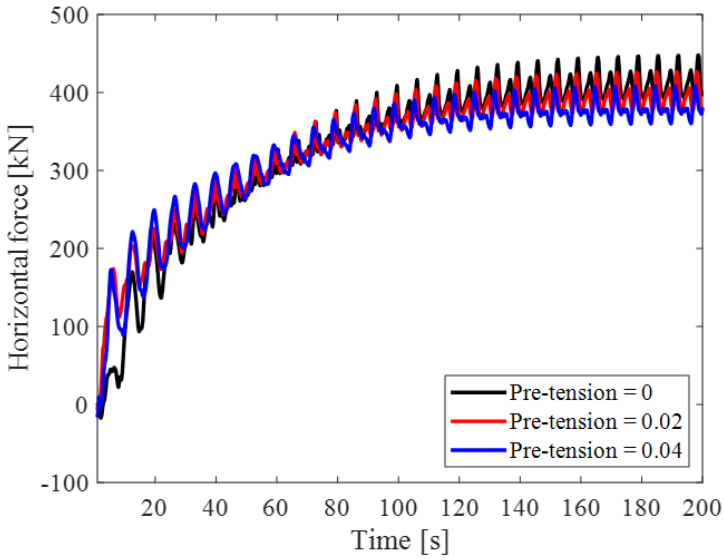

Figure 4.38: Comparison of the horizontal forces acting on the fish cage, when the mooring system is pre-tensioned using extensions of 0%, 2%, and 4%.

Figure 4.39 shows the comparison between the pitch angle of (a) the floating collar and (b) the sinker tube for a fish cage, when the mooring system is pre-tensioned. As shown in the figure, applying pre-tension in the mooring system will result in increased pitch motion. By comparing the floating collar and the sinker tube, it can be observed a significant difference in the pitch motion between the cases. Without any tension, the maximum pitch angle reaches 14.22 degrees and 13.9 degrees for the floating collar and sinker tube, respectively. At 2% extension, the maximum pitch angle is 17.65 degrees and 17.57 degrees. Lastly, at 4% extension, the maximum pitch angle is 21.71 degrees and 22.04 degrees for the floating collar and sinker tube, respectively. This results in a difference in pitch angle of 7.49 degrees for the floating collar and 8.14 degrees for the sinker tube. Furthermore, it can be observed that the pitching motion rapidly increases for the structure with the largest mooring line extension.

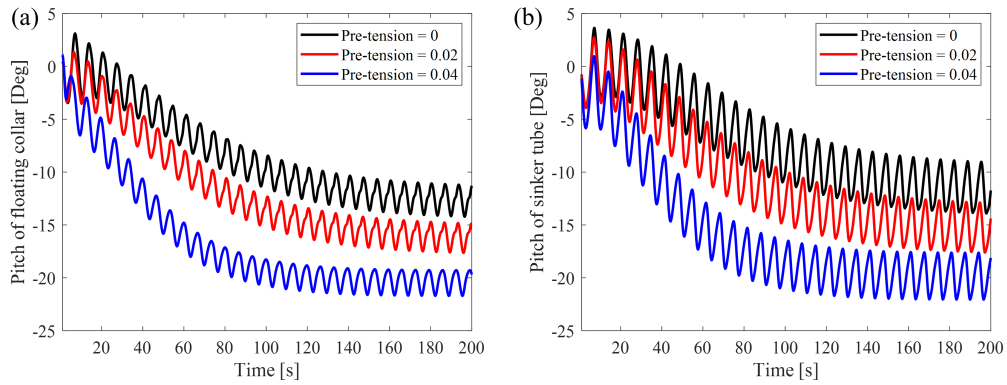

Figure 4.39: Comparison of the pitch angle of (a) the floating collar and (b) the sinker tube on a fish cage, when the mooring system is pre-tensioned using extensions of 0%, 2%, and 4%.

Figure 4.40 shows the comparison of the horizontal displacement of the CoG of (a) the floating collar and (b) the sinker tube for a fish cage, when the mooring system is pre-tensioned. It can be observed that the mooring system without any pre-tensioning will experience the longest horizontal displacement of the CoG. Maximum X_{CoG} is 20.19m and 47.72m for the floating collar and sinker tube, respectively. Moreover, the maximum X_{CoG} with 2% extension is 15.73m and 41.37m, and for the 4% extension it is 10.87m and 36.18m for the floating collar and sinker tube, respectively.

Figure 4.41 shows the comparison of the vertical displacement of the CoG of (a) the floating collar and (b) the sinker tube for a fish cage, when the mooring system is pre-tensioned. Similarly to the horizontal displacement, the maximum vertical displacement of the CoG can be observed for the mooring system without any pre-tensioning. As shown in Figure 4.41(a), maximum vertical displacement for the mooring system with 0%, 2%, and 4% is 6.21m, 7.92m and 10.36m, respectively. As shown in Figure 4.41(b), maximum Z_{CoG} for the mooring system with 0%, 2%, and 4% is goes from -30m to: -19.23m, -22.07m, and -25.93m, respectively.

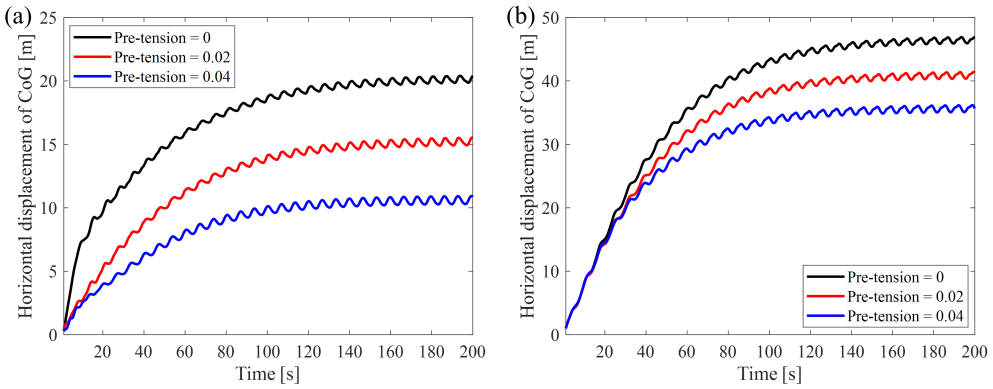

Figure 4.40: Comparison of the horizontal displacement of the CoG of (a) the floating collar and (b) the sinker tube on a fish cage, when the mooring system is pre-tensioned using extensions of 0%, 2%, and 4%.

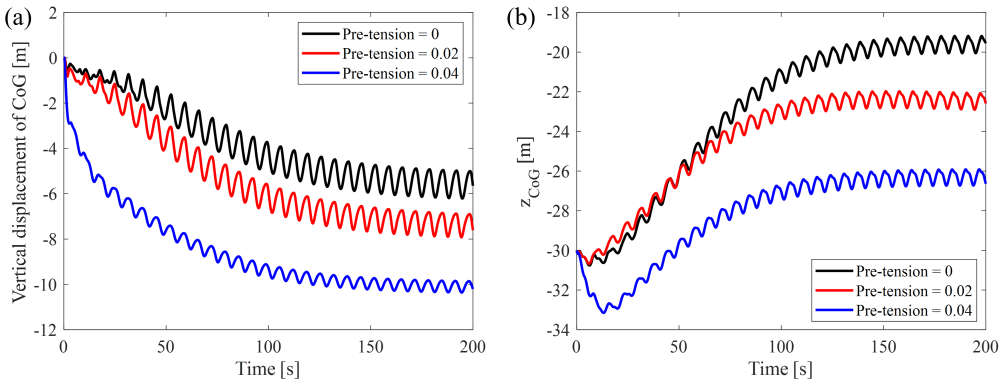

Figure 4.41: Comparison of the vertical displacement of the CoG of (a) the floating collar and (b) the sinker tube on a fish cage, when the mooring system is pre-tensioned using extensions of 0%, 2%, and 4%.

4.5 Dynamic response of multiple gravity-type fish cages to regular and irregular waves and current in extreme conditions

The effect of regular and irregular waves and current conditions on multiple fish cages will be examined and compared. The extension of the mooring lines is set to 2% and the flow direction is set to 0 degrees. Furthermore, the wave conditions are set to: $T_{wave} = 6.6$s, $H_{wave} = 2.8$m and $T_p = 6.6$s, $H_s = 2.8$m for regular and irregular waves, respectively. The current profile remains the same as before (see Table 4.2).

In this section, six different cases are studied, labeled as ”1x1 fish cage”, ”2x1 fish cage”, ”2x2 fish cage”, ”3x1 fish cage”, ”3x2 fish cage” and ”4x2 fish cage”. For simplicity the cases are labeled according to the amount of fish cages in the mesh in x- and y-direction accordingly. For example, a ”4x2 fish cage” has 4 cages in the x-direction and 2 cages in the y-direction, 8 cages in total.

Section 4.5.1 covers the effect of regular waves while section 4.5.2 covers the effect of irregular waves.

4.5.1 Effect of regular waves on multiple fish cages

Figure 4.42 shows the comparison of the horizontal forces acting on multiple fish cages in regular wave and current conditions. It can be observed that the maximum tension reaches 2913.1 kN for the 4x2 fish cage mesh, which is 6.8 times larger than the horizontal force calculated for the single sigh cage. Furthermore, it can be observed that the horizontal force increases according to the amount of fish cages in the mesh. Moreover, the force difference between ”4x2 fish cage” and ”3x2 fish cage” compared to ”3x2 fish cage” and ”2x2 fish cage” has a significantly larger increase when adding two additional fish cages, indicating a more aggressive increase in the horizontal force as more fish cages are included.

Figure 4.43 shows the comparison of the pitch angle of (a) the floating collar and (b) the sinker tube for multiple fish cages. The maximum pitch angle reaches -22.8 degrees and -23.2 degrees and is observed in the 2x1 fish cage for the floating

collar and sinker tube, respectively. The fish cages 1x1, 3x2, and 4x2 are shown to have lower pitch angles for rigid bodies compared to the rest of the fish cages.

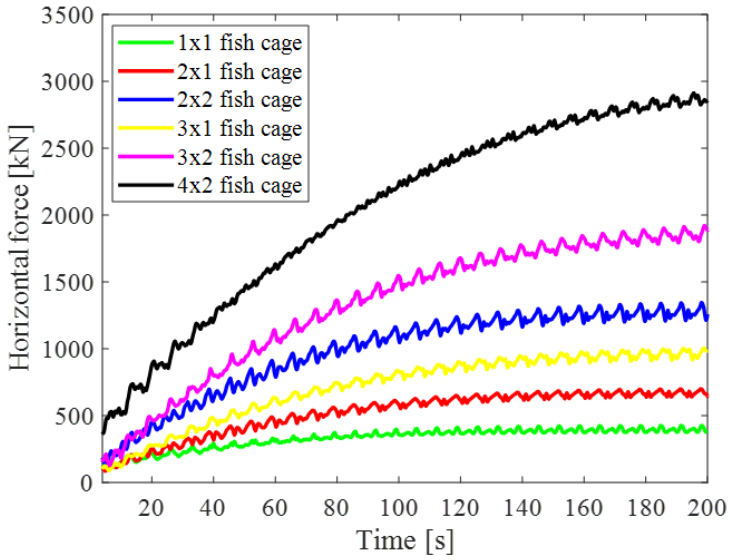

Figure 4.42: Comparison of the horizontal forces acting on multiple fish cages in regular waves ($T_{wave} = 6.6$s, $H_{wave} = 2.8$m), with flow directions set to 0 degrees, extension on mooring lines set to 2%.

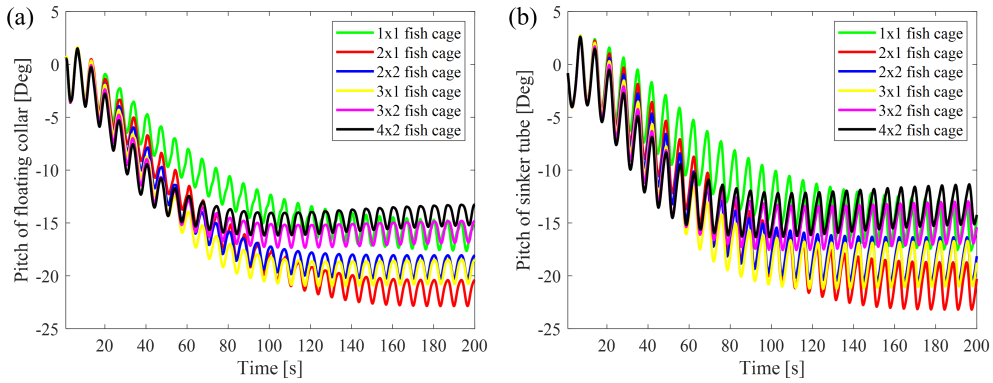

Figure 4.43: Comparison of the pitch angle of (a) the floating collar and (b) the sinker tube in regular waves ($T_{wave} = 6.6$s, $H_{wave} = 2.8$m), with flow directions set to 0 degrees, extension on mooring lines set to 2%.

Figure 4.44 shows the comparison of the horizontal displacement of the center of gravity of (a) the first floating collar and (b) the first sinker tube for multiple fish cages. It can be observed that the displacement of CoG is larger and increasing more rapidly for the sinker tube compared to the floating collar. For the first time interval [0s,30s] the displacement of CoG for the sinker tube remains relatively consistent between the meshes. Between [30s,80s] it can be seen that the displacement of the CoG of sinker tube in fish cage 3x2 and 4x2 keep increasing at the same rate. Maximum horizontal displacement of CoG is 33.1m for the floating collar and 57.6m for the sinker tube, respectively.

Figure 4.45 shows the comparison of the vertical displacement of the center of gravity of (a) the first floating collar and (b) the first sinker tube for multiple fish cages. It can be observed that the maximum displacement of Z_{CoG} is located in the 4x2 fish cage for both the floating collar and the sinker tube. The maximum displacement of CoG for the floating collar is -24.8m, while for the sinker tube, it ranges from -30m to -42.1m. Furthermore, it can also be observed that the Z_{CoG} for the sinker tube decreases with an increasing number of sinker tubes. For the fish cages 1x1 and 2x1, the Z_{CoG} shifts upwards (closer to the floating collar). Moreover, for the 2x2 fish cage, the Z_{CoG} remains relatively stable, while for the remaining configurations, the Z_{CoG} shifts downwards.

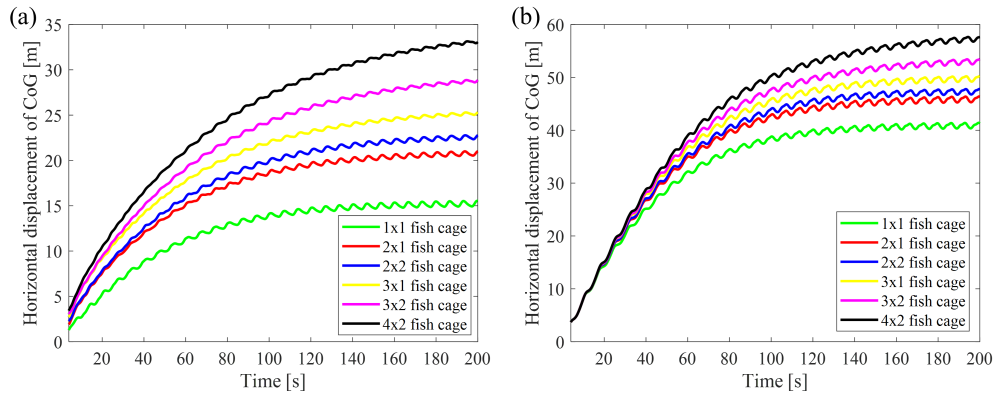

Figure 4.44: Comparison of the horizontal displacement of the center of gravity of (a) the floating collar and (b) the sinker tube in regular waves ($T_{wave} = 6.6$s, $H_{wave} = 2.8$m), with flow directions set to 0 degrees, extension on mooring lines set to 2%.

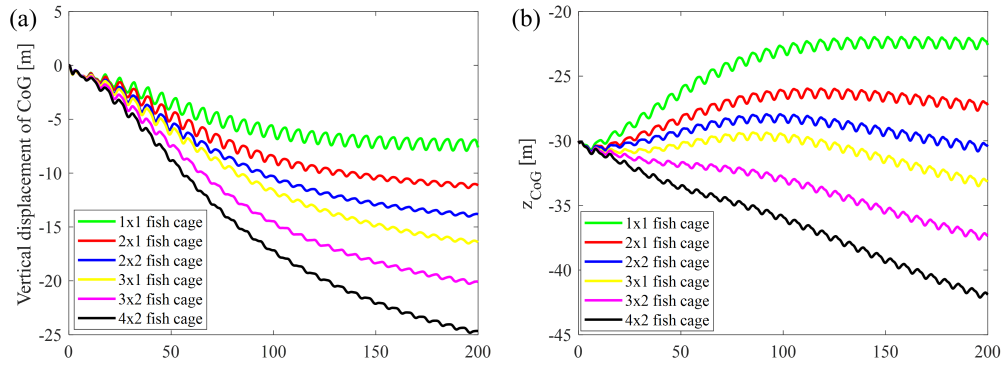

Figure 4.45: Comparison of the vertical displacement of the center of gravity of (a) the floating collar and (b) the sinker tube in regular waves ($T_{wave} = 6.6$s, $H_{wave} = 2.8$m), with flow directions set to 0 degrees, extension on mooring lines set to 2%.

Table 4.10 shows the results of the calculated values for the maximum hydrodynamic response of the tested fish cages, under regular wave and current conditions. Figure 4.46 and Figure 4.47 show maximum deformations and tensions of the fish cages from (a) 1x1 fish cage to (f) 4x2 fish cage, with a time-step

of 0.5ms, in side-view and top-view, respectively. It can be observed that the maximum tension acting on the fish cages is located in the mooring lines in front, the side, and the bridle lines facing the current direction. In Figure 4.46, it can be observed for fish cages (b) to (f) that the last cages will experience the largest net deformation. Furthermore, the front cages tend to be pulled down under the waterline due to the forces acting on the structure.

Table 4.10: Calculated values for the maximum hydrodynamic response of multiple fish cages under regular wave and current conditions.

Fish cage	1x1	2x1	2x2	3x1	3x2	4x2
Horizontal force [kN]	426.9	700.7	1346.01	1001.6	1922.7	2913.1
Pitch angle (floating collar) [deg]	-17.6	-22.8	-20.3	-21.0	-17.3	-16.2
Pitch angle (sinker tube) [deg]	-17.6	-23.2	-20.6	-21.0	-16.9	-15.1
X_{CoG} (floating collar) [m]	15.5	21.0	22.7	25.3	28.9	33.1
X_{CoG} (sinker tube) [m]	41.4	46.4	47.8	50.2	53.4	57.6
Z_{CoG} (floating collar) [m]	-7.9	-11.4	-14.0	-16.5	-20.3	24.8
Z_{CoG} (sinker tube) [m]	-22.9	-27.7	-30.8	-33.5	-37.6	-42.1

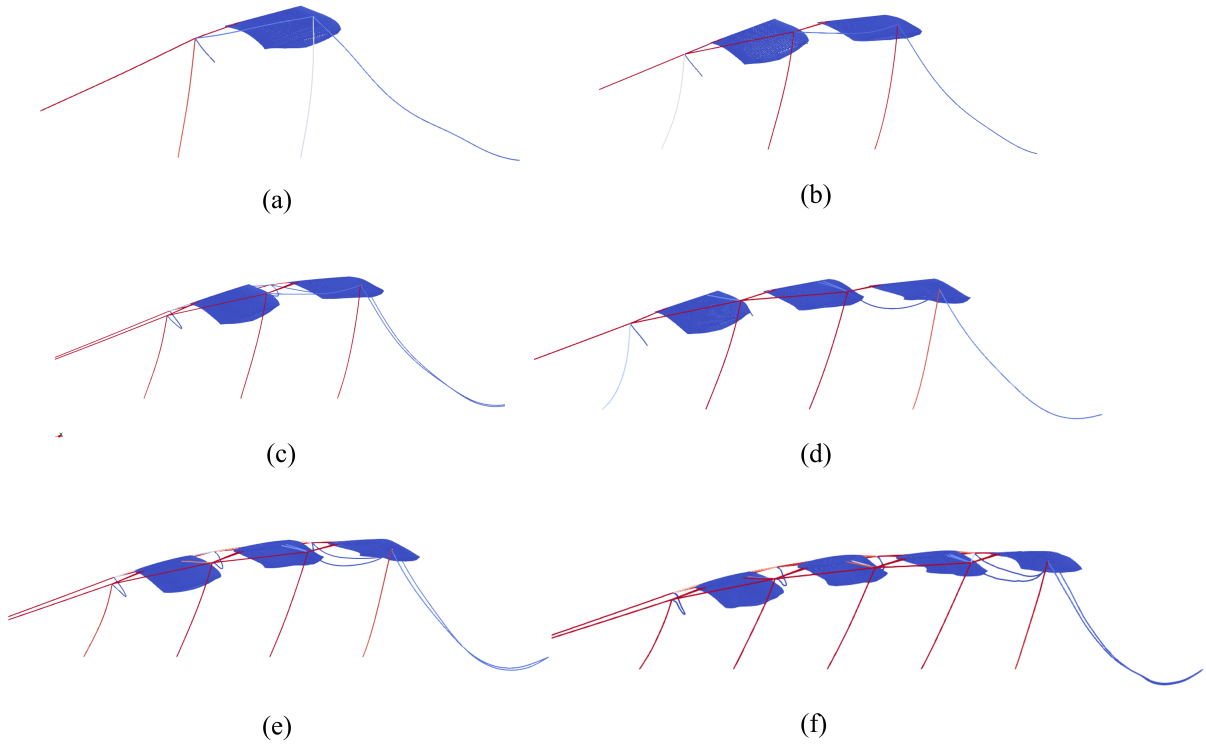

Figure 4.46: Deformations and tensions of the fish cages from (a) 1x1 fish cage to (f) 4x2 fish cage, with a time-step of 0.5ms, in side-view, under regular wave and current conditions.

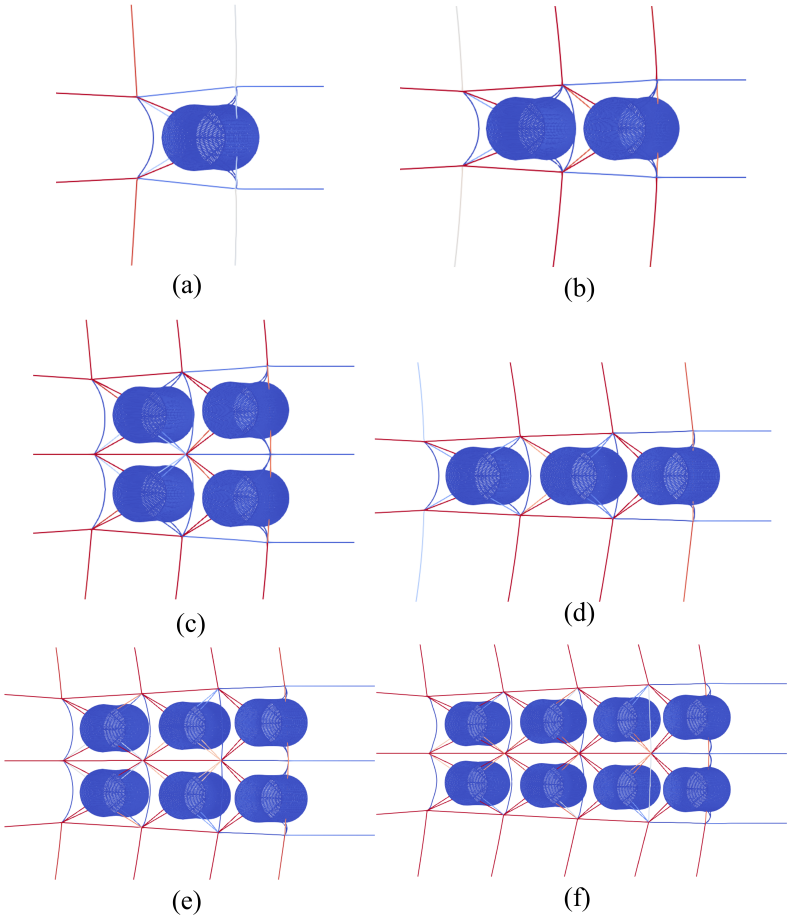

Figure 4.47: Deformations and tensions of the fish cages from (a) 1x1 fish cage to (f) 4x2 fish cage, with a time-step of 0.5ms, in top-view, under irregular wave and current conditions.

4.5.2 Effect of irregular waves on multiple fish cages

Figure 4.48 shows the comparison of the horizontal forces acting on multiple fish cages. It can be observed that the maximum horizontal force reaches 2499.0kN for the 4x2 fish cage, which is lower compared to the forces calculated for the same case in regular waves that reached 2913.1kN. The force acting in the horizontal direction is 5.8 times larger for the 4x2 fish cage compared to the 1x1 fish cage.

Figure 4.49 shows the comparison of the pitch angle of (a) the floating collar and (b) the sinker tube. The maximum pitch angle can be observed for the 3x1 fish cage, reaching an angle of -22.1 degrees for the floating collar and -22.1 degrees for the sinker tube.

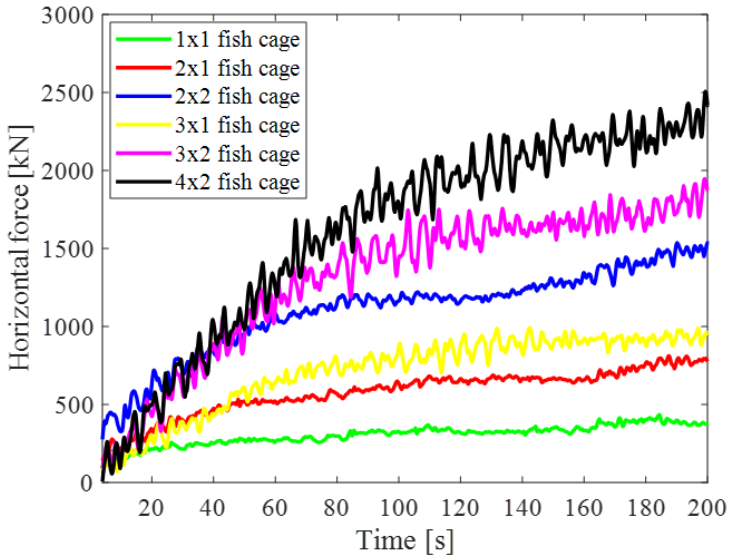

Figure 4.48: Comparison of the horizontal forces acting on multiple fish cages in irregular waves ($T_p = 6.6$s, $H_s = 2.8$m), with flow directions set to 0 degrees, extension on mooring lines set to 2%.

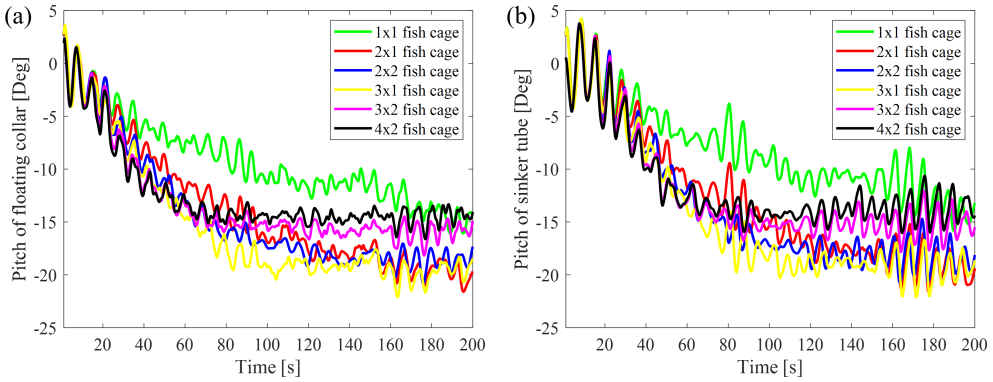

Figure 4.49: Comparison of the pitch angles of (a) the floating collar and (b) the sinker tube in irregular waves ($T_p = 6.6$s, $H_s = 2.8$m), with flow directions set to 0 degrees, extension on mooring lines set to 2%. Results are calculated for the floating collars and sinker tubes directly opposing the current.

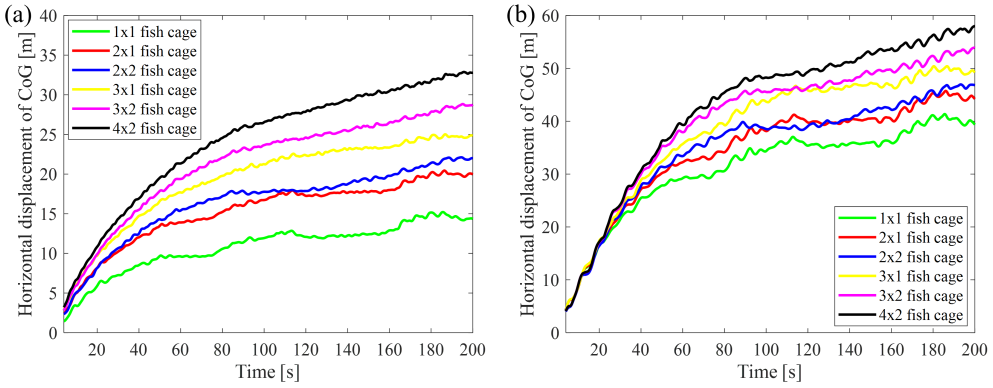

Figure 4.50: Comparison of the horizontal displacement of the center of gravity of (a) the floating collar and (b) the sinker tube in irregular waves ($T_p = 6.6$s, $H_s = 2.8$m), with flow directions set to 0 degrees, extension on mooring lines set to 2%. Results are calculated for the floating collars and sinker tubes directly opposing the current.

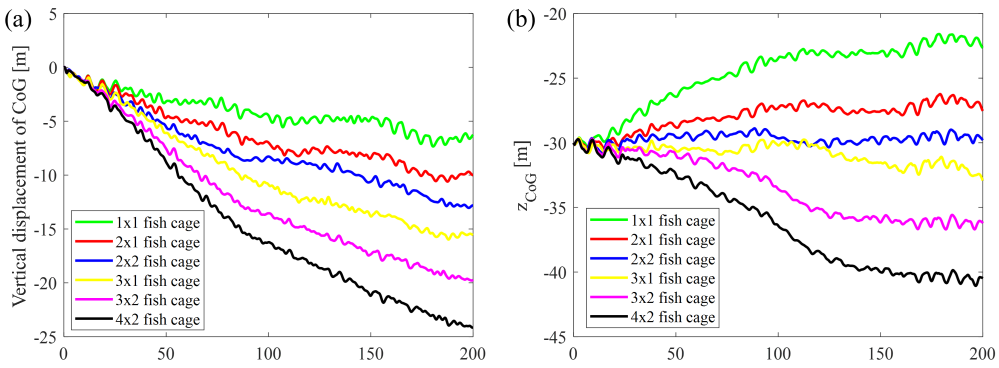

Figure 4.51: Comparison of the vertical displacement of the center of gravity of (a) the floating collar and (b) the sinker tube in irregular waves ($T_p = 6.6$s, $H_s = 2.8$m), with flow directions set to 0 degrees, extension on mooring lines set to 2%. Results are calculated for the floating collars and sinker tubes directly opposing the current.

Table 4.11 shows the results of the calculated values for the maximum hydrodynamic response of the tested fish cages, under irregular wave and current conditions. Figure 4.52 and Figure 4.53 show maximum deformations and tensions of the fish cages from (a) 1x1 fish cage to (f) 4x2 fish cage, with a time-step of 0.5ms, in side-view and top view, respectively. Similarly to the fish cages in regular waves, it can be observed that the maximum tension acting on the fish cages is located in the mooring lines in front, the side, and the bridle lines facing the current direction. In Figure 4.52 it can be observed for fish cages (b) to (f) that the last cages will experience the largest net deformation. Furthermore, the front cages tend to be pulled down under the waterline due to the forces acting on the structure.

Table 4.11: Calculated values for the dynamic response of multiple fish cages in irregular wave and current conditions.

Fish cage	1x1	2x1	2x2	3x1	3x2	4x2
Horizontal force [kN]	435.5	812.8	1537.1	988.2	1947.9	2499.0
Pitch angle (floating collar) [deg]	-16.0	-21.6	-21.0	-22.1	-18.2	-16.6
Pitch angle (sinker tube) [deg]	-15.8	-21.6	-20.7	-22.1	-17.8	-16.0
X_{CoG} (floating collar) [m]	15.2	20.4	22.1	24.9	28.8	32.9
X_{CoG} (sinker tube) [m]	41.3	45.7	46.9	50.3	53.9	58.0
Z_{CoG} (floating collar) [m]	-21.6	-26.3	-29.0	-32.4	-36.6	-41.1
Z_{CoG} (sinker tube) [m]	-7.3	-10.6	-13.0	-16.0	-19.8	-24.5

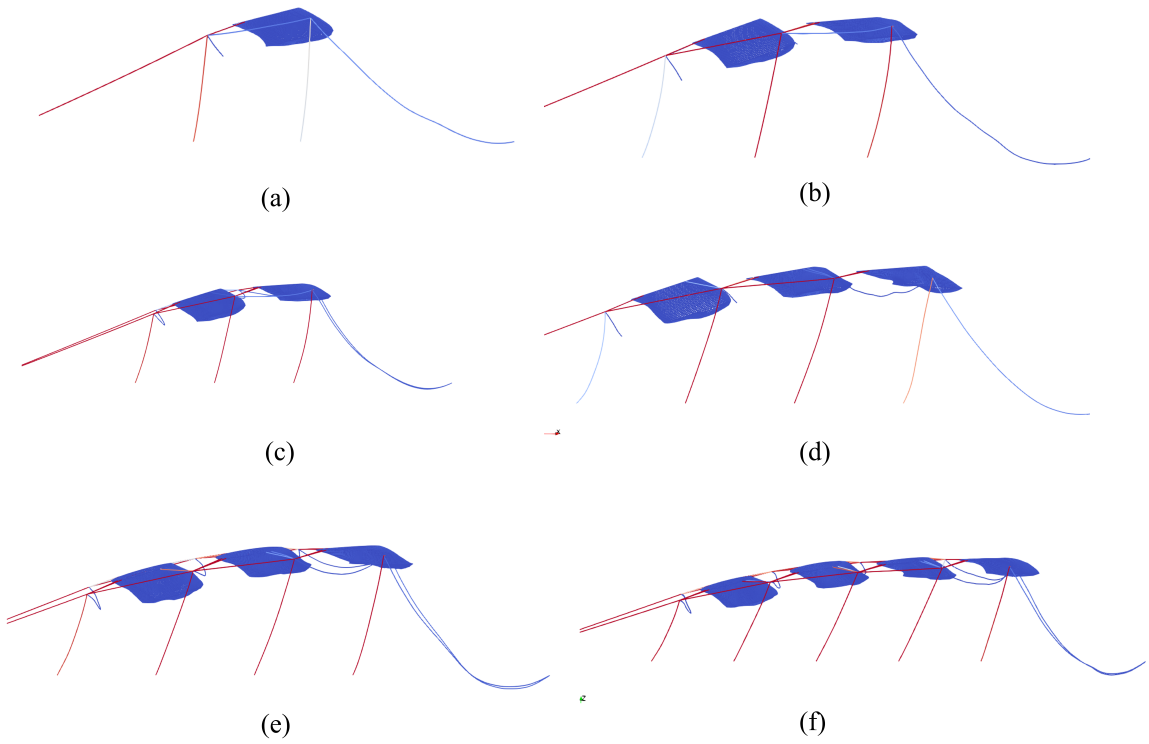

Figure 4.52: Deformations and tensions of the fish cages from (a) 1x1 fish cage to (f) 4x2 fish cage, with a time-step of 0.5ms, in side-view, under irregular wave and current conditions.

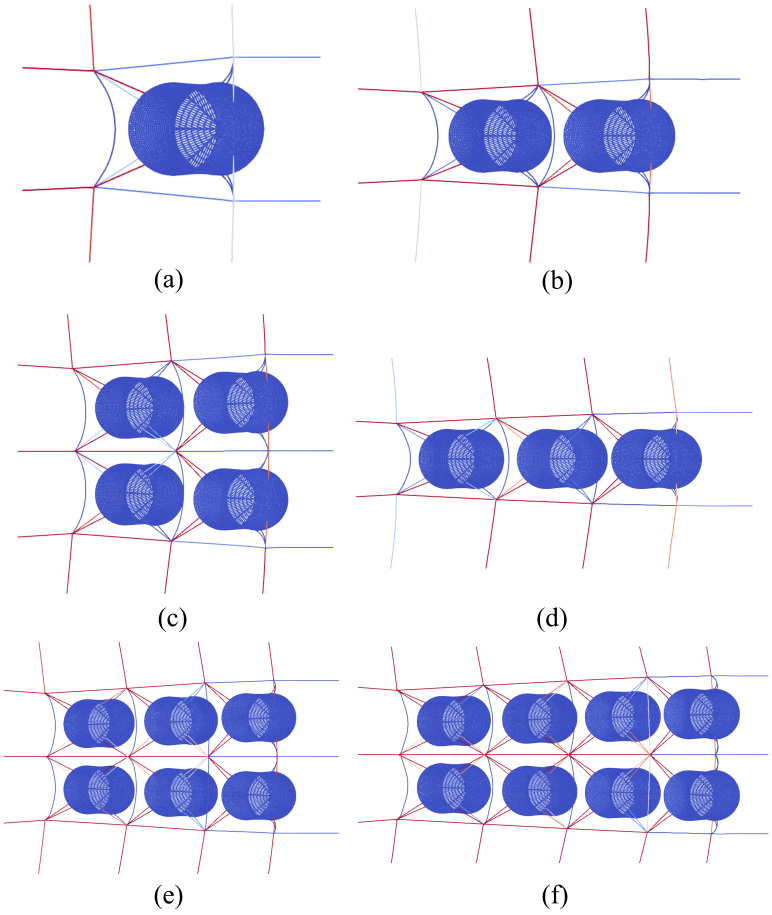

Figure 4.53: Deformations and tensions of the fish cages from (a) 1x1 fish cage to (f) 4x2 fish cage, with a time-step of 0.5ms, in top-view, under irregular wave and current conditions.

4.6 Conclusion

The dynamic response of multiple fish cages with mooring lines under regular and irregular wave and current conditions is investigated in the present study. The structural deformations of the tested fish cage netting are obtained using a modified XPBD algorithm, with correction forces to accurately predict tensions. The present XPBD algorithm is validated against and compared with the experi-

mental results of a vertical net panel. A comparison study has been conducted to further validate the modified XPBD algorithm against experimental and numerical results. Grid- and time-step sensitivity studies are conducted for the dynamic response of the fish cages. Results show that the maximum pitch angle of the floating collar and sinker tube, the horizontal displacement, and the vertical displacement are reached when the flow angle is 0 degrees. However, the maximum horizontal force is observed when the flow angle is 30 degrees and the maximum roll angle is observed when the flow angle is 45 degrees. The effect of regular and irregular waves acting on a single fish cage with a mooring system does not have significant changes for the maximum calculated values; however, the fish cage will have an increased pitch angle under regular waves. Results show that the suggested extension of the mooring lines should be 2%, based on the extensions tested in the present study. Furthermore, the effect of regular wave and current conditions will result in larger values of the dynamic response for the tested parameters.

References

[1] Malcolm Beveridge and Jon Arne Grøttum. “A review of cage culture: northern Europe.” In: (Jan. 2007), pp. 129–158. URL: https://www.researchgate.net/publication/257655031_A_review_of_cage_culture_northern_Europe.

[2] Francesco Cardia and A. Lovatelli. *Aquaculture operations in floating HDPE cages. A field handbook.* Jan. 2017.

[3] J. DeCew et al. “Modeling of dynamic behavior of a single-point moored submersible fish cage under currents”. In: *Aquacultural Engineering* 43.2 (2010), pp. 38–45. ISSN: 0144-8609. DOI: https://doi.org/10.1016/j.aquaeng.2010.05.002. URL: https://www.sciencedirect.com/science/article/pii/S0144860910000312.

[4] Pulkit Dewan. “Dynamic analysis of flexible gravity-based fish cages under accidental failures in the mooring system”. In: (2019). https://uis.brage.unit.no/uis-xmlui/handle/11250/2620866, pp. 58–86.

[5] FAO. “The State of World Fisheries and Aquaculture (SOFIA)”. In: (2022). https://www.fao.org/documents/card/en?details=cc0461en. ISSN: 978-92-5-130562-1.

[6] John Howard. *The Benefits of Using Fish Farm Cage Nets for Sustainable Aquaculture Practices*. Online; accessed April 28th 2024. URL: https://www.borisnets.co.uk/the-benefits-of-using-fish-farm-cage-nets-for-sustainable-aquaculture-practices/.

[7] Pål Lader et al. “Experimental investigation of wave forces on net structures”. In: *Applied Ocean Research* 29.3 (2007), pp. 112–127. ISSN: 0141-1187. DOI: https://doi.org/10.1016/j.apor.2007.10.003. URL: https://www.sciencedirect.com/science/article/pii/S0141118707000697.

[8] H. Moe-Føre et al. “Structural response of high solidity net cage models in uniform flow”. In: *Journal of Fluids and Structures* 65 (2016), pp. 180–195. ISSN: 0889-9746. DOI: https://doi.org/10.1016/j.jfluidstructs.2016.05.013. URL: https://www.sciencedirect.com/science/article/pii/S0889974616303279.

[9] H. Schaub and J. L. Junkins. *Analytical Mechanics of Space Systems, American Institute of Aeronautics and Astronautics (AIAA)*. Reston, VA, p. 26, 27, 123. 2013.

[10] SjømatNorge. “Nurturing growth: the Norwegian way”. In: (2021). https://sjomatnorge.no/materiell/nurturing-growth-the-norwegian-way/.

[11] Geir Store norske leksikon (2005-2007); Thorsnæs. *Bjørnafjorden - fjordstykke*. Online; accessed April 24th 2024. URL: https://snl.no/Bj%C3%B8rnafjorden_-_fjordstykke.

[12] Waysail. *Mooring System*. Online; accessed April 28th 2024. URL: https://www.qdwaysail.com/Mooring-System-pd46802294.html.

[13] X Wen, H Cheng, and M C Ong. “Dynamic response of a single point mooring submersible fish cages in waves and current”. In: *IOP Conference Series: Materials Science and Engineering* 1294.1 (2023), p. 012013. DOI: 10.1088/1757-899X/1294/1/012013. URL: https://dx.doi.org/10.1088/1757-899X/1294/1/012013.

Chapter 5

Conclusion

The dynamic behaviors of fish cages are numerically studied to explore the safety issue of the aquaculture system. The hydrodynamic forces acting on the net panels are simplified into Morison forces acting on the net ropes. The structural responses of the fish cages and the mooring system are calculated using an extended position-based dynamics (XPBD) algorithm, where correction forces are added to improve the accuracy of the original XPBD. Two typical cases are involved in the present study: lifting operations of a fish cage during the de-lice or harvest operations and ultimate state analysis of multiple fish cages with a mooring system.

In the case of lifting operations, the environmental loads are neglected due to the operational condition. The structural model of modified XPBD is validated against experimental results obtained from a flexible horizontal net. A time-step sensitivity study is conducted for the lifting operation of the fish cage. The results of the lifting operations reveal a rapid increase in lifting force due to the weight of the sinkers positioned at the bottom of the side net. Furthermore, it is observed that the maximum tension in the net occurs at the net ropes connected to the center point of the bottom net. The damaged fish cages with broken net ropes at the bottom net exhibit no significant changes in lifting force and net tension. However, structural reinforcements are recommended for the bottom net to ensure safe lifting operations.

In the case of the ultimate state analysis of multiple fish cages with a mooring system, the environmental loads due to waves and currents are included to conduct the ultimate state analysis. The present modified XPBD is coupled with the Mori-

son model, and the method is validated against the experimental results of a vertical net panel and a cage net. Grid and time-step sensitivity studies are conducted for the single fish cage with a mooring system. Results show that the maximum pitch angle of the floating collar and sinker tube, the horizontal displacement, and the vertical displacement are reached when the flow angle is 0 degrees. However, the maximum horizontal force is observed when the flow angle is 30 degrees and the maximum roll angle is observed when the flow angle is 45 degrees. The effect of regular and irregular waves on a single fish cage with a mooring system shows minimal changes in the maximum calculated values. However, when subjected to regular waves, the fish cage exhibits an increased pitch angle. Summarised from the two cases, the safety of the fish cage system can be enhanced by numerically exploring the operational activities and the ultimate state.